Dissertation

to obtain the academic title

„Doctor rerum naturalium“ (Dr. rer. nat.)

submitted to the council of the

Faculty of Physics and Astronomy of the

FRIEDRICH-SCHILLER-
UNIVERSITÄT
JENA

Nano-film functionalized exposed core fibers enabling resonance-driven dispersive wave tailoring

---

research conducted at the

Leibniz ipht
LEIBNIZ INSTITUTE of PHOTONIC TECHNOLOGY

Submitted by:

Tilman Lühder

Disputation am 12.01.2023
Gutachter:

- Prof. Dr. Markus A. Schmidt, Jena
- Prof. Dr. Giancarlo Soavi, Jena
- Prof. Dr. Wonkeun Chang, Singapur

Es werde Licht! Und es ward Licht.

- Genesis 1:3

There is no such thing as objectivity.
We are all just interpreting signals from the universe and trying
to make sense of them. Dim, shaky, weak, static-y little signals that
only hint at the complexity of a universe we cannot begin to understand.

- Bones: The Doctor in the Photo

Abstract

Light sources with specific optical properties are the backbone of optical technologies. Spectroscopic applications in environmental and life sciences demand broadband sources or multiple specific, user-controlled frequency bands. Additionally, light sources with a uniform spectral power density are advantageous for imaging applications in medical diagnostics, e.g. optical coherence tomography. Ultrafast sources allow the examination of samples on extremely short time scales, whereas a high spectral stability is important for scanning, single pulse applications, and metrology. Yet, the creation of broadband, stable, and spectrally flat light sources, especially at low pump energies, remains a particular challenge. Supercontinuum generation (SCG) via the formation of solitons and the generation of dispersive waves is a well-established method for broadband light generation. This method is exceedingly effective in optical fibers as their flexible optical properties can be optimized for efficient SCG. Therefore, it is essential to accurately design and precisely control the dispersion of fibers with new methods.

This thesis aims to explore nonlinear frequency conversion in resonance-enhanced fibers to create tunable broadband light sources with tailored properties at low pump energies. By depositing high refractive index nano-films with different thicknesses on the surface of the exposed fiber core, the modal resonance of the films can be controlled to shape the dispersion of the fibers and thus the output spectrum of SCG. Different nano-film geometries are investigated starting from TiO_2 nano-films with a uniform thickness fabricated by atomic layer deposition. Next, Ta_2O_5 nano-films with a gradually increasing thickness along the fiber are examined, manufactured by a tilted sputtering method. Finally, partially masking the fiber allows for creating periodically structured Ta_2O_5 nano-films.

Experiments, supported by simulations and phase-matching considerations, reveal the advantages of longitudinal dispersion variations along the fiber over uniformly coated fibers concerning an enhanced spectral flatness and an enlarged bandwidth. The pulse dynamics are explored, leading to an expansion of the spectrum towards the infrared to span from 1.05 µm to 2.0 µm. Furthermore, periodically structured nano-films lead to multi-color tailorable higher-order dispersive waves via quasi phase-matching, which are outside of the wavelength range of classical soliton-based SCG. Novel dispersion landscapes are achieved, and the promising spectral stability is simulated.

Concludingly, resonance-based modifications of the fiber dispersion after the fiber drawing by using nano-films are a powerful new tool to efficiently shape nonlinear frequency conversion in SCG even at low pump energies. It has high technological potential for the realization of novel, ultrafast, broadband, and stable nonlinear light sources for biophotonics or hyperspectral imaging.

Zusammenfassung

Lichtquellen mit speziell abgestimmten optischen Eigenschaften bilden das Rückgrat von optischen Technologien. Spektroskopische Anwendungen in den Lebens- und Umweltwissenschaften erfordern breitbandige Lichtquellen oder Licht in mehreren spezifischen, steuerbaren Frequenzbändern. Währenddessen sind Lichtquellen mit gleichmäßiger spektraler Leistungsdichte vorteilhaft für die Bildgebung in der medizinischen Diagnose, z.B. der optischen Kohärenztomografie. Ultrakurz-gepulste Lichtquellen eignen sich für die Erforschung von Proben auf extrem kurzen Zeitskalen, wohingegen für abtastende und Einzelimpulsanwendungen sowie in der Messtechnik zusätzlich die spektrale Stabilität entscheidend ist. Dabei stellt das Erzeugen von breitbandigen, stabilen und spektral abgeflachten Spektren vor allem bei geringen Eingangsimpulsenergien eine besondere Herausforderung dar. Die Superkontinuumserzeugung (engl. supercontinuum generation, SCG) ist eine etablierte Methode zur massiven spektralen Aufweitung von Lasern für die Herstellung breitbandiger Lichtquellen mittels der Erzeugung von Solitonen und der Abstrahlung von dispersiven Wellen. Diese Methode ist besonders effektiv in optischen Fasern, weil die effiziente SCG durch die flexible Gestaltung der optischen Eigenschaften der Fasern optimiert werden kann. Deswegen ist es unerlässlich, die Dispersion von Fasern akkurat entwerfen und präzise auch mit neuen Methoden kontrollieren zu können.

Diese Arbeit zielt darauf ab nichtlineare Frequenzumwandlungen in durch Resonanzen optimierten Fasern bei geringen Eingangsimpulsenergien zu untersuchen und dadurch eine Grundlage für die Realisierung von abstimmbaren breitbandigen Lichtquellen zu schaffen. Durch eine Beschichtung der Oberfläche exponierter Faserkerne mit hochbrechenden Materialien verschiedener Dicken können die modalen Resonanzen dieser dünnen Schichten kontrolliert werden, was einen Einfluss auf die Dispersion der Fasern und die resultierenden Spektren der SCG hat. Verschiedene Schichtgeometrien werden untersucht, beginnend bei gleichmäßig dicken, durch Atomlagenabscheidung hergestellten Schichten aus TiO_2. Des Weiteren werden Ta_2O_5-Schichten mit einer entlang der Faser zunehmenden Dicke analysiert, was durch eine geneigte Sputtertechnik ermöglicht wird. Außerdem werden durch partielle Abschottung periodisch strukturierte Ta_2O_5-Schichten aufgetragen.

Experimente, die durch Simulationen und Phasenanpassungsberechnungen gestützt werden, zeigen die Vorteile längs variierbarer Dispersionen bezüglich einer verbesserten spektralen Glätte und einer erweiterten Bandbreite im Vergleich zu gleichmäßig beschichteten Fasern auf. Dabei wird die Lichtimpulsdynamik analysiert, die zu einer Frequenzverbreiterung auf den Spektralbereiche von 1.05 µm bis 2.0 µm führt. Ferner ermöglichen die periodisch strukturierten Schichten durch Quasi-Phasenanpasssung das Entstehen von mehreren anpassbaren dispersiven Wellen höherer Ordnung außerhalb der Bandbreite konventioneller Soliton-basierter SCG. Neue mögliche Dispersionsformen können erreicht werden und die erfolgversprechende spektrale Stabilität wird simuliert.

Zusammengefasst sind resonanzgestützte Veränderungen der Faserdispersion mittels dünner Schichten eine verheißungsvolle Methode um nichtlineare Frequenzumwandlung in der SCG auch nach dem Faserziehen selbst bei geringeren Eingangsimpulsenergien effizient zu manipulieren. Diese Methode hat ein hohes technologisches Potential für die Herstellung neuartiger, ultrakurz gepulster, breitbandiger und stabiler nichtlinearer Lichtquellen für Anwendungen in der Biophotonik oder hyperspektralen Bildgebung.

Contents

List of figures

List of abbreviations and symbols

AD	anomalous dispersive
ALD	atomic layer deposition
D	dimensional
DW	dispersive wave
DW_0	zero order dispersive wave
ECF	exposed core fiber
Eq.	Equation
Fig.	Figure
FoM	figure of merit
FROG	frequency resolved optical gating
FWHM	full width at half maximum
GNLSE	generalized nonlinear Schrödinger equation
GVD	group velocity dispersion
IR	infrared
MI	modulation instability
ND	normal dispersive
OSA	optical spectrum analyzer
PM	phase-matching
QPM	quasi phase-matching
Ref.	Reference
RI	refractive index
RIU	refractive index unit
RMS	root mean square
SC	supercontinuum
SCG	supercontinuum generation
SEM	scanning electron micrograph
SPM	self phase modulation
SSC	soliton self compression
UV	ultra violet
X	place holder other symbols
ZDW	zero dispersion wavelength

α	phase jump
β	propagation constant
β_1	inverse group velocity
β_2	group velocity dispersion
γ	nonlinear parameter
Γ	gamma function
ϑ	2D ray angle
θ	incident angle
$\delta(X)$	delta function
δ	asymmetry parameter
ΔX	difference of two X values
ϵ	permittivity
ϵ_0	vacuum permittivity
λ	wavelength
λ_{cut}	cut-off wavelength
λ_{p}	pump wavelength
λ_{ZD}	zero dispersion wavelength
Λ	period length/pitch
μ_0	vacuum permeability
ν	frequency
ρ	sputtering distance
σ	standard deviation
τ	time coordinate
τ_{shock}	shock coefficient
φ	substrate angle
ϕ	phase
$\mathcal{X}$	susceptibility
ψ	emitting angle
ω	angular frequency
Ω_G	soliton shifting rate

a	fiber core diameter	M	mode count
A	slowly varying pulse envelope	n	refractive index
A_{eff}	effective mode area	n_1	intensity independent RI
A_g	time gate	n_2	nonlinear index coefficient
A_i, B_i	Sellmeier parameters	n_{cl}	cladding refractive index
b	2D waveguide width	n_{co}	core refractive index
c	vacuum speed of light	n_{eff}	effective mode index
d	rod diameter	N_p	period number
$\vec{e}$	polarization direction	N_{sol}	soliton number
$\vec{E}$	electric field	$\vec{P}$	polarization
Er	erosion function	p	emitting exponent
f	focal length	P	(optical) power
ff	filling fraction	P_0	peak power
f_R	Raman fraction	q	quasi phase-matching order
g	2D waveguide length	r	radius
$g^{(1)}_{\mathrm{i,j}}$	first order coherence	R	nonlinear response function
gs	gradient strength	S_z	Poynting vector, z component
GVD_{eff}	effective group velocity dispersion	t	nano-film thickness
h	horizontal	t_s	starting nano-film thickness
h_R	Raman response function	T_0	pulse half-width at 1/e
H	angular emitting distribution	T_R	Raman time
H_0	sputtering rate prefactor	v	vertical
I	light intensity	v_g	group velocity
k	wave number	v_p	phase velocity
l_{creation}	peak creation length	V	normalized frequency/V-number
l_{nf}	nano-film length	V_{cut}	normalized cut-off frequency
L_{D}	dispersive length	X^*	complex conjugate of X
L_{f}	fission length	$X_{\mathrm{w/o}}$	X without nano-film
L_{NL}	nonlinear length	X_{w}	X with nano-film
m	2D mode order	$\vec{x}$	3D position vector
m_{cut}	cut-off wavelength slope	x,y,z	carthesian coordinates

1 Introduction

Shortly after the construction of the first laser by Maiman[4], the new bright light sources with high light intensities allowed for the experimental discovery of two photon absorption[5] and second harmonic generation[6]. Although partially being predicted earlier in 1931[7], this opened the field of nonlinear optics where the response of a system changing frequency, phase, polarization or the path of incident light starts to depend on the intensity of the incident light. Until today, nonlinear frequency conversion remains an active field of research to create novel light sources[8] or to observe quantum effects[9,10]. For instance, nonlinearly manipulated lasers allow to fill the spectral gap between the available laser wavelengths otherwise limited by the naturally existing laser media and their specific electronic structures. One prominent example is the widely used 532 nm frequency-doubled ytterbium laser. Not only can nonlinear effects such as second[11] and third harmonic generation[12,13], difference frequency generation[14] or four wave mixing[15] lead to individual, specific new wavelengths, but also continuous nonlinear spectral broadening is possible via modulation instability (MI)[16] or self-phase modulation[17]. In particular, soliton formation, the fission of higher-order solitons and the dissipation of excess energy to dispersive waves (DWs) leads to the creation of multi-octave spanning broadband light sources, creating a supercontinuum (SC)[18]. SC sources are commercialized and form the key technology for spectroscopic applications in life science[19], environmental monitoring[20,21] and biophotonics[22]. Broadband SC sources are used for food quality control[23] and optimizations in the combustion engine industry[24]. Furthermore, they can be found in superresolution microscopy[25] and hyperspectral imaging[26], medical diagnosis, for example in optical coherence tomography[27], photo-chemistry[28], and metrology[29–31]. Despite the overall success of SCG to create broadband light, for the rising variety of applications in optics and their individual requirements on their light sources, novel and unconventional methods to shape SC spectra are demanded. For example this can help to efficiently tailor spectra for spectroscopy to only contain light in useful frequency bands and reduce excess wavelengths without absorbing filters.

Nonlinear effects are most efficient at high light intensities and long phase-matched light-matter interaction lengths and can be enhanced in highly nonlinear media[32]. Focusing light to a small spot with a moderate numerical aperture creates high intensities, but the longitudinal length is severely limited by the small focal depth of a Gaussian beam. That is why high pulse energies in the mJ regime are needed for this configuration[33,34], while creating broadband spectra at lower required input power (sub nJ) is favourable for efficient small-scale and non-stationary applications.

Using femtosecond pulses allows for the high peak powers needed with minimal pulse energy, lowering the photo-toxicity for in-vivo biological samples[35] and the damage threshold

for nonlinear materials. Moreover, only ultrashort pulses enable the study of femtosecond temporal dynamics in bio-matter[36] and to understand ultrafast electronic transitions in molecules, e.g. for cancer photo-therapy via transient absorption spectroscopy[37]. Hence, femtosecond broadband light sources are demanded, which is challenging to achieve due to the fast dispersion of ultrashort pulses and the limited broadening mechanisms compatible with that time scale and low pulse energy.

Supercontinuum generation (SCG) is exceptionally efficient in optical waveguides and especially in fibers, because the tight light confinement - similar to a focus point - can be sustained for length scales from centimeters to hundreds of meters, maintaining the high light intensities needed for nonlinear effects. While this enhancement of nonlinear effects is limiting high power fiber lasers[38] and hinder optical communication[39], it can intentionally be exploited for nonlinear frequency conversion, nonlinear pulse compression[40], and optical switching[41,42]. On top of it, fibers are highly versatile as they exist in many different shapes and exhibit multiple possible guiding mechanisms, and can consist of various, potentially highly nonlinear materials of different states of matter. Thus, their optical properties can be tailored to allow for efficient nonlinear frequency conversion at specific wavelengths. For instance, supercontinua in the mid-infrared (mid-IR) are required for sensing of the spectral fingerprints of molecules[43,44] or IR reflectography of artwork[45]. More IR applications of SC spectra in spectroscopy are summarized by Zorin et al.[46]. While ongoing research also expands supercontinua towards the deep UV[47], this work focuses on SCG in the vicinity of the widely available telecommunications band around $\lambda = 1570$ nm. Still, the findings and techniques investigated in this work can also be applied to the other wavelength regimes.

The dispersion of the underlying fibers is of key importance to the resulting spectra and it is particularly crucial when using ultra-short pulses. It needs to be controlled precisely in order for the spectrum to fulfill the different demands for all of the respective applications. It has an effect on the fundamental broadening mechanisms involved in a fiber system dependent on its sign and it is involved in dictating the spectral location of and the conversion efficiency to individual features, for example the DW[18]. Hence, the spectral shape and particularly the bandwidth and the distribution of energy across the spectrum is dependent on the fiber properties. One requirement for many applications is the creation of broadband and spectrally flat light sources, i.e. having a similar spectral power density inside a specific wavelength interval. For example, this is important for optical coherence tomography with a high quality point spread function[48] or for hand-held spectroscopic devices which are unable to deliver the high dynamic range of heavy laboratory equipment[49]. One method to generate broadband and flat spectra is through modulation instability (MI) by using long pulse durations and high pulse energy[50,51]. Another solution is using high peak power to boost the soliton number and initiate soliton fission of high order solitons into multiple fundamental solitons which spread out and fill

up the spectrum[52–54]. However, both of these methods are directly associated with pulse to pulse fluctuations and loss of coherence (spectral pulse-to-pulse stability)[55,56], reducing the data consistency required for single shot and scanning applications, e.g. using the dispersive Fourier transformation[57]. Thus, it is of particular interest to generate flat and broad spectra at low pulse energies with high coherence. This, however, is also quite challenging. Other low energy approaches yielding high coherence involve self-phase modulation (SPM) in near-zero-flattened normal dispersive fibers[58–60], using highly nonlinear media such as carbon-containing solvents in liquid core fibers[61], or strongly confining nano-waveguides made out of high RI chalcogenides or semiconductors[62,63]. Yet, for easy handling and fabrication all-solid fibers with well-known materials are preferred.

One prerequisite of nonlinear frequency conversion is the phase matching (PM) of the pumping and the target feature. The undesired back-conversion process in systems generally exhibiting phase mismatch can be suppressed by periodically alternating the structural parameters such as the material composition or the geometry. This so called quasi phase matching (QPM) is classically utilized in parametric amplification; other examples of application include quantum technology[64] and UV light generation[65,66]. Furthermore, it can also be applied to other nonlinear effects such as MI[67] and four wave mixing[68,69], generating multiple additional tuneable spectral peaks. These kinds of multi-color ultrafast light sources are potentially interesting for hyperspectral imaging in medical diagnostics[35,70] or for environmental science[21]. The successes for the other nonlinear broadening mechanisms also suggest promising results for the phase matched DW creation in SCG as considered in waveguides by Hickstein et al.[71] and Phillips et al.[72]. For optical fibers, this approach led to a first experiment covering a marginal spectral interval[73]. It successfully proved the feasibility of the effect, but fails to unravel the full potential of QPM as a powerful tool to shape dispersive waves.

Although the initial drawing process of fibers allows for designing the final fiber shape and thus the fiber dispersion, its extreme sensitivity on manufacturing parameters makes it difficult to produce exact results for novel experimental nonlinear fibers. To mitigate these, post fabrication fine-tuning capabilities such as temperature or pressure control are beneficial[74,75].

Sollapur et al.[76] proved that resonances induced to fibers by the anti-crossing guiding mechanism modifies the dispersion and can lead to octave-spanning supercontinua. This suggests, that including resonances in general is a promising approach to tune nonlinear frequency conversion. One way to include resonances post fiber drawing is the addition of thin nano-films similar to ultra thin Fabry-Perot resonators[77]. Nano-film DW tuning adds post-drawing flexibility to the design of the dispersion of otherwise static fibers and consequentially to the versatility of the resulting broadened spectrum. The strong and specific nature of resonances can massively affect the fiber properties with only small modifications to the film. Nano-films are easy, fast, and cheap to implement and rival

other dispersion modulation approaches such as waveguide tapering[68,78] in accuracy and effect.

In this work, the novel concept of modifying the dispersion of optical fibers via nano-film induced resonances and its potential to shape the resulting nonlinearly broadened spectra is investigated. The nano-films are deposited directly on top of the cores of exposed core fibers (ECFs). Specifically, the tunability of the dispersive waves with respect to different nano-film geometries is analyzed, including uniform TiO_2 nano-films, Ta_2O_5 nano-films with a thickness gradient along the fiber, and periodically structured Ta_2O_5 nano-films. This novel post fiber drawing dispersion shaping method allows for tailorable broadband light generation with femtosecond pump pulses. One objective is to create light sources with a uniform spectral power density distribution by optimizing the nano-film geometry. Furthermore, the generation of multi-color tunable DWs at specific frequency bands with the help of QPM are desired. Finally, shaping the spectra at low pump energies and maintaining an excellent coherence is of interest. Overall, this work aims to set a foundation for the realization of novel broadband nonlinear light sources with tailored properties for applications in biophotonics, medical diagnostics, and metrology. Within the scope of this thesis, the following hypotheses are tested:

- Nano-films on ECFs can efficiently tune the dispersion after fiber drawing, enabling tunable DW generation.
- Implementing nano-films with a thickness gradient influences the soliton dynamics and improves the quality of the output spectra concerning bandwidth and spectral uniformity.
- Periodically modulated nano-films on ECFs allow for the creation of multi-color femtosecond QPM-DWs and feature unique effective dispersion landscapes.
- Nano-film functionalized ECFs are suitable platforms to create tuneable broadband spectra at low pump energy with a high coherence .

To address these issues, first, some general knowledge of optical fibers and especially about their the dispersion is introduced, with a short review on known dispersion modification concepts (Chapter 2). Next, the theoretical basics of soliton-driven SCG including the creation of DWs is described, serving as the base of simulations. This is followed by the introduction of the new dispersion tuning concept of this work, using modal resonances in high RI nano-films (Chapter 3). First, it is conceptually evaluated with a simple model and then adapted using the real ECF and the three actual nano-film geometries investigated experimentally in this work. Chapter 4 features the general sample fabrication process and starts with introducing the ECF. It also reveals the nano-film deposition methods as well as their evaluation. The experimental results are presented in Chapter 5, which is split in three main parts according to the nano-film geometry. After introducing experimental methods, the first part features nano-films with a constant thickness to

prove the concept of DW tuning with variation of the nano-film thickness[1]. However, the resulting spectra exhibit a particular amount of non-uniformity, i.e. they have spectral gaps, and are severely limited in bandwidth. This is overcome by introducing ECFs with a gradient nano-film, which is increasing in thickness along the fiber length and leads to a longitudinally varying dispersion[2]. Here, the aim is to create flat and coherent spectra at low pump energy, which at the same time have an increased bandwidth towards the infrared. Finally, periodically modulated nano-films are examined which, with the help of QPM, feature additional DWs outside the spectral range of classical SCG, extending the spectra even further towards the IR[3]. As an outlook, possible combinations of the effects using more complicated nano-film geometries are briefly portrayed. All findings of this work are summarized in Chapter 6.

2 Fundamentals of nonlinear fiber optics

2.1 Introduction to optical fibers

Optical fibers can guide light over large distances and are therefore widely used for modern high-speed communication all around the globe. Another high-impact sector is the usage in specific light sources such as fiber lasers and supercontinuum (SC) sources. Because of their integration potential, robustness, and flexibility, there is a trend to transform all bulk optical devices into their pure fiber based counterparts, including photodetectors[79], pulse stretchers[80], optical amplifiers[81], beam splitters[82], and polarization controllers[83]. All applications require specific parameters and properties of their individual fiber, ranging from their guidance concept over losses to their dispersion and nonlinear characteristics.

The simplest light guiding mechanism of fibers is total internal reflection at the boundary of two materials with different RI. Thus, light rays inside a fiber core cannot escape into the surrounding cladding for shallow ray angles if the involved refractive indices n for the core and the cladding fulfill $n_{\mathrm{co}} > n_{\mathrm{cl}}$. Only certain rays constructively interfering with each other in transversal direction after two reflections can propagate as an ensemble and lead to distinct optical fiber modes propagating through the fiber (Fig. A.1 and supporting text in the appendix). Details about the ray model in optical waveguides, mode formation, and the transition to electromagnetic waves in 3D structures are comprehensively deduced in optics textbooks, for example by Saleh & Teich in Chapter 7 (Ref. 84). The amount of different modes possible in a cylindrical step index fiber of core diameter a can be estimated using the normalized frequency (V-number)

$$V = \frac{2\pi a}{\lambda}\sqrt{n_{\mathrm{co}}^2 - n_{\mathrm{cl}}^2}. \tag{2.1}$$

For $V > 2.4048$ a step index fiber becomes multi-mode with the amount of modes $M \approx V^2/2$ for $V \gg 1$.

The modes of fibers can be calculated by solving Maxwell's equations in the form of the wave equation for an electric field $\vec{E}$ and the polarization $\vec{P}$ with the condition of no free charges in non-magnetic media

$$\nabla \times \nabla \times \vec{E}(\vec{x},t) = \mu_0 \frac{\partial^2}{\partial t^2}\left[\epsilon_0 \vec{E}(\vec{x},t) + \vec{P}(\vec{x},t)\right]. \tag{2.2}$$

ϵ_0 is the vacuum permittivity and μ_0 represents the vacuum permeability. It is useful to handle the wave equation in the frequency domain (angular frequency: ω) with the linear dependence $\vec{P}(\vec{x},\omega) = \epsilon(\omega)\vec{E}(\vec{x},\omega)$. Assuming low losses ($\epsilon(\omega) \approx Re(n)^2(\omega)$) and homogeneous, isotropic media, Eq. 2.2 can be rewritten as a Helmholz equation

$$\nabla^2 \vec{E}(\vec{x},\omega) + \frac{n^2(\omega)\omega^2}{c^2}\,\vec{E}(\vec{x},\omega) = 0. \tag{2.3}$$

Solving Eq. 2.3 within the core and cladding section of the fiber and applying appropriate boundary conditions, the modes of fibers can be calculated. A detailed walk-through to calculate the modes of various types of fibers, in particular for circular step-index fibers, can be found in the literature, e.g., by Snyder and Love[85]. The calculation peaks in an Eigenvalue problem where the wanted Eigenvalue is the propagation constant β of the mode and the Eigensolution determines the electric and magnetic field distributions. $n_{\text{eff}} = \beta\lambda/(2\pi)$ is the effective (refractive) index and represents the RI of a homogeneous medium where a freely expanding optical wave would have the same propagation constant as the mode in the fiber. For total internal reflection based fibers it always lies in between the RI of the core and the cladding $n_{\text{co}} > n_{\text{eff}} > n_{\text{cl}}$ and the fundamental mode has the largest value. The effective index and its dependence on the wavelength is a key parameter for nonlinear fiber optics, in particular their second derivative as being discussed in Section 2.2.

For fibers with a more complicated cross section, analytical solutions are difficult to obtain and the modes are typically calculated numerically. Here, the calculations are accomplished with a commercial solver using the Finite-Element Method (COMSOL Multiphysics), importing the exact fiber geometry of a Scanning Electron Microscope (SEM) image and taking the silica dispersion of Malitson[86]. This method is universally applicable and can also find solutions in case the guiding mechanism would change from RI based to anti-resonance[87], inhibited coupling[88], or band gap effects[89].

2.2 Dispersion in optical fibers

When considering nonlinear applications, the dispersion of fibers is essential for the pulse propagation. It determines the linear spatial, spectral, and temporal evolution of pulses along the fiber while being a relevant parameter for nonlinear effects. This section provides the description of the dispersion and related relevant parameters, followed by an analysis of the physical origin of dispersion caused by material properties and waveguide confinement. Then, several existing dispersion tuning schemes are presented.

One common parameter to assess the dispersion is the wavelength dependent effective mode index n_{eff}. It specifies at which speed the phase is propagating in comparison to the vacuum speed of light c: $v_p = c/n_{\text{eff}} = \omega/k$, with $k = 2\pi n_{\text{eff}}/\lambda$ symbolizing the wave number inside a medium. For optical pulses, the group velocity $v_{\text{g}} = d\omega/dk$ determines the speed of the pulse envelope. It is connected by the first derivative of the propagation constant β (often equivalent to k in longitudinal direction) with respect to ω.

$$\beta_1 = \frac{d\beta}{d\omega} = \frac{n_{\text{eff}}}{c} - \frac{\lambda}{c}\frac{dn_{\text{eff}}}{d\lambda} = \frac{1}{v_{\text{g}}} \tag{2.4}$$

In order to describe the change of the group velocity when considering wave packets at different wavelengths, the group velocity dispersion (GVD) is essential, i.e. the second derivative of β with respect to ω.

$$\mathrm{GVD} = \beta_2 = \frac{\mathrm{d}^2\beta}{\mathrm{d}\omega^2} = \frac{\lambda^3}{2\pi \mathrm{c}^2}\frac{\mathrm{d}^2 \mathrm{n}_{\mathrm{eff}}}{\mathrm{d}\lambda^2} \tag{2.5}$$

A positive GVD represents the case where wave packets having shorter wavelengths propagate slower compared to ones with longer wavelengths. This condition is called the normal dispersive (ND), whereas for negative GVD, where shorter wavelengths travel faster than pulses of longer wavelengths, this is named anomalous dispersive (AD). Between the two dispersion domains there is a zero-crossing of the GVD at the so-called zero dispersion wavelength (ZDW,λ_{ZD}).

Especially for ultra-short pulses the transform-limited bandwidth is broad, making the pulse more susceptible to temporal broadening due to a non-zero GVD. This temporal broadening is minimized near the ZDW, leaving it susceptible to higher-order dispersion effects. A numerical value to determine the temporal broadening is the dispersion length L_{D}, as defined by Agrawal[18]

$$L_{\mathrm{D}} = \frac{T_0^2}{|\mathrm{GVD}|}, \tag{2.6}$$

with T_0 being the input pulse width (half-width at 1/e of the maximum intensity).

Operating near the ZDW can increase the conversion efficiency of nonlinear effects for example four wave mixing in communications[90] or dispersive wave generation[91,92]. Most lasers have a fixed wavelength and require a special fiber with a ZDW near the pump wavelength (λ_{p}) for efficient nonlinear frequency conversion. Therefore, studying the dispersion of fibers, especially the origin and possibilities to modulate the dispersion landscape in order to shift the ZDW near λ_{p} is desirable.

2.2.1 Origin of dispersion

There are two main effects contributing to the total dispersion of a fiber: Material dispersion and waveguide dispersion. Those two effects can be explained with a simple 2D waveguide ray model. A high RI layer is embedded within a low RI background medium and light is guided in the central layer by total internal reflection (Fig. A.1). The optical path length of the light ray is determined by two parameters: First, the wavelength dependent RI of the core material (material dispersion) and, second, the actual geometric path length of the ray (waveguide dispersion). The latter is defined by the constructively interfering phase criterion after one round-trip, consisting of the transverse propagation inside the waveguide and the two phase jumps of the reflections. The derivation of the GVD of the 2D ray model including the identification of the influence of material and waveguide dispersion can be found in the Appendix (Fig. A.1 and related text). In the

literature the waveguide dispersion is often seen as the difference of the total fiber dispersion minus the material dispersion and is not calculated individually. The separation of the total dispersion is a simplification as the interaction of material and waveguide has some cross terms and cannot be split into a simple addition of individual contributions in general[93]. Moving from the ray picture to a more realistic scenario with evanescent fields, the material dispersion depends on the core and the cladding composition and their relative contributions vary with the wavelength as the mode field diameter changes. On top of it, a profile dispersion term needs to be added in case of gradient index fibers[94]. However, the simplification of separating the total dispersion in individual contributions can be successfully applied for special cases of specific fibers[95] and can yield insights to dispersion management.

Although an analytical splitting of the dispersion is possible for the 2D waveguide ray model, also a numerical splitting is possible, being applicable even to complex fibers with arbitrary cross sections where analytical solutions cease to exist. With a known n_{eff} by simulations (Section 2.1), the GVD can be retrieved by numerically differentiating the n_{eff} at the central wavelength $\lambda = \lambda_0$ according to Eq. 2.5, using three supporting points separated by the spectral distance $\Delta\lambda$

$$\mathrm{GVD}_{\mathrm{total}}(\lambda_0) = \frac{\lambda_0^3}{2\pi \mathrm{c}^2} \frac{\mathrm{n}_{\mathrm{eff}}|_{\lambda_0-\Delta\lambda} - 2\mathrm{n}_{\mathrm{eff}}|_{\lambda_0} + \mathrm{n}_{\mathrm{eff}}|_{\lambda_0+\Delta\lambda}}{(\Delta\lambda)^2}. \tag{2.7}$$

When separating the GVD into a material and waveguide part, the supporting points for the central second order differential quotient can be chosen accordingly. Either, they only respect the wavelength dependence of n_{eff} while using core and cladding materials $n_{\mathrm{co,cl}}$ without dispersion, or they only account for material dispersion while keeping the same wavelength for the simulation of n_{eff}. Adding both contributions leads to the novel formulation of $\mathrm{GVD}_{\mathrm{sum}}$ with the notation $n_{\mathrm{eff}}(\mathrm{wavelength}, \mathrm{material})$ of the supporting points

$$\begin{aligned}
&\mathrm{GVD}_{\mathrm{sum}}(\lambda_0) \approx \\
&\frac{\lambda_0^3}{2\pi c^2}\Bigg(\underbrace{\frac{n_{\mathrm{eff}}(\lambda_0-\Delta\lambda, n_{\mathrm{co,cl}}(\lambda_0)) - 2n_{\mathrm{eff}}(\lambda_0, n_{\mathrm{co,cl}}(\lambda_0)) + n_{\mathrm{eff}}(\lambda_0+\Delta\lambda, n_{\mathrm{co,cl}}(\lambda_0))}{(\Delta\lambda)^2}}_{\text{waveguide dispersion}} + \\
&\underbrace{\frac{n_{\mathrm{eff}}(\lambda_0, n_{\mathrm{co,cl}}(\lambda_0-\Delta\lambda)) - 2n_{\mathrm{eff}}(\lambda_0, n_{\mathrm{co,cl}}(\lambda_0)) + n_{\mathrm{eff}}(\lambda_0, n_{\mathrm{co,cl}}(\lambda_0+\Delta\lambda))}{(\Delta\lambda)^2}}_{\text{material dispersion}}\Bigg).
\end{aligned} \tag{2.8}$$

For the sake of simplicity, this numerical model is applied to perfectly circular silica rod embedded in air. This step-index-fiber-like model with an adapted core diameter should result in qualitatively similar dispersion landscapes compared to the core of uncoated ECFs, consisting of the same materials and having the same guiding mechanism. The solution of n_{eff} for the step index fiber can be calculated analytically as described by Snyder

and Love[85], serving as the basis to numerically calculate the GVD using Eqs. 2.7, 2.8, and the individual parts of Eq. 2.8 (Fig. 2.1). The results are independent of the step size which is set as $\Delta\lambda = 10$ nm. For silica rods with a large diameter of $d = 10$ µm compared to the wavelength of $\lambda = 1570$ nm, the fiber is weakly guiding and the dispersion resembles the one of bulk materials. Therefore, the contribution of the material dispersion is dominant, especially for short wavelengths (Fig. 2.1a). The total dispersion and the sum of the individual effects are identical, validating the splitting equation (Eq. 2.8). For smaller silica rods ($d = 3$ µm) the mode gets confined more, making the fiber to be stronger guiding and increasing the contribution of the waveguide dispersion (Fig. 2.1b). At even smaller diameters, becoming comparable to the wavelength ($d \leq 1.5$ µm), the waveguide dispersion bends upwards, creating a second ZDW (Fig. 2.1c). Here, a small difference of the sum representation of the GVD (Eq. 2.8) compared to the exact solution (Eq. 2.7) is observable at long wavelengths. Hence, the splitting of the dispersion becomes inaccurate for strongly guiding fibers. For $d = 1$ µm the material dispersion is negligible compared to the dominating waveguide dispersion. Although being almost identical for all fiber dimensions, the material dispersion still slightly changes according to the different evanescent fields, making this approach superior to pure bulk material dispersion models. Despite the approximation to represent the dispersion as a sum having errors as

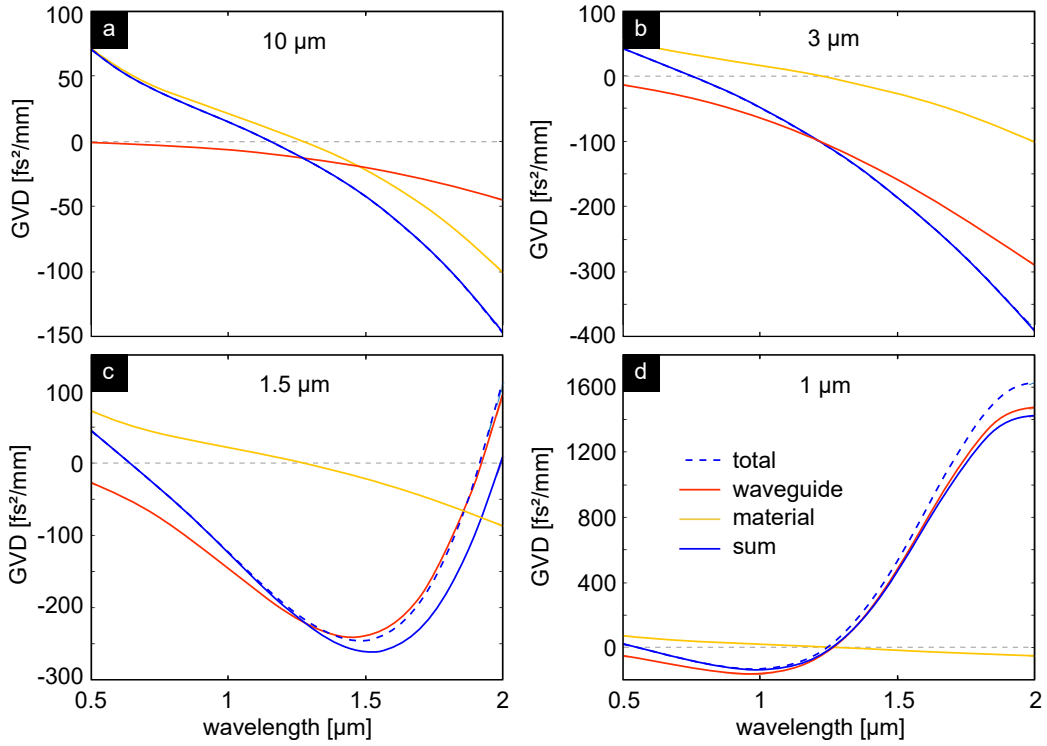

Figure 2.1: Calculated group velocity dispersion of a silica cylinder in air with diameters of $d = 10$ µm to $d = 1$ µm based on the analytical solution of n_{eff} with $\Delta\lambda = 10$ nm. The calculation using the second order differential quotient (total, Eq. 2.7) is opposed to the approximated dispersion (sum), consisting of the sum of the individual contributions of material and waveguide dispersion according to Eq. 2.8.

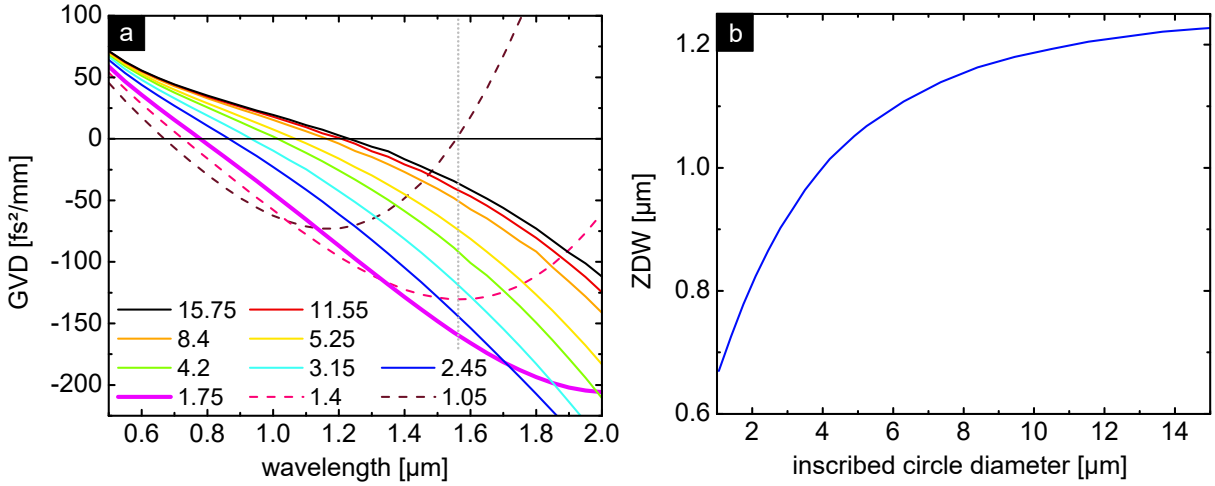

Figure 2.2: (a) GVD distribution for the bare ECF with different inscribed circle diameters indicated in the legend (in µm). The fat magenta line represents the fiber used for experiments in this work. Dashed and solid lines refer to smaller and larger core sizes, respectively. The pump wavelength is marked with a gray vertical dotted line. (b) Short-wavelength ZDWs of the curves in (a).

there should be some higher-order cross terms of the waveguide and material dispersion contributions, the qualitative behavior is identical to the exact solution in the examples investigated here.

Consequently, the total dispersion can be modified by increasing the impact of the waveguide dispersion or by exchanging the material composition of the waveguide. The material dispersion is primarily responsible for the position of the single ZDW for weakly guiding fibers, whereas the waveguide dispersion can cause a highly sensitive second ZDW at long wavelengths. With carefully designing the geometry and material composition, also fibers with three[96], waveguides with four[97] or coupled waveguide arrays with eight ZDWs[98] are possible.

2.2.2 Geometric dispersion tuning

The most straight-forward way for waveguide dispersion tuning is changing the core size of fibers. In the following example the shape of the cross section of a bare ECF (Fig. 4.1) is scaled in simulations to have various inscribed circle diameters. Starting at the actual fiber size used for experiments in this work (fat magenta line in Fig. 2.2a), the first ZDW is located near $\lambda = 800$ nm. Increasing the size in simulations red-shifts the dispersion by reducing the impact of the waveguide dispersion until it becomes negligible and the GVD curve approaches the dispersion of bulk silica. The ZDW increases in wavelength and gradually approaches the bulk ZDW of silica of $\lambda_{ZD} = 1.27$ µm[99] (Fig. 2.2b). Although being tunable to a certain amount, the first short-wavelength ZDW is limited at the long-wavelength edge by the bulk properties. In particular, this makes the first ZDW impossible to use for efficient nonlinear frequency conversion in the telecommunications

regime around $\lambda_p = 1570$ nm in this work. The ZDW is not close enough to the pump wavelength and, on top of it, the longest possible ZDWs are also connected to a large core size, reducing the peak intensity available for nonlinear light-matter interactions.

Reducing the size (dashed lines in Fig. 2.2a) causes the blue shift of the second ZDW, originally located around $\lambda_{ZD} = 2.7$ µm for the actual fiber size, which is outside the wavelength of interest. It reaches the pump wavelength at an inscribed circle diameter of 1.05 µm. Being smaller than the wavelength, the small core size reduces the efficiency of free space coupling of light into the fiber, hence, reduces the peak power and complicates nonlinear frequency conversion. Moreover, the second ZDW is more sensitive to core diameter tuning compared to the first ZDW, making fiber drawing with the exact parameters difficult[100]. Therefore, other dispersion tuning mechanisms need to be explored to make this fiber attractive for nonlinear frequency conversion in the telecommunications regime.

2.2.3 Further dispersion tuning mechanisms

The dispersion of fibers can be modified by altering the material dispersion, i.e. using different materials as optical core. For example, high index chalcogenides[101,102] and semiconductor cores composed of silicon or germanium[103–105] can replace the usual core material of pure or Ge-doped silica. Apart from solid material alternatives, hollow cores filled with liquids[106–108] or low RI gases[109] are of rising interest because of the enhanced molecular nonlinearity[110,111]. Furthermore, material composites such as mixing liquids[112] and meta-materials[113] are possible. For example, the latter is used in the cladding of photonic crystal fibers, consisting of a hollow channel array in a host material, that can be filled with various other materials[114,115]. One interesting material are liquid crystals[116] which are highly birefringent and can be tuned electrically.

Non-solid materials have the advantage that the dispersion can be tuned externally with gas and hydrodynamic pressure[75,117–119], as well as temperature owing to the bigger thermo-optical coefficient of liquids[74,120,121]. However, the material dispersion does not change much as in a first order approximation only a constant n_{eff} offset is applied and even a linear dependence on the wavelength is canceled out by taking the second derivative to calculate the GVD. Thus, temperature tuning affects the waveguide dispersion by changing the core-to-cladding RI contrast, having a similar effect to geometric size tuning[74]. Particularly, the second, long-wavelength ZDW can be shifted mainly while having a minor effect on the short-wavelength ZDW. Furthermore, the dispersion can be also externally modified by controlling the plasma density in gas-filled photonic crystal fibers[76,122].

Without changing the materials, the waveguide dispersion can be altered by different fiber designs and light guiding mechanisms, specifically anti-resonant[123] and photonic band-gap fibers[124]. Moreover, using higher-order modes gives access to modified dispersion landscapes[125,126].

The introduction of resonances into waveguides via the anti-resonant guiding mechanism strongly affects the dispersion, enabling multi-octave spanning supercontinuum generation[76]. This suggests that the novel dispersion modification approach analyzed in this work in Chapter 3, employing modal resonances originating from nano-films[1,2], can be particularly useful for nonlinear frequency conversion. Having an all-solid fiber approach is favorable for many applications, easing fiber handling and avoiding the lower damage threshold of nonlinear liquids such as CCl_4[127].

With the knowledge of the dispersion in fibers and the possibility to modify and influence it, the next section introduces the basics of nonlinear effects in fibers that can be achieved with specifically designed fiber and dispersion parameters.

2.3 Basics of supercontinuum generation

The creation of a broad continuous spectrum from one or a few narrow-band light sources is called supercontinuum generation. SC sources provide light with high radiance compared to non-directed light (e.g. laser diodes) and can outclass synchrotron radiation regarding the generated power in selected bands[128]. The term SCG is not bound to a specific phenomenon but rather covers a plethora of different effects and combinations of them, leading to diverse spectral broadening and frequency conversion. Most of the effects are of nonlinear nature and only occur at high light intensities. If not indicated otherwise, the following theoretical introduction to nonlinear effects and SCG in fibers is based on the book 'Nonlinear Fiber Optics' by Agrawal[18].

2.3.1 Nonlinear refraction

The origin of nonlinearities in optical media is the response of charge carriers to external electromagnetic fields. At high excitation levels, the bound electrons will respond anharmonically to a perfectly harmonic field. Therefore, the polarization $\vec{P}$ in a medium can be expressed as a Taylor series of the applied field $\vec{E}$

$$\vec{P} = \epsilon_0 \sum_{i=1}^{\inf} \overset{\leftrightarrow}{\mathcal{X}}^{(i)} \vec{E}^i, \tag{2.9}$$

where ϵ_0 is the vacuum permittivity and the various orders of $\overset{\leftrightarrow}{\mathcal{X}}$ are the susceptibilities. The dominant term at low intensities is the linear one ($\overset{\leftrightarrow}{\mathcal{X}}^{(1)}$), determining the base RI of the material. The second order susceptibility is causing nonlinear effects, e.g. second-harmonic generation and sum-frequency generation. However, $\overset{\leftrightarrow}{\mathcal{X}}^{(2)}$ is negligible for center-symmetric media such as silica and thus has no observable influence on the observed spectra in this work. Third order susceptibility effects include third harmonic generation, four wave mixing, and the Kerr effect. The latter implies that the RI of a material at one

specific wavelength is not constant, but in first order depends on the intensity I of the incident light

$$n(I) = n_1 + n_2 I(t). \tag{2.10}$$

Here, n_1 is the constant part of the RI and n_2 is the nonlinear index coefficient related to $\mathcal{X}^{(3)}$. With a Gaussian intensity distribution in time of a short pulse, the RI of the medium at a constant position rises from and falls back to n_1 when the pulse is traversing through it.

2.3.2 Nonlinear parameter

The material dependent nonlinear index coefficient determines the suitability for nonlinear frequency conversion. Silica with $n_{2,\,\mathrm{silica,1550nm}} = 2.8 \cdot 10^{-20}\,\mathrm{m^2/W}$ (Ref. 129) has a rather low nonlinear coefficient which motivates the study of fibers with exotic, highly nonlinear materials such as soft glasses[101,130], or fibers with liquid-filled cores[108]. For example, the nonlinearities of TiO_2 and Ta_2O_5, e.g. used for nonlinear waveguides, are more than one magnitude higher at $n_{2,\,\mathrm{TiO_2}} = 9 \cdot 10^{-19}\ \mathrm{m^2/W}$[131] (average of both crystal axis values of bulk rutile TiO_2 at 800 nm) and $n_{2,\,\mathrm{Ta_2O_5}} = 6.2 \cdot 10^{-19}\ \mathrm{m^2/W}$[132], respectively. Apart from changing the material, nonlinear effects can be enhanced by increasing the light intensity through high confinement in optical fibers. Therefore, it is useful to define the nonlinear parameter γ, combining material and fiber nonlinear potential into one value[133]

$$\gamma(\lambda) = \frac{2\pi}{\lambda} \frac{\int n_2 S_z^2 dA}{\left(\int S_z dA\right)^2}, \tag{2.11}$$

where S_z is the longitudinal component of the Poynting vector of the mode. This definition is different from the one by Agrawal[18], and is only valid for modes with a high transversality (defined by Steel[134]), i.e. with fields that are oriented mostly in transversal direction. Since the modes discussed here have a high transversality, considering a full vectorial model to calculate γ as proposed by Afshar and Monro[135] is not needed.

2.3.3 Self-phase modulation

At high power, short pulses propagating through a medium modulate the RI through the Kerr effect (Section 2.3.1). During the propagation along z, the phase of the pulse shifts in time t and space

$$\phi = \omega_0 t - kz = \omega_0 t - \frac{2\pi}{\lambda} n(I) z. \tag{2.12}$$

The change of the phase in time is the frequency, but including the time dependent RI $n(I(t))$ results in an additional term causing a perturbation $\delta\omega$[17]

$$\omega = \frac{d\phi}{dt} = \omega_0 - \frac{2\pi z}{\lambda} \frac{dn(I)}{dt} = \omega_0 - \frac{2\pi z\, n_2}{\lambda} \frac{dI}{dt} = \omega_0 - \delta\omega. \tag{2.13}$$

$\delta\omega$ causes the leading half of a pulse with increasing intensity in time to shift towards longer wavelengths (red shift) and the trailing half to blue shift. Consequently, a pulse will first split up into two pulses having a longer and a shorter central wavelength compared to the initial one. Afterwards, due to cascaded pulse splitting, a series of peaks with various frequencies can emerge, overall broadening the spectrum[17]. This nonlinear broadening is called self-phase modulation (SPM) and it is symmetric in frequency for symmetric initial pulses.

With the group velocity being defined as $v_g = \frac{dw}{dk}$, Eq. 2.13 also makes v_g dependent on the local intensity of a pulse in the time domain. Specifically, the center of a pulse with a high intensity will travel slower compared to its wings, deforming the pulse in time and steepening the trailing slope. This so-called self steepening leads to an asymmetry in SPM and can create optical shock[136].

When the pulse spectrally broadens sufficiently it gets affected by dispersion, influencing the temporal pulse shape and leading to more complex phenomena, for instance, optical solitons.

2.3.4 Solitons

In normal dispersive media light pulses with longer wavelength travel faster than pulses at shorter wavelength. Therefore, the red shifted leading edge of a pulse broadened by SPM will separate itself further in time from the trailing blue shifted part, leading to fast pulse dispersion and eventually optical wave breaking[137]. Contrarily, in anomalous dispersive media the two sides of the pulse will be compressed in time, ultimately changing their temporal order and being converted back towards the central initial wavelength by SPM. Therefore, the combination of SPM and anomalous dispersion can result in a stable wave packet that stays well-confined in the spectral as well as temporal domain without dispersing. These properties define a solitary wave (or short: soliton), first described in 1834 by John Scott Russell for a water wave[138]. An equilibrium of the two effects leading to soliton formation is only possible at a certain light intensity combined with a matching dispersion at a specific wavelength. Thus, the pulse power influences the wavelength at which a soliton is created. Non-matching combinations, e.g. at higher pulse powers, can be stable in a dynamic way instead of having a static solution. This results in a periodical oscillation between different pulse durations and associated bandwidths with certain, not necessarily single peak, spectral and temporal shapes. This behaviour is called soliton breathing and is analyzed in detail in Ref. 139. Its occurrence starts at high input pulse powers and can be quantified with the order of the soliton, i.e. the soliton number N_{sol}[18]

$$N_{\mathrm{sol}} = \sqrt{\frac{L_{\mathrm{D}}}{L_{\mathrm{NL}}}} = \sqrt{\frac{\gamma P_0 T_0^2}{|\beta_2|}}. \tag{2.14}$$

Here, L_{D} is the dispersive length (Eq. 2.6) and L_{NL} stands for the nonlinear length defined as

$$L_{\mathrm{NL}} = \frac{1}{\gamma P_0}, \tag{2.15}$$

using the peak power of the soliton P_0. L_{D} and L_{NL} represent the length scales after which dispersive and nonlinear effects become relevant for the pulse evolution, respectively. $N_{\mathrm{sol}} = 1$ corresponds to a fundamental soliton with a static solution and higher values lead to higher-order solitons. Higher-order dispersion terms, self steepening, optical losses, and the Raman scattering can diminish the stability of soliton breathing and induce the breakdown of higher-order solitons into multiple different fundamental solitons with various widths and powers[18,140,141], called soliton fission. Soliton fission primarily happens at the first temporal compression and connected spectral broadening of the higher-order soliton. Specifically, the position along the fiber can be estimated by the fission length

$$L_{\mathrm{f}} = \sqrt{L_{\mathrm{NL}} L_{\mathrm{D}}}. \tag{2.16}$$

The amount of fundamental solitons created is the integer number closest to N_{sol}. With the spread of several different fundamental solitons across the spectrum and associated cascaded nonlinear effects for each of them, soliton fission is a commonly exploited effect for spectral broadening in SCG[142,143].

Raman scattering is based on the absorption of photons to a virtual state and their release at a smaller energy (Stokes wave) by deexciting to a vibrational state with a characteristic energy band dependent on the chemical composition of the material. This effectively scatters photons while elongating the wavelength and creates heat. Solitons can be narrow in time and thus exhibit a broad bandwidth. Therefore, Raman-scattered photons from the short-wavelength side spectrally overlap with the red tail of the soliton, leading to intra-pulse stimulated Raman scattering. In contrast to (amplified) spontaneous Raman scattering in short pulses and Raman assisted four wave mixing, it does not require phase matching to be efficient[144,145]. As a result, the soliton is steadily shifting towards longer wavelengths while losing some energy. Neglecting higher-order terms, the rate of the red-shifting soliton Ω_G (in rad/s) is determined by Gordon's formula[146] and is proportional the propagation length z

$$\Omega_G = -\frac{8|\beta_2| T_R}{15 T_0^4} z, \tag{2.17}$$

where $T_R = 3$ fs is the Raman time in silica fibers[147]. The quadruple dependence on the temporal width of the soliton makes the soliton intra-pulse stimulated Raman scattering induced red shift highly dependent on the fiber and pulse parameters. For a strong continuous Raman shift the broadening of the shifting soliton during propagation while red shifting needs to be prevented, e.g. by tapering fibers[148]. The approximated equation by Gordon can be improved by including the effects of propagation losses, self-steepening,

and dispersion slope, inducing a more accurate nonlinear dependence on the propagation distance[149].

2.3.5 Dispersive waves

Solitons perturbed by higher-order dispersion emit part of their energy to other frequencies in the normal dispersive domain of the spectrum. These new spectral features are called Cherenkov radiation[92] or nonsolitonic radiation and because of their dispersive nature in contrast to solitons are also named dispersive waves (DWs). As the creation of DWs is a phase-matched process, the wavelength of the emitted radiation from solitons can be accurately calculated. The phases of pulses at the frequency of the DW ω_{DW} and the soliton ω_{sol} after a propagation time $t = z/v_g$ can be expressed as

$$\phi(\omega_{\mathrm{DW}}) = \omega_{\mathrm{DW}} t - k(\omega_{\mathrm{DW}}) z \qquad = \omega_{\mathrm{DW}} \frac{z}{v_g} - \frac{\omega_{\mathrm{DW}} n(\omega_{\mathrm{DW}})}{c} z \tag{2.18}$$

$$\phi(\omega_{\mathrm{sol}}) = \omega_{\mathrm{sol}} t - k(\omega_{\mathrm{sol}}) z - 0.5\gamma P_0 z = \omega_{\mathrm{sol}} \frac{z}{v_g} - \frac{\omega_{\mathrm{sol}} n(\omega_{\mathrm{sol}})}{c} z - 0.5\gamma P_0 z. \tag{2.19}$$

The difference of the phases of Eqs. 2.18 and 2.19 ($\Delta\phi$), which includes the nonlinear phase of the soliton, gives the phase matching (PM) condition for $\Delta\phi = 0$. Rewritten in terms of the wavelength and effective RIs (corrected from Ref. 71), the phase mismatch to potential DW wavelengths λ is

$$\Delta\phi(\lambda) = n_{\mathrm{eff}}(\lambda_{\mathrm{sol}}) + (\lambda - \lambda_{\mathrm{sol}}) \left.\frac{dn_{\mathrm{eff}}}{d\lambda}\right|_{\lambda_{\mathrm{sol}}} + \frac{\gamma P_0 \lambda}{4\pi} - n_{\mathrm{eff}}(\lambda). \tag{2.20}$$

With a soliton number close to 1 the soliton peak power P_0 at the soliton wavelength λ_{rmsol} can be estimated by replacing it with the pump pulse peak power. Albeit usually given in units of rad/cm, in the version of the equation used in this work the phase mismatch can be expressed in units of the RI, effectively representing an effective refractive index mismatch.

Akhmediev and Karlsson[92] proposed an alternative method to calculate λ_{DW} based on the second and third order dispersion terms. However, this approximation cannot be applied to nano-film functionalized ECFs as their complex dispersion landscape includes higher-order terms and cannot be described accurately enough with a Taylor series up to third order only. Additionally, they provide an estimation for the power of DWs, accounting for dispersion terms up to the third order

$$P_{\mathrm{DW}} \approx \left(\frac{5\pi N_{\mathrm{sol}}}{4\delta_3}\right)^2 \left(1 - \frac{2\pi}{5}(2N_{\mathrm{sol}} - 1)\delta_3\right)^2 \exp\left(-\frac{\pi}{2(2\mathrm{N_{sol}} - 1)\delta_3}\right) \mathrm{P}_0 \tag{2.21}$$

$$\text{with} \quad \delta_3 = \frac{\beta_3}{6|\beta_2|T_0}. \tag{2.22}$$

Equation 2.21 implies that fibers with a smaller β_2 to β_3 (third derivative of β with respect to ω) ratio have a stronger conversion efficiency to the DW[91]. Because P_{DW} depends on the soliton power, DW creation from the strongest, most red shifted soliton is the dominant frequency conversion process. Other fundamental solitons after fission can also generate DWs in principle, but they are neglected in many cases.

Newly generated frequencies such as DWs can be generated from noise in principle[139], yet, the conversion is enhanced in case they are seeded[150,151]. The seed of the DW needs to be present at the same temporal and spatial position in relation to its source, i.e. the soliton. Because of the dispersion in fibers and the walk-off of different wavelengths, especially for ultra-short pulses, this implies that only the soliton itself can act as a seed. Thus, there needs to be a spectral overlap of λ_{DW} with the soliton. For DWs spectrally far away from λ_s the overlap can be fulfilled when the soliton exhibits spectral broadening, e.g. via temporal compression. This happens during the soliton formation at the potential soliton fission point, and in case of no fission also periodically during soliton breathing of higher-order solitons. These form the two prime opportunities for efficient nonlinear frequency conversion to DWs, which occur only at certain positions along the fiber length[141].

2.3.6 Quasi phase-matching for dispersive waves

Regularly disturbing the dispersion along the propagation direction of optical pulses, e.g. by periodically changing the geometry of fibers, induces an additional geometric lattice vector $k_{\mathrm{QPM}} = 2\pi q/\Lambda$ to the system (e.g. as used in the supplementary information of Ref. 73). Λ is the period length of the perturbation and q is an integer value referring to different orders. This not only alternates the properties locally within the individual sections, but also has a global effect. Specifically, it adds a term to the PM condition and expands Eq. 2.20, forming Eq. 2.23 (corrected from Ref. 71) and now being called a QPM condition

$$\Delta\phi(\lambda) = n_{\mathrm{eff}}(\lambda_{\mathrm{sol}}) + (\lambda - \lambda_{\mathrm{sol}}) \left.\frac{dn_{\mathrm{eff}}}{d\lambda}\right|_{\lambda_{\mathrm{sol}}} + \frac{\gamma P_0 \lambda}{4\pi} - n_{\mathrm{eff}}(\lambda) - \frac{q\lambda}{\Lambda} = 0. \tag{2.23}$$

As q can adopt both positive and negative values, this leads to PM wavelengths at shorter and longer wavelengths compared to the DW without QPM. The latter is identical to the zeroth order QPM-DW with $q = 0$, therefore also named DW_0 in this work.

All in all, the nonlinear effects described so far can be summarized as sketched in Fig. 2.3. The initial pump pulse undergoes spectral broadening and temporal compression owing to SPM. In the AD domain of the fiber, a soliton of order N_{sol} can be formed, which might fission to multiple solitons around L_{f} (1.). Energy can be dissipated to phase matched DWs with the potential to also form higher-order DWs in case periodic structures are used to enable QPM (2.). Finally, intra-pulse stimulated Raman

scattering shifts the solitons towards longer wavelengths (3.).

Apart from these main effects which are principally featured in the experiments of this work, in general, also other nonlinear phenomena can occur and contribute to nonlinear spectral broadening in fibers as described in the next sections.

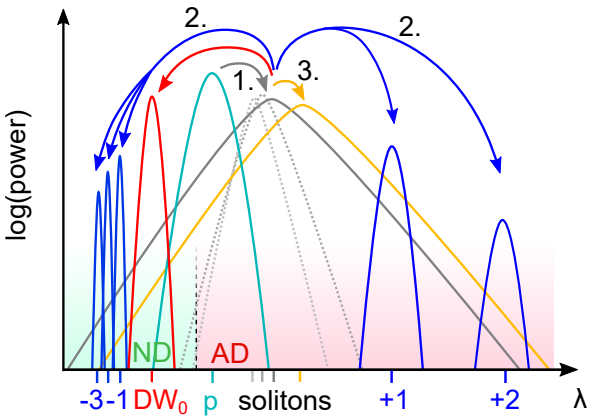

Figure 2.3: Conceptual schematic of the generation of spectral features in soliton-based SCG: 1. Formation of a higher-order soliton from the pump (p, turquoise) and optional soliton fission to multiple fundamental solitons (gray, secondary solitons are dashed). 2. Creation of the DW_0 (red) from the main soliton with the potential to form higher-order DWs (blue) via QPM. 3. Raman shift of the solitons (orange). The ND and AD domain of the fiber are indicated with light green and red backgrounds, respectively.

2.3.7 Cross phase modulation

In linear optics, all modes should be independent because of the mode orthogonality. Including nonlinear effects as discussed for SPM (Section 2.3.3), a pulse modifies the RI of the material it is passing though via nonlinear refraction and subsequently changes its own phase. This effect also works for different pulses which are traversing the same medium. For instance, high intensity light traveling in one optical mode can affect the propagation properties of other modes with low intensity not inducing nonlinear effects by themselves[152]. Analogously, this so-called cross phase modulation effect can also occur within one mode for spectral features at different wavelengths. The nonlinear effects of a soliton influences the propagation of its dispersive wave(s) and can result in a trapping of the DW at the same group velocity as the soliton[153].

2.3.8 Four wave mixing and modulation instability

One further family of nonlinear effect involves the interplay of four photons. In four wave mixing process energy can be converted between frequencies fulfilling energy conservation, i.e. a fourth photon created at ω_4 respecting the equation $\omega_4 = \omega_1 \pm \omega_2 \pm \omega_3$. This general notation includes the annihilation of two photons inducing the creation of two other photons, as well as one to three and three to one processes. Moreover, several photons participating can have the same frequency, leading to degenerated four wave mixing. With several peaks available in the spectrum generated by other effects, four wave mixing can lead to the generation of a plethora of new wavelengths in principle, limited by the required phase matching of all four photons, including the nonlinear phase. As four wave mixing is phase sensitive, exploiting QPM to tune the output wavelengths is possible[68,69].

One special case of four wave mixing is third harmonic generation, where three low energy photons are converted to one photon at triple the frequency. ECFs serve as an

efficient platform for third harmonic generation as phase matching is provided by the use of exotic higher-order modes[12]. Functionalizing ECFs with nano-films can enhance the conversion efficiency and enables tuning of the output wavelength[13,154]. Since this effect is well-studied elsewhere, the generation of green light from the pump at $\lambda_p = 1570$ nm is ignored in this work. However, it serves as a handy visible indication and helps optimizing good coupling to the small fiber core in experiments.

Considering the interplay between the nonlinear and dispersive effects, the generation of new frequencies from noise is called modulation instability. It can also be interpreted as a special case of degenerate four wave mixing. Here, there is only one pump wavelength involved, converting two of its photons into two unseeded sidebands symmetrical around the pump frequency[139]. MI classically occurs in AD domains, but can also be found in ND fibers for leaky modes[155] or in fibers with a negative fourth order dispersion[16]. Because MI does not require any additional intentional seeding, it is a powerful tool to initiate spectral broadening and is usually found in systems with high peak power and long pulse durations (sub-picosecond to nanosecond duration[156,157]). However, the requirement of the amplification of noise makes the prediction of the pulse evolution of individual pulses impossible, leading to a high shot-to-shot variation.

2.3.9 Nonlinear pulse propagation

The pulse dynamic in nonlinear media needs to be calculated to confirm the effects observed in experiments and to predict the behavior for hypothetical parameter changes. Linear pulse propagation can be calculated by solving the wave equation (Eq. 2.3) under the assumption of the slowly varying envelope approximation for a linear polarized field in the direction $\vec{e}$

$$\vec{E}(\vec{x},t) = 0.5\,\vec{e}/|\vec{e}|\,(A(\vec{x},t)\exp(-i\omega t) + \text{complex conjugated})\,. \tag{2.24}$$

The wave equation is based on the first order approximation of Eq. 2.9 and needs to be expanded to include nonlinear terms. While keeping the slowly varying envelope approximation in the time domain as well as the Fourier transformed frequency domain, further approximations are introduced. For instance, nonlinear loss is neglected and the nonlinear terms are treated as a small perturbation of the linear system at ω_0. Thus, the nonlinear RI of materials n_2 are only evaluated at a single wavelength without dispersion. Furthermore, the fields are assumed to be transversal and the effective mode area non-dispersive. With a Taylor series of the dispersion, nonlinear pulse propagation can be described by the generalized nonlinear Schrödinger equation (GNLSE). Different assumptions and approximations allow for various versions of pulse propagation equations that are derived from the original form of the wave equation (Eq. 2.2) and discussed in detail in Ref. 158. The GNLSE used in this work is the one given by Dudley et al.[139] and can be expressed in a co-moving time frame compared to the group velocity of the pump pulse as

$$\frac{\partial A}{\partial z} + \frac{\alpha}{2}A - \sum_{k\leq 2} \frac{i^{k+1}}{k!}\beta_k \frac{\partial^k A}{\partial t^k} = i\gamma \left(1 + i\tau_{\text{shock}}\frac{\partial}{\partial t}\right)\left[A(R * |A|^2)\right], \tag{2.25}$$

with α being the absorption constant and * signaling a convolution with the nonlinear response function $R(t) = (1 - f_R)\delta(t) + f_R h_R(t)$. The response function consists of an instantaneous electronic response with the Dirac delta function plus the Raman contribution with the silica Raman fraction $f_R = 0.18$ and the Raman response function h_R[159].

The GNLSE version in Eq. 2.25 assumes a wavelength independent intensity. More realistically, longer wavelength have a larger effective mode field area A_{eff} in fibers, reducing the peak intensity. One definition of A_{eff}, also used by Agrawal[18], consists of area integrals over the electric field distribution $\vec{E}(\vec{x}, \lambda)$:

$$A_{\text{eff}}(\lambda) = \frac{(\int |\vec{E}(\vec{x}, \lambda)|^2 dA)^2}{\int |\vec{E}(\vec{x}, \lambda)|^4 dA} \tag{2.26}$$

The dispersion of A_{eff} can be added to the GNLSE by modifying the shock term responsible for higher-order nonlinearities[160]

$$\tau_{\text{shock}} = \frac{1}{\omega_0} + \frac{d}{d\omega}\left[ln\left(\frac{1}{n_{\text{eff}}(\omega)A_{\text{eff}}(\omega)}\right)\right]. \tag{2.27}$$

Nonlinear pulse propagation calculations are implemented in numerical simulations via solving the GNLSE (Eq. 2.25) with a split-step method. The code used in this work is based on the one published by Dudley and Taylor[156] with the additional correction for the mode area dispersion (Eq. 2.27). Using the raw dispersion data $n_{\text{eff}}(\omega)$ of the fundamental mode calculated as described in Section 2.1, the full dispersion is included without the need of a finite Taylor expansion. These simulations account for all possible nonlinear effects described in the Sections 2.3.1 to 2.3.8 within one mode and therefore can predict the pulse dynamics and the spectral evolution along the fiber. Taking the value of the nonlinear parameter γ at a central frequency only, e.g. the pump frequency, is a commonly used approximation. In cases with a strongly Raman-shifting soliton being the cause for nonlinear effects, it can be helpful to vary γ along the pulse propagation to account for the value at the local soliton frequency. Hence, tracking of the soliton wavelength and updating γ is implemented for the simulations in the Section 5.3.

2.3.10 Frequency resolved optical gating

The results of the nonlinear pulse propagation simulation are the spectrum and the temporal shape of the pulse at different positions along the fiber. However, the connection of both data sets is missing, i.e. which part of the spectrum corresponds to which temporal feature (spectrogram). Completing the full characterization of short pulses could be done experimentally by capturing frequency resolved optical gating (FROG) traces. It consists of splitting a pulse into two parts, interfering them with each other with a tunable relative time delay in a nonlinear crystal, and measuring the resulting spectrum[161]. In simulations,

intensity FROG traces can be obtained by multiplying the solution of GNLSE calculations in time $A(t)$ with an arbitrary time gate $A_g(t)$ with different delays τ and transforming it to the frequency domain with an inverse Fourier transform (IFT) as introduced by Xu et al.[162]

$$I_{\mathrm{FROG}}(\tau,\omega) = \left| \int A(t) A_g(t-\tau) \exp(-i\omega t) dt \right|^2 . \tag{2.28}$$

The gate function heavily influences the resulting spectrogram, leading to an enhanced spectral resolution for wider gates and a better temporal resolution for narrower gates. In this work, the shape of the gate is chosen to be sech squared, imitating the interference with an experimental probe pulse.

2.3.11 Coherence of supercontinuum sources

When considering a pulsed light source, one important characteristic is its consistency, that is the pulse-to-pulse stability, also named coherence. Usually, spectroscopic applications only require measuring material responses that are mostly independent of the actual spectral power density and fluctuations of the optical pulses are averaged out. However, fast scanning applications or the realization of precise frequency combs[163] depend on the spectral properties of a few or even single pulses that might vary from each other, thus, demanding high coherence. The coherence can be measured experimentally by interfering two independently generated pulses and observing the fringe visibility[164].

A lack of coherence can be caused by frequency broadening mechanisms that depend on noise, for example MI, or appear for highly power sensitive effects such as higher-order soliton fission[55,56]. Therefore, the coherence can be probed by including random noise in simulations and comparing the final spectrum of different runs. One commonly used noise model is the one-photon-per-mode model[165], which adds one photon per simulated frequency bin with random phase. This is enough to characterize the pulse stability in MI systems. On top of it, the shot noise of the pump laser concerning pulse energy, peak power, and pulse duration can be included in the simulations. In this work, a set of 20 individual simulations is considered, with 190 unique combinations of electric fields $E_{\mathrm{i,j}}(\lambda)$; i, j = 1,2,...,20; i $\neq$ j. Defined by Dudley and Coen[166], the first-order degree of coherence $|g^{(1)}_{\mathrm{i,j}}|$ can be calculated as

$$|g^{(1)}_{\mathrm{i,j}}(\lambda)| = \frac{\langle E^*_{\mathrm{i}}(\lambda) \cdot E_{\mathrm{j}}(\lambda) \rangle}{\sqrt{\langle |E_{\mathrm{i}}(\lambda)|^2 \rangle \langle |E_{\mathrm{j}}(\lambda)|^2 \rangle}}, \tag{2.29}$$

where $\langle X \rangle$ refers to an ensemble average over many independent spectra. A full characterization of the coherence also requires higher-order terms[167], which are ignored in the scope of this work.

3 Dispersion modification concept using nano-films

For precise control of nonlinear frequency conversion in fibers, tailoring the dispersion of waveguides is the key to success (Section 2.2). In this work, the dispersion is influenced post fiber drawing by the novel concept of introducing nano-films in direct contact with the core. After a general discussion of the requirements for the nano-films in the next paragraph, the effectiveness of the concept is tested on a slab waveguide in simulations (Section 3.1). Then, the influence of nano-films on the dispersion of ECFs is analyzed and the dispersion characteristics using different nano-film geometries, having a thickness gradient or periodic structures, are evaluated in Section 3.2.

Compared to the size of the core of the ECFs with an inscribed circle diameter of 1.75 µm, thin nano-films with thicknesses of $t = 50$ nm to $t = 100$ nm do not seem to make a huge difference from a geometric point of view. Therefore, material properties such as the nonlinearity should not have a large impact on the properties of the entire fiber. Notably influencing the optical properties of the fibers is only possible by introducing strong resonances to the system. These resonances appear in the form of optical modes, bound by the dielectric and transparent nano-film itself. The concept is similar to Bloch waves bound to a nano-film stack on D-shaped fibers[168], but with a strong interaction with the modes of the original core. This is solely possible with nano-film materials having a high RI, as confining modes to the nano-film requires a high RI contrast to the surrounding material, i.e. the silica core. A lower RI contrast to the core material increases the required nano-film thickness to achieve a similar effect as analyzed in Section 3.2.1. Materials with a lower RI than the core material just replace the air cladding of uncoated fibers with another type of cladding. This will slightly increase the mode field diameter, effectively behaving similar to geometric size tuning discussed in Section 2.2.2. Although the dispersion of the mode field diameter and the different fraction of the evanescent field in the low-RI cladding will cause some modification of the fiber dispersion, it is not as strong as with high RI nano-films. This work only evaluates the strong dispersion tuning with high RI nano-films.

3.1 Anti-crossing in a slab waveguide

For a better understanding of nano-film resonance-driven dispersion modification and its potential, a simple one dimensional model of a slab waveguide is analyzed, first. This model consists of a infinitely extended silica layer with a similar thickness (1.7 µm) compared to the inscribed circle diameter of the real fiber (1.75 µm), embedded within air layers simulating the capillary holes of the fiber. On one side of the waveguide there is a thin

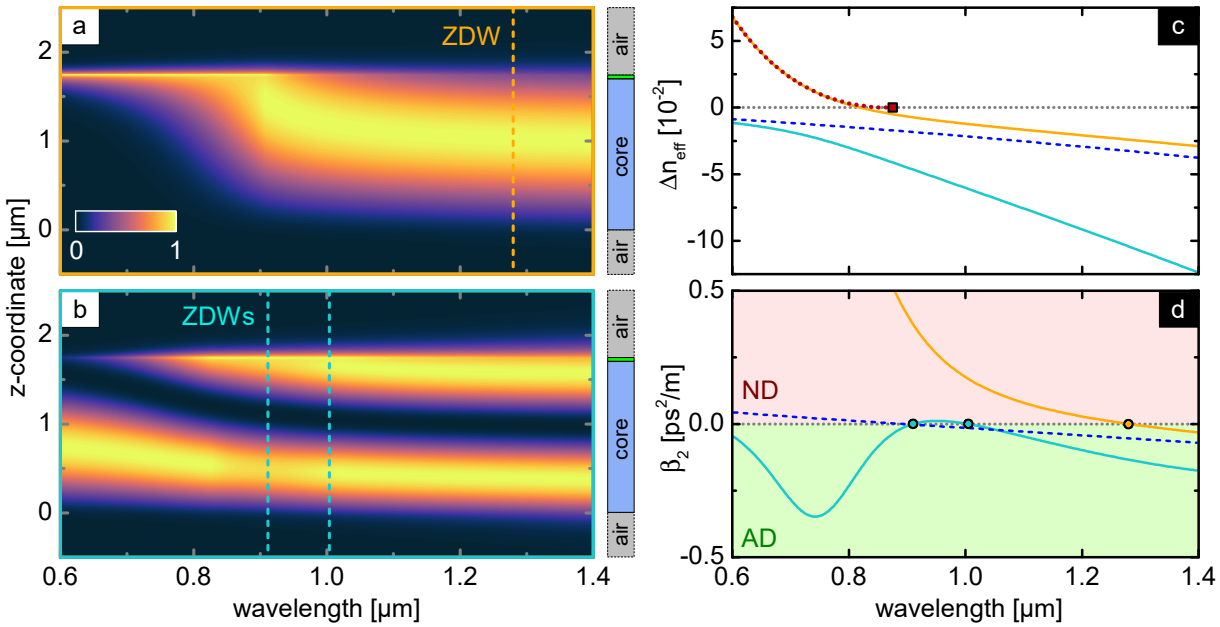

Figure 3.1: Wavelength dependent normalized electric field distribution of the (a) fundamental and (b) higher-order mode of the 1D model shown to the right of both plots (silica core width: 1.7 µm, TiO_2 nano-film thickness: 40 nm, light green). (c) Effective indices of the fundamental mode (orange), higher-order mode (turquoise)(color-matched to the frame of (a+b)), mode of the core without any nano-film (blue, dashed) and pure nano-film mode (silica/TiO_2/air structure, red, dotted). The red square marks the cut-off of the nano-film mode. All values are normalized to the refractive index of silica $\Delta n_{\text{eff}} = n_{\text{eff}} - n_{\text{silica}}$. (d) β_2 of some modes of (c). The ZDWs are marked with circles on the zero-crossing, dividing the plot in a normal dispersive (ND, red) and anomalous dispersive (AD, green) domain.

layer of TiO_2 with a width of $t = 40$ nm representing the nano-film in fibers (schematics to the right of Fig. 3.1a+b).

The electric field distribution of the fundamental mode of the slab waveguide with transversal electric polarization is displayed in Fig. 3.1a. This is a mode based on hybridization of two other modes. At long wavelengths ($\lambda > 1$ µm), the hybrid mode is similar to the fundamental mode of the waveguide without any nano-film. Thus, their effective refractive indices, displayed as the difference to the one of silica ($\Delta n_{\text{eff}} = n_{\text{eff}} - n_{\text{silica}}$), are similar (orange solid and blue dashed lines in Fig. 3.1c, respectively). At shorter wavelengths, the hybrid mode transitions towards the mode inside the thin film. The nano-film, seen as an individual waveguide with one air and one silica cladding side, has a modal cut-off at $\lambda_{\text{cut}} = 868$ nm (red dotted line and red square). When the hybrid mode has a considerable part of its power located within the high index material, its effective mode index increases notably.

The first higher-order mode with the same polarization direction (transversal electric) is shown in Fig. 3.1b and its effective mode index is represented by the turquoise line in Fig. 3.1c. At longer wavelengths, this mode has a large fraction of its power close to the nano-film. Around the same wavelength of the mode transition of the fundamental

hybrid mode, near $\lambda = 800$ nm, the second order mode becomes the new fundamental-like core mode for shorter wavelengths. Considering the electric field distribution, the fraction near the nano-film decreases and, simultaneously, the effective index of the higher-order mode approaches the one of the nano-film-free fundamental mode (dashed blue line). In total, the exchange of the properties and the shape of the field distribution can be seen as anti-crossing of optical modes, similar to anti-crossing of energy bands in crystals [169,170].

The introduction of anti-crossing through nano-film-induced resonances also impacts the GVD of all modes involved as depicted in Fig. 3.1d. Without any nano-film, the slab waveguide has a ZDW of $\lambda_{\mathrm{ZD}} = 920$ nm. As the nano-film is introduced, bending up the effective index curve of the fundamental mode influences its curvature, i.e. the GVD. In particular, the ZDW shifts towards longer wavelengths for increasing nano-film thicknesses, in this example by more than 300 nm. Because the pump laser is located in the telecommunication regime, it is sufficient to restrict the discussion to the long-wavelength side of the resonance and focus on the fundamental mode.

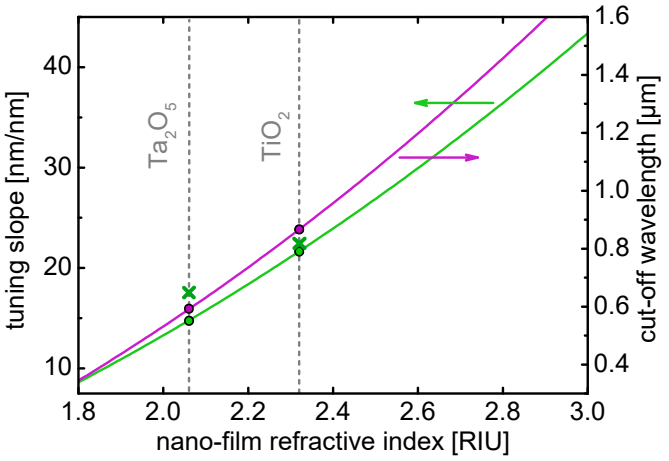

Figure 3.2: Cut-off wavelength of the nano-film mode (red square in Fig. 3.1) and the resulting tuning slope potential of nano-films with different RIs using the 1D model (arrows point to their axis). Green crosses mark values for the ZDW tuning slope calculated with the detailed 3D model (Fig. 3.4). Dashed lines mark the RIs of the used materials at $\lambda_p = 1.57$ µm.

To estimate the tunability of the dispersion dependent on the nano-film thickness t and its potential considering other nano-film materials, the cut-off wavelengths of the pure nano-film mode can act as an indicator[1]. Following the theory as presented in a book by Okamoto [171], the normalized cut-off wavelength of the fundamental mode in transversal electric polarization of a slab waveguide with asymmetrical cladding, here composed of air (n_a) and silica (n_b), is given by

$$V_{\mathrm{cut}} = 0.5 \arctan\left(\sqrt{\delta}\right), \tag{3.30}$$

with the asymmetry parameter $\delta = (n_b^2 - n_a^2)/(n_{\mathrm{co}}^2 - n_b^2)$. Using the definition of the normalized frequency $V = \pi t/\lambda \cdot \sqrt{n_{\mathrm{co}}^2 - n_b^2}$, Eq. 3.30 can be rewritten as

$$\lambda_{\mathrm{cut}} = \frac{2\pi t \sqrt{n_{\mathrm{co}}^2 - n_b^2}}{\arctan\left(\sqrt{\delta}\right)}. \tag{3.31}$$

[1]The following model is found and applied to the presented case by Markus Schmidt

Equation 3.31 suggests both a longer cut-off wavelength as well as a higher tuning slope $m_{\mathrm{cut}} = d\lambda_{\mathrm{cut}}/dt$ (unit: nm wavelength tuning per nm nano-film thickness) with increasing RI of the nano-film, visualized in Fig. 3.2. Thus, nano-films with even higher RI such as chalcogenides or semiconductors can be desirable for this tuning method. Interestingly, the modeled tuning slope is independent of the nano-film thickness and matches well with the measured tuning slopes of the ZDW (presented in the Section 3.2), verifying the appropriateness of this model and the use of the cut-off wavelength as an indicator.

3.2 Dispersion management in nano-film-enhanced ECFs

The dispersion of fibers is one fundamental aspect for nonlinear frequency conversion and can be retrieved by mode field simulations (Chapter 2). Moreover, it is required for predicting the spectral broadening and optimizing experimental nano-film parameters. Despite the success of the 1D model, more exact 3D simulations are essential when using complex fibers functionalized with nano-films. In the following, detailed dispersion tuning capabilities of nano-film enhanced ECFs are analyzed, in particular with a focus on the ZDW. On top of it, expanding the knowledge of optical properties to different nano-film geometries, i.e. nano-films having a thickness gradient or periodically structured nano-films, will boost the degrees of freedom to better tailor dispersive waves and the output spectrum.

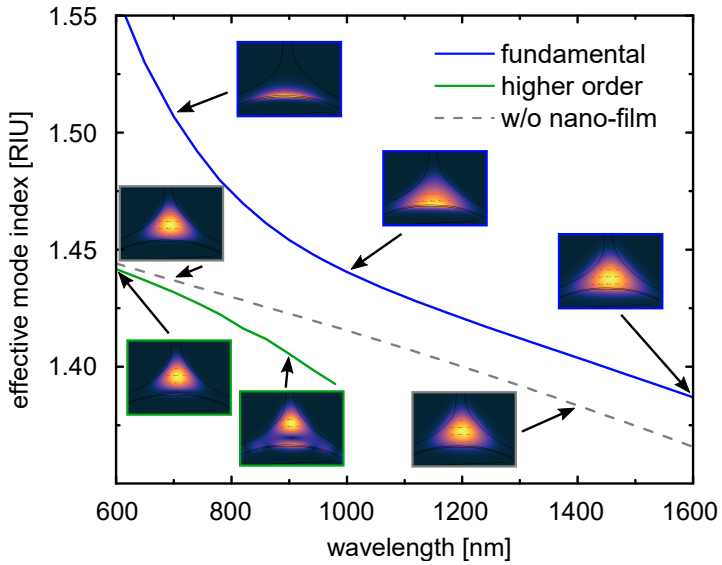

Figure 3.3: Effective mode index of the modes involved in anti-crossing in the ECF with a Ta_2O_5 nano-film with a thickness of $t = 70$ nm (blue: fundamental mode; green: higher-order mode, gray dashed: fundamental mode without nano-film. The insets show the normalized absolute electric field distribution of the modes at different wavelengths. All modes are polarized along the horizontal axis (red arrows).

3.2.1 Dispersion tuning with uniform nano-films

When considering the simplest case of a uniform nano-film with a constant thickness on an ECF, there are many similarities with the 1D model. For instance, the electric field distribution of all involved modes (calculated with a Finite Element method using COMSOL Multiphysics, Section 2.1) behaves analogously and also the anti-crossing shape of the effective index curves can be recognized (Fig. 3.3). Specifically, the fundamental mode (blue) transforms into a mode inside the nano-film, bending up the RI. Furthermore, a higher-order mode (green) approaches the fundamental mode without nano-film (gray, dashed), leading to the well-known anti-crossing structure. The modification of the dispersion of the fundamental mode is elaborated in detail for nano-films with different thicknesses and materials in Fig. 3.4.

For very thin nano-films ($t < 20$ nm for TiO_2), the anti-crossing position is spectrally too far away to bend the the RI curve in the spectral region of interest. This results in a constant offset of the effective mode index and does not influence its curvature, i.e. the GVD (Fig. 3.4b, calculated using Eq. 2.7). With an increasing nano-film thickness the anti-crossing shifts towards longer wavelengths, stronger influencing the effective index

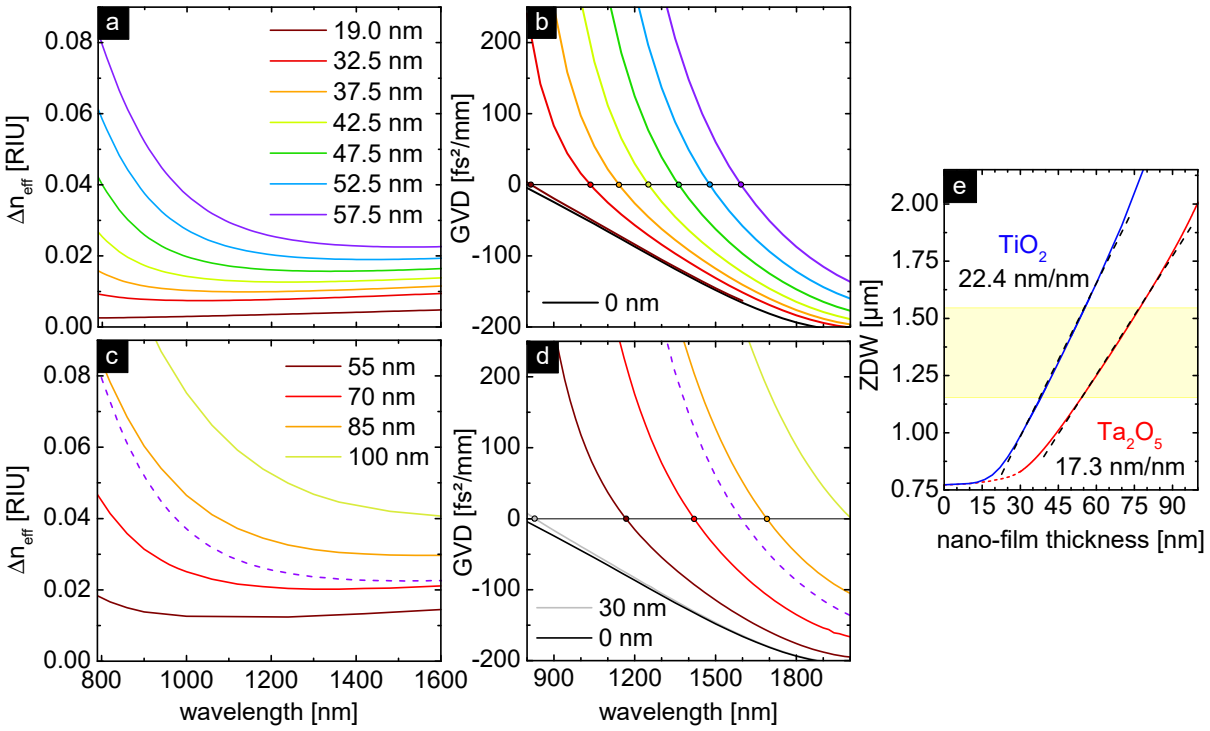

Figure 3.4: Modification of the effective mode index (a+c) and GVD (b+d) for different thicknesses of TiO_2 (a–b) and Ta_2O_5 nano-films (c–d). The effective mode indices are normalized to the refractive index of silica $\Delta n_{\text{eff}} = n_{\text{eff}} - n_{\text{silica}}$. In (c–d), the dashed curves are copied from (a–b) to ease the comparison with the TiO_2 nano-film with $t = 57.5$ nm. (e) Tuning slope of the ZDW (marked with circles in (b+d)) with respect to the nano-film thickness. Dashed lines represent linear fits and the experimentally relevant area for uniform nano-film thicknesses is highlighted in yellow.

and the GVD, and ultimately shifting the ZDW towards longer wavelengths. After an initial constant section at thin nano-films, the ZDW increases almost linearly (Fig. 3.4e).

When comparing the two materials used in this work, TiO_2 (Fig. 3.4a–b) and Ta_2O_5 (Fig. 3.4c–d), the effect of modulating the dispersion is qualitatively the same. Because Ta_2O_5 has a lower RI, thicker nano-films are needed to reach a similar increase of the GVD. For example, the GVD curve for the TiO_2 nano-film with a thickness of $t = 57.5$ nm (purple dashed curve) fits well within the set of Ta_2O_5 nano-film curves near the one with $t = 85$ nm (orange curve, Fig. 3.4d). One small difference is that because of the higher RI contrast to silica, TiO_2 has a slightly sharper resonance and thus the GVD is minimally steeper at shorter wavelengths. Considering the ZDW tuning, TiO_2 is more sensitive to the nano-film thickness at $\frac{\Delta\lambda_{ZD}}{\Delta t} = 22.4$ nm/nm. However, also Ta_2O_5 nano-films with $\frac{\Delta\lambda_{ZD}}{\Delta t} = 17.3$ nm/nm can shift the ZDW towards the telecommunications wavelength range.

With the ZDW being located closer to the pump wavelength while keeping λ_p in the AD domain (area highlighted in yellow in Fig. 3.4e), one prerequisite for efficient nonlinear frequency conversion is fulfilled. This sets the useful TiO_2 nano-film thickness range for uniformly deposited ECFs to 40 nm $< t <$ 60 nm.

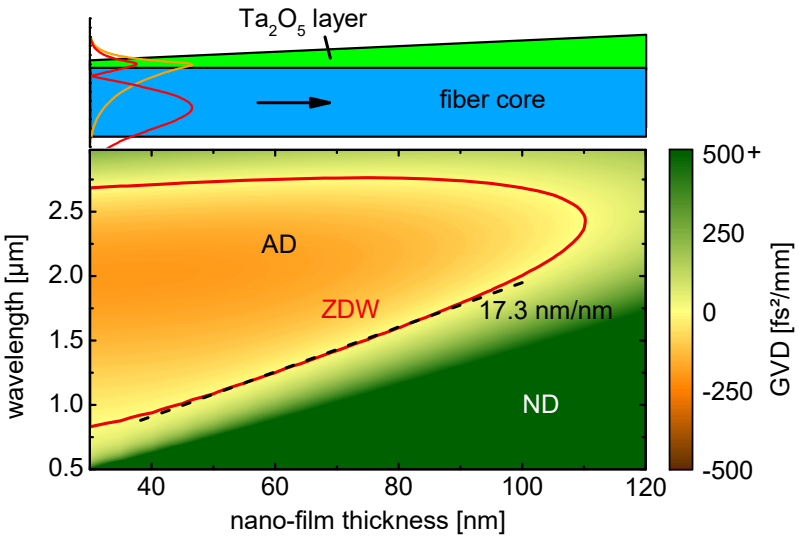

Figure 3.5: Top: Schematic of the longitudinal cross section of an ECF with a nano-film with increasing thickness along its length on its core. Orange and red curves represent the central cross section profile of the normalized absolute electric field of the fundamental and higher-order mode at $\lambda = 1120$ nm and $t = 100$ nm, respectively. Bottom: GVD landscape along a fiber having a Ta_2O_5 nano-film with a thickness gradient. The ZDW (red line) divides the plot into a normal dispersive (ND) and anomalous dispersive (AD) domain.

3.2.2 Dispersion of nano-films with a thickness gradient

When considering nano-films with a non-constant thickness along the fiber length, the dispersion can be tailored more freely. As this requires special deposition techniques discussed in Chapter 4, only Ta_2O_5 nano-films are considered in the following sections. Here, nano-films with a continuously increasing thickness along the fiber are considered as exemplarily sketched on top of Fig. 3.5. This leads to a locally changing dispersion of the fiber dependent on the actual, constantly varying nano-film thickness. Because of the increased resulting bandwidth (revealed in Section 5.3), the displayed nano-film thickness-dependent dispersion landscape has a wider wavelength range (Fig. 3.5). A second ZDW is revealed at long wavelengths near $\lambda = 2.7$ µm, that is spectrally far away from the resonance of the nano-film and thus is almost unaffected by it. As the first short-wavelength ZDW shifts towards longer wavelengths with increasing nano-film thickness or, analogously, increasing position along the fiber, it merges with the second ZDW at $t = 110$ nm. For thicker films there is no ZDW, making the fiber completely normal dispersive and unsuitable for soliton-based nonlinear frequency conversion.

3.2.3 Effective dispersion of periodically structured nano-films

Another possibility to shape nano-films to access new effects such as QPM (Section 2.3.6) is to periodically modulate their thickness. Here, this idea uses ECFs having alternating sections with and without being coated by a nano-film, forming a periodic structure with the pitch Λ in the mm scale. Comparing simulations of nano-films with alternating and with constant thickness, it is obvious that with the periodic modulation, thicker nano-films are needed to obtain comparable spectral positions of distinct spectral features. Consequently, both sections with and without coating contribute to the total nonlinear broadening, forming an effective material with optical parameters between the ones of the individual sections. The periodically coated fiber can be described by a uniform fiber which has a longitudinally invariant GVD, here, called 'effective dispersion' (GVD_{eff}). The effective dispersion is given by the second derivative of the averaged effective index of both coated (subscript w) and uncoated (subscript w/o) fiber sections with respect to the wavelength:

$$GVD_{\mathrm{eff}} = \frac{\lambda^3}{2\pi c^2} \frac{d^2 \left[n_{\mathrm{eff,w}}\, ff + n_{\mathrm{eff,w/o}} \left(1 - ff\right) \right]}{d\lambda^2} = GVD_{\mathrm{w}}\, ff + GVD_{\mathrm{w/o}} \left(1 - ff\right). \tag{3.32}$$

The contribution of both sections is weighted by their relative length, quantified by the filling fraction ff of the nano-film coated section with a length of l_{nf} in relation to the period length ($ff = l_{\mathrm{nf}} \,/\, \Lambda$). The equation is validated by simulations and experimental results in Section 5.4, though, the concept to use an averaged dispersion is also derivable using perturbation theory in combination with the nonlinear Schrödinger equation

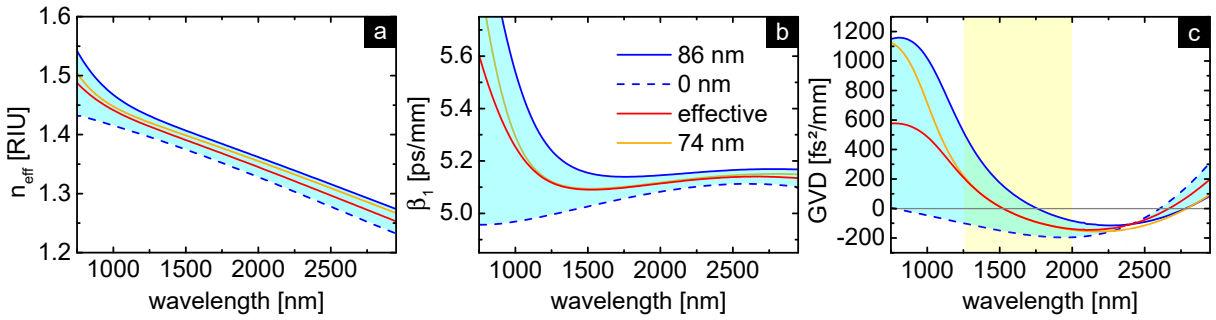

Figure 3.6: Effective mode index (a), β_1 (b) and the GVD (c) of ECFs with constant Ta_2O_5 nano-films of thickness $t = 86$ nm (blue, solid line) and $t = 0$ nm (blue, dashed line), spanning the possible cyan area if the thickness is modulated between those values. The red lines are the mean values of both blue lines (effective curves for $ff = 0.5$) whereas the orange lines show the values of a constant $t = 74$ nm thick nano-film, matching the effective GVD in a central, yellow marked area.

for dispersion-oscillating fibers for MI broadening[67,172]. Equation 3.32 implies a tuning possibility of the GVD_{eff} with *ff*, taking values between the GVD of an uncoated and a uniformly coated ECF. This tuning potential is visualized as a cyan area on the example of an alternating nano-film with thicknesses $t = 86$ nm and $t = 0$ nm in Fig. 3.6, showing the effective mode indices as well as their first two derivatives, β_1 and the GVD. With a filling fraction of half a period ($ff = 0.5$), the effective material curves (red) including the effective dispersion lie exactly in the center of the ones based on the individual sections of the alternating nano-film (blue, solid and dashed). Considering the GVD, which is decisive for nonlinear frequency conversion, the effective dispersion is similar to the dispersion of a uniformly coated ECF with a constant nano-film thickness of $t = 74$ nm (orange) from $\lambda = 1250$ nm to $\lambda = 2000$ nm. Hence, the broadened spectrum will be nearly identical for both cases in this central region, however, there will be differences in spectral regions further away from the center where the dispersion differs. With periodically modulating the nano-film thickness leading to an effective dispersion, the fiber has a completely new shape of its dispersion outside of the central area that cannot be reproduced by constant nano-films in the entire spectrum. Thus, this method expands the variety of possible dispersion landscapes and realizable multitude of nonlinear broadened spectra even without the QPM effect.

4 Nano-films for nonlinear applications

Thin layers with sub-micrometer thickness, here termed nano-films, have many applications including decorative and protective coatings. Besides uses in the semiconductor industry[173,174], thin layers are highly relevant in photonics for mirrors[175,176], anti reflection coatings[177,178], beam-splitters[179], and find application in devices from UV-coatings[180] to thin film solar cells[181]. Furthermore, they are neccessary for plasmonic applications in devices such as spectral filters[182,183], mode couplers[184], or sensors[185,186]. Concerning nonlinear optics, nano-films can be used as waveguides to enhance nonlinear effects through a high field confinement and the usage of highly nonlinear materials such as chalcogenides[187] or epsilon near zero materials[188,189]. For example, nano-films are utilized to enhance third[154] and high harmonic generation[190].

This chapter features sample fabrication in general. It first introduces the exposed core fibers used as substrates for nano-film deposition. After the description of the deposition processes used in this work in detail, some methods for the evaluation of the nano-films are elaborated.

4.1 Exposed core fibers

Exposed core fibers are microstructured fibers based on the concept of suspended core fibers[191]. At the joint of three struts having a width of a 280 nm to 480 nm, a triangular thicker section is formed which supports optical modes (Fig. 4.1, inset). This optical core with a diameter of its inscribed circle of 1.75 µm (dotted red circle) confines modes via total internal reflection at the interface to the three surrounding air sections. The thin geometry of the struts implies a large evanescent field in the air that reduces the effective index of strut modes. This incompatibility hinders the core mode from escaping through the struts and enables guidance.

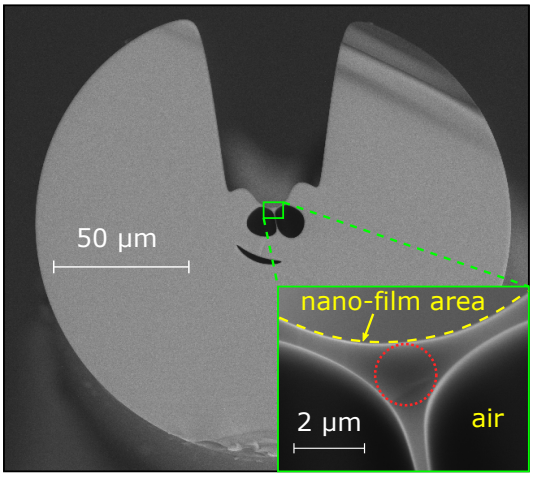

Figure 4.1: Scanning electron microscope image of the cross section of the ECF with a magnification of the core region in the inset. The red dotted line represents the inscribed circle of the triangular core with a diameter of 1.75 µm.

A large RI contrast between the core and the cladding materials usually is associated with a tight confinement of the mode. Yet, the concave curvature and the overall small size of the core enable an evanescent field inside the air region. This evanescent field has a large enough power for applications in sensing, as also used in fiber tapers[192,193], U-bend waveguides[194], and D-shaped fibers[195,196].

One of the three air sections surrounding the core is open to the environment at one side, exposing the surface of the core. This allows for accessing the core from the side of the fiber while simultaneously at least partly protecting the sensitive surface from contamination compared to fully open D-shaped fibers. The light matter interaction at that surface combined with the ability to externally manipulate and functionalize it via, e.g. depositing thin layers on top of the core, led to multiple applications of ECFs in sensing[197–203], biophotonics[19], and nonlinear optics[12,13,154,204].

Although different sections along the tens of meters long fiber from one fiber spool are utilized for various coatings, the cross section of the ECF varies only little and it can be practically seen as constant for all ECF samples discussed and simulated in this work (see Appendix, Fig. A.3).

ECFs are fabricated by first creating a suspended-core-fiber-like preform by extruding from stainless steel dies at high temperature and pressure[1]. Afterwards, one of the three air holes is cut open, followed by inserting the extruded preform into U-shaped wedged jacket. After aligning the cut air hole to the jacket opening, both are drawn to the final fiber as published by Warren-Smith et al.[198]. The bonding of the central preform and the jacket can be seen in form of their incomplete fusing, leaving an unintentional banana-shaped air hole which does not compromise the functionality of the fiber (Fig. 4.1).

The fact that the entire fiber is composed of silica simplifies the fabrication by eliminating thermal expansion, melting point, and viscosity discrepancies of composite material fibers and overall reduces mechanical stress. Furthermore, the well-known optical and nonlinear properties of fused silica ease simulations to more accurately predict nonlinear frequency conversion.

4.2 Nano-film fabrication methods

Nano-film fabrication is of great importance since not only the choice of the raw material, but also the used deposition technique and its parameters have a notable impact on the nano-film properties. Depending on the material composition and the desired geometrical and morphological properties, different fabrication methods can be used. All deposition methods are usually classified as (i) physical (vapor) deposition or (ii) chemical deposition process. Class (i) contains thermal and electron beam evaporation techniques, which are fast and highly directional, thereby enabling the creation of distinct patterns using physical masks[205]. Furthermore, slower deposition methods such as sputtering and pulsed laser deposition allow for the deposition of oxide and nitride materials via a reaction on the film surface[206]. Finally, electrohydrodynamic deposition involves material transport via micro-scale liquid droplets[207] and can lead to nano-films with tailored topographies.

[1]The fiber design and the drawing of the ECF used in this work was accomplished by Erik P. Schartner and Heike Ebendorff-Heidepriem.

In contrast to the methods where the raw nano-film components are deposited, class (ii) processes contain chemical reactions of precursors on the substrate to conformally form the final nano-film. This class contains the sol-gel method such as spin coating with liquid precursors[208], and chemical vapor deposition as well as plasma enhanced chemical vapor deposition with gaseous precursors[209]. Last but not least is the atomic layer deposition (ALD) method, here, a two step chemical vapor deposition process. It is slow, but ensures consecutive mono-layer deposition for nano-films with a uniform thickness with sub-nm precision[210].

In the following, the deposition of the two materials used in this work are described in detail. This includes high-precision uniform TiO_2 nano-films via ALD for the proof of concept study and tailorable Ta_2O_5 nano-films via sputtering to optimize the nano-film geometry.

4.2.1 Atomic layer deposition

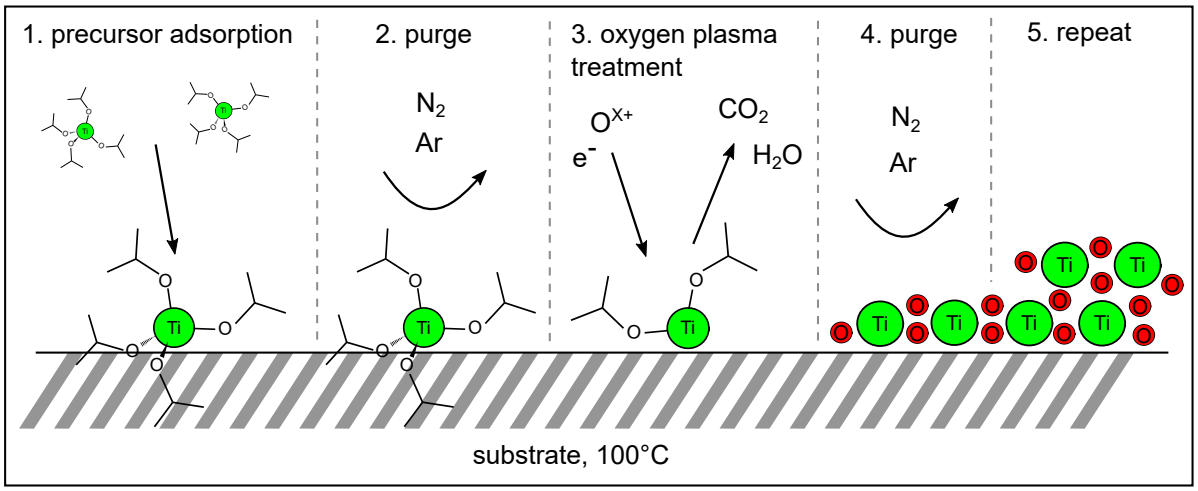

Figure 4.2: Schematic of the steps involved in the fabrication of TiO_2 nano-films using ALD with titanium isopropoxide and oxygen plasma precursors.

TiO_2 nano-films are fabricated using ALD (deposition machine: OpAL, Oxford Instruments) to ensure a uniform thickness along the entire fiber section with a length of up to 7 cm[1]. Moreover, it allows for a precise control of the nano-film thickness independent of the actual geometry of the microstructured fiber. Having the identical thickness, the nano-film dimensions and properties can be evaluated with measurements on a co-deposited planar substrates, placed next to the fibers. The ALD process consists of the consecutive deposition of mono-layers as sketched in Fig. 4.2. One deposition cycle consists of (1.) the adsorption of titanium isopropoxide from the gas phase and (3.) its reduction to TiO_2 using an oxygen plasma. The organic side groups get oxidized, forming, among others, carbon dioxide and water vapor. Between both steps the vacuum chamber and the plasma

[1] All TiO_2 nano-films fabricated with ALD were deposited by Sebastian Goerke.

source get purged with argon and nitrogen, respectively (2.+4.). During the deposition the substrate is kept at a temperature of 100°C, which ensures the formation of amorphous TiO_2 to avoid rough crystalline surfaces and grain boundaries to reduce scattering losses[211,212]. Having a cycle duration of 26.75 s, the growth rate is only 0.1 nm/min. In order to get a sample set with different nano-film thicknesses, several fibers are deposited simultaneously and are removed from the deposition chamber sequentially. For the experiments in this work one fiber was removed every 56 minutes.

4.2.2 Reactive magnetron sputtering

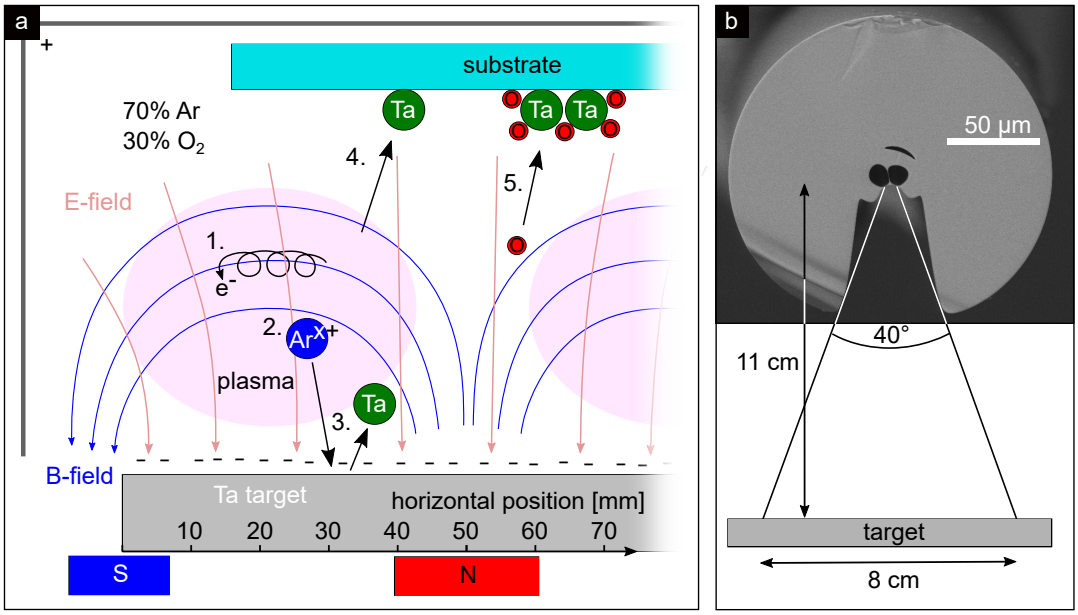

Figure 4.3: Schematic steps involved in the fabrication of Ta_2O_5 nano-films using reactive magnetron sputtering. A detailed explanation can be found in the main text. (b) Illustration of the sputtering acceptance angle of the ECFs.

For nano-films having a modulated thickness along the fiber length, especially for nano-films with a thickness gradient, uniform deposition methods are disadvantageous and switching to directional methods is advised. Direct current reactive magnetron sputtering of Ta_2O_5 offers high reliability and flexibility owing to the free substrate placement opportunities. The process is schematically schematically presented as a cross section of the rotational center symmetric setup in Fig. 4.3a. The tantalum target is charged negatively and is located above concentric permanent magnets generating a doughnut shaped magnetic field. Having a gas pressure of 0.5 Pa with 70 % argon content is sufficiently high to ignite a plasma. The electrons of the plasma, repelled by the charged target, are confined by the magnetic field lines (1.) and keep the plasma area close to the target. A more detailed analysis of the electron trajectories and the entire magnetron sputtering process is summarized by Anders[213]. Contrarily, positively charged argon ions accelerate in the electric field towards the target (2.) and eject tantalum atoms by means of collision

(3.). Next, the tantalum atoms get deposited on the substrate (4.) and are oxidized by oxygen radicals and ions[214] (5.), originating from the remaining 30 % O_2 content of the atmosphere.

As sputtering is mostly directed, the fiber geometry and potential shielding effects need to be considered. Although some collisions of the Ta atoms with the sputtering gas happen and cause redirections, here, only the direct, straight trajectory from the target to the substrate is considered. When being aligned perfectly to the target, the acceptance angle of 40° of the ECF is wide enough to collect Ta atoms originating from all over the target with a diameter of 8 cm only if the fiber is located at least 11 cm away from the target (Fig. 4.3b). With a minimum distance of 12 cm in experiments, unproblematic deposition should be guaranteed. However, slightly misaligning the fiber's rotational orientation and the neglected gas collisions present in the real experiments will reduce the nano-film thickness on the fiber core compared to a planar substrate at the same position. This relative difference caused by partial shielding due to the slot geometry of the ECF is the definition of the correction factor f_c, which is individual for each coated fiber.

Owing to the non-conformal nature of the sputtering method, only the central region of flat substrates gets coated uniformly with a decrease of the nano-film thickness to all sides. Figure 4.4 shows the spatial dependence of the nano-film thickness along a central cross section of a planar Si substrate positioned at two different distances from the target, measured with a P-10 surface profiler, KLA-Tencor Corp.[1] The further away the substrate is, the more uniform it will be coated at the expense of nano-film growth speed. This feature, which is undesired for most coating applications[215] and countered by, for example, magnet wobbling[216], can be exploited in case non-uniform nano-films are desired. Although placing samples off-center would give a nano-film with a thickness gradient, this technique is not supported by the available room and the setup inside the deposition chamber. Furthermore, the tunability of the nano-film shapes along longer samples is limited.

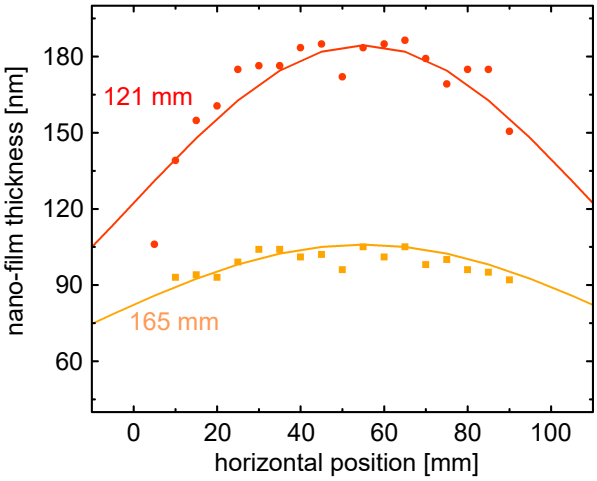

Figure 4.4: Experimental (points) and modeled (line) thickness distribution of a Ta_2O_5 nano-film along a substrate parallel to the target at substrate-target distances of 121 mm and 165 mm.

Instead, the concept to create nano-films with thickness gradients is to place the samples at a defined angle φ inside the magnetron deposition chamber (Fig. 4.5). This posi-

[1] All Ta_2O_5 nano-films were deposited by Henrik Schneidewind and these two thickness profiles are measured by him.

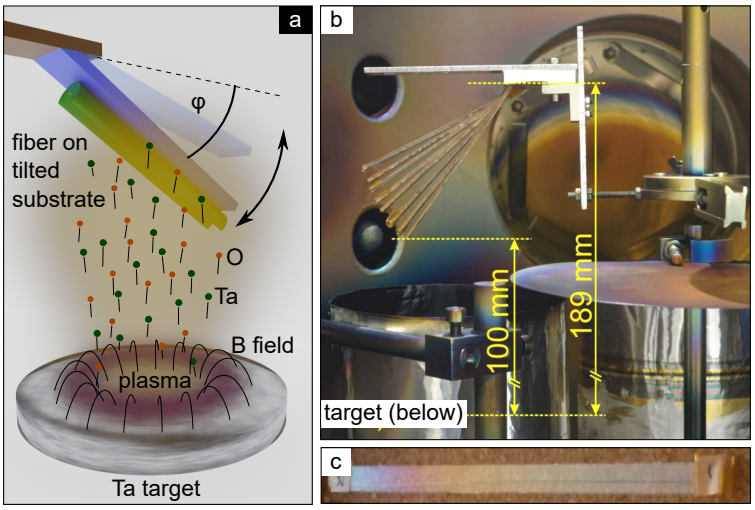

Figure 4.5: (a) Schematic illustration of tilted reactive magnetron deposition to realize nano-films having a thickness gradient. (b) Photograph of a set of fibers mounted on a custom sample holder at different angles in the deposition chamber. (c) Photograph of an ECF taped to a Borofloat 33 substrate with a length of 10 cm, coated with a nano-film with gradually increasing thickness to the left.

tions parts of the sample closer to the target, where the deposition rate is higher. However, the distance to the target is only one aspect of tilted deposition, which needs a more sophisticated model. The model is based on work by Fan et al.[217], adapted for angled substrates[218] as used by Yu et al.[219], and applied to our deposition situation.

The core of the model is an integral, summing up the contribution of every infinitely small area dA on the target to the nano-film thickness at one point of the substrate $t(\vec{x})$. Note that deflections of atoms due to collisions in the sputtering gas are neglected. All elements of the model are sketched in Fig. 4.6a. First, owing to the doughnut shaped plasma, the target is not ablated uniformly. Therefore the integral is weighted with the erosion function $Er(\vec{r})$, which is visually evaluated to be radially symmetric and has non-zero values only at the radius of the target $r_{\min} < r < r_{\max}$ with $r_{\min} = 1$ cm, $r_{\max} = 4$ cm, and a maximum value of Er at $r = 3$ cm. This behavior is empirically modelled by a Poisson-distribution shaped function (green curve in Fig. 4.6a) including the gamma function Γ

$$Er(r) = \left[1.5^{\frac{2\ \mathrm{cm}^{-1}(r_{\max}-r)}{\Gamma(2\ \mathrm{cm}^{-1}(r_{\max}-r))}} + 0.0045\ \mathrm{cm}^{-1}\,(r - r_{\max})\right]^{1.5}. \tag{4.33}$$

Independent of the position on the target, the ejected Ta atoms are assumed to have the same angular emitting distribution $H(\psi) \propto \sin(\psi)^{\mathrm{p}}$ (Ref. 217), peaking at perpendicular ejection from the target and vanishing for grazing emittance. Along the straight flight to the substrate, the deposition rate decreases quadratically with ρ and upon reaching the substrate the incidence angle θ induces another $\cos(\theta)$ factor. The latter is one of the reasons why the side walls of the ECF groove have a significantly thinner nano-film thickness (green inset of Fig. 4.6b). All effects merge to the final equation for the local

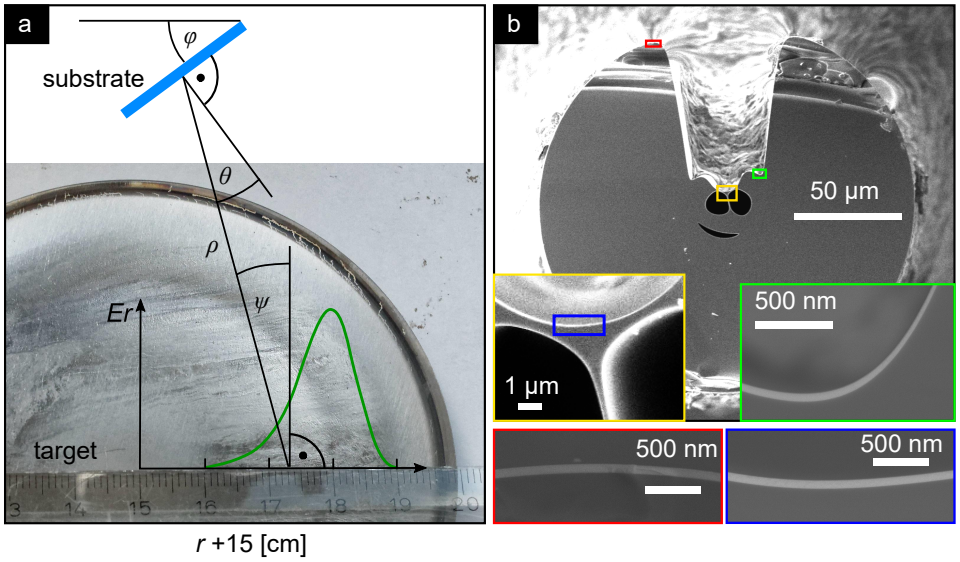

Figure 4.6: (a) Schematic model of tilted magnetron sputtering introducing all significant parameters (explained in the main text) with a photograph of the tantalum target. (b) SEM of the coated ECF with magnified insets showing the Ta_2O_5 nano-film thickness at different positions.

nano-film thickness on the substrate, with H_0 being a factor proportional to the sputtering time and including the normalization of $H(\psi)$.

$$t(\vec{x}) = H_0 \int_{Target} \frac{Er(\vec{r})H(\psi)\cos(\theta)}{\rho^2} dA \tag{4.34}$$

The remaining model parameters p = 2.51 and $H_0 = 0.014\ s^{-1}$ are set by fitting the model to experimentally deposited thicknesses of Ta_2O_5 layers on two Si wafers positioned parallel to the target at distances of 121 mm and 165 mm (Fig. 4.4). At these distances the initial doughnut shaped emission pattern is washed out, resulting in a single-peaked shape. The angle φ is only relevant for experimental positioning of the substrate and the alignment of the substrate relative to the center of the target is kept as a variable while fitting experimental data with the model.

Apart from scattering in the sputtering gas, other effects happening on the substrate side are also neglected, including resputtering of deposited material, reflection of Ta atoms at the substrate, as well as biased and kinetic energy assisted diffusion [220].

4.3 Nano-film evaluation

4.3.1 Ellipsometry

Ellipsometry is a precise method to measure the complex refractive index including the absorption and the thickness of planar thin films on defined planar substrates. It is based on the polarization resolved measurement of the reflected light intensity at different wavelengths from an incoming beam with a variable specific incident angle [221]. The incident

beam is polarized 45° with respect to the beam plane to equally include both transversal electric and magnetic components. The resulting experimental data of the reflected beam is fitted with a complex model using the Fresnel reflection and transmission coefficients at each interface. The model includes interference effects from reflections at different interfaces and all materials are defined by physical or mathematical dispersion models, for example the Sellmeier, Cauchy, or Drude-Lorentz model. During the calculation, the parameters of the dispersion models and the width of the layers are varied until they form a system which matches the measured reflection properties best. This method is dependent on and limited by the actual dispersion model used as a base for the calculations. Because of the potentially large amount of fitting parameters, ellipsometry works best if most of the materials involved, especially the substrate, have a fixed given dispersion.

Within the spectral interval of 400 nm $< \lambda <$ 2300 nm and a joint fit using data from all incident angles of 50°,60° and 70°, the dispersion of TiO_2 films is measured with a type SE850 ellipsometer (Sentech Instruments GmbH). Using a third order Sellmeier equation

$$n^2 = 1 + \sum_{i=1}^{3} \frac{A_i \cdot (\lambda/\mu m)^2}{(\lambda/\mu m)^2 - B_i} \tag{4.35}$$

and assuming a 2 nm thin native oxide layer on the silicon substrate[222–224], the parameters are determined to be $A_1 = 6.393$, $A_2 = -3.976$, $A_3 = 1.337$, $B_1 = -0.08330$ µm², $B_2 = -0.2736$ µm², and $B_3 = 0.1097$ µm². The dispersion values of the substrate are taken from the ellipsometer fitting program library (SpectraRay, Sentech Instr., 'SiO (Palik)', 'Si (Hertziger)'). Because the fitting uncertainties add up to an error of $\Delta n = \pm 0.05$ RIU for $\lambda > 500$ nm, the result falls well into literature values of similarly fabricated layers[225] (Fig. 4.7).

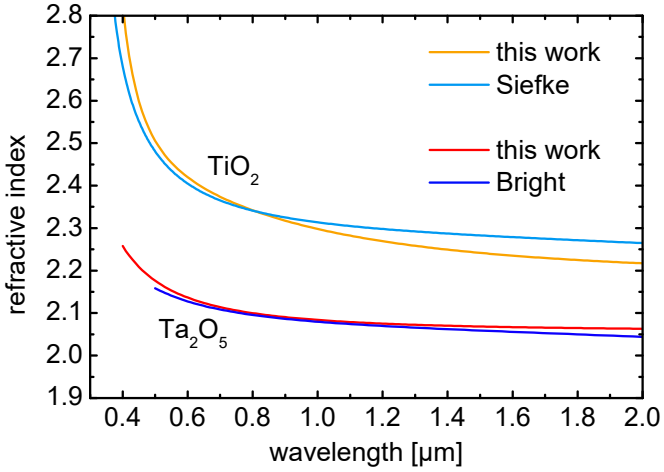

Figure 4.7: Measured refractive indices (via Ellipsometry) of the used nano-films in comparison to literature values of Siefke et al.[225] and Bright et al.[226]

Analogously, the dispersion of Ta_2O_5 nano-films is measured on Borofloat 33 substrates resulting in the Sellmeier formula $n^2 = 1 + 3.2289/[1 - 33929 \cdot (\lambda/\mathrm{nm})^{-2}]$ (substrate:

SpectraRay 'Borofloat 33'). With $\Delta n = \pm 0.06$ RIU dependent on the deposition geometry, layer thickness, substrate angle during deposition, measuring angle, and the fitting method this is also in accordance with literature values[226–228]. Variations in the nano-film dispersion, especially compared to the films deposited in other facilities, can be caused by varying argon concentrations within the film[229], different stoichiometry[230] or morphology, and void formation at high incident angles θ.

All results of ellipsometry are averaged values within the elliptic spot size of the incident beam, being about 1 mm × 3 mm. For a more precise geometrical evaluation of the nano-film other methods need to be used.

4.3.2 Stylus profilometer

A stylus profilometer scans the surface profile of a sample by a cantilever tip being dragged in contact with the material along its surface. Either the force applied to the cantilever holder or the displacement of the tip can be measured.

The surface roughness of a Ta_2O_5 nano-film is measured with an atomic force microscope to be ∼0.2 nm RMS on a 2.5 µm^2 area (magnified area in Fig. 4.8[1]). However, including the bigger particles that are randomly spread across the surface, height variations up to 25 nm can be observed. Although these imperfections are undesired and increase scattering losses, the nano-films still allow for analyzing nonlinear frequency conversion. Potentially, the nano-film morphology could be improved by adapting a surfactant sputtering technique[231,232] or switching to high-power impulse magnetron sputtering[213].

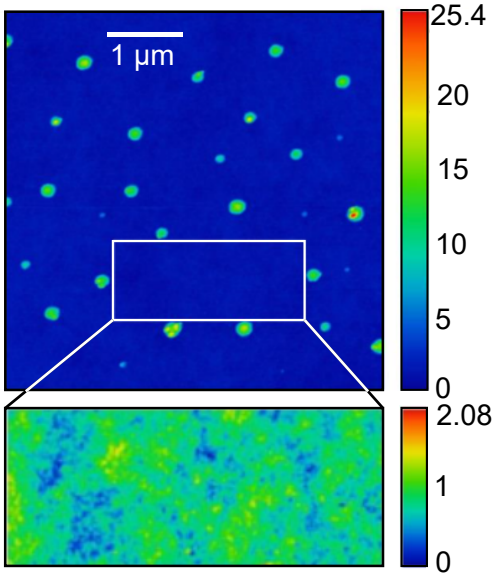

Figure 4.8: Atomic force microscope image of the Ta_2O_5 nano-film measuring the surface height profile. The inset shows a magnified section without bigger particles (1 µm × 2.5 µm). Both color bars represent the nano-film height in nm.

4.3.3 Scanning electron microscopy

A SEM image is based on measuring directly reflected or secondary electrons of an electron beam scanning the sample. To avoid electric charge build-up of the sample, it needs to be coated with a thin conducting layer, e.g. carbon. The electron scattering properties of different materials make SEM sensitive to the local atomic number of the sample and allows for the measurement of the nano-film thickness in a cross section view (Fig. 4.6b). For

[1]Measured by Henrik Schneidewind

this work, the thickness measured with ellipsometry is used owing to the non-destructive nature of optical measurements. However, as SEM is the only method available to check the nano-film profile on curved fiber surfaces, it is an excellent tool to confirm the measurement of other methods on planar substrates and to verify the f_c values.

For two fibers coated with different thicknesses, $t \approx 81$ nm and $t \approx 135$ nm, the nano-film thicknesses on the core of the ECF (blue area in Fig. 4.6b) and the outside of the ECF (red area) are measured. Their ratio leads to $f_c = 0.9$ and $f_c = 0.85$ and considering the ratio of on-core thickness to the one measured with an ellipsometer on a co-deposited separate planar glass sample it is 0.84 and 0.79, respectively. These values are only measured at one specific distance to the sputtering target and two samples are not enough to get statistically relevant information, but they confirm the plausibility of the f_c values that are later determined by fitting simulated spectra to experiments.

4.3.4 Linear transmission

The surface roughness of the nano-film measured with the atomic force microscope and material imperfections that can be indirectly detected with ellipsometry lead to optical losses of the coated fiber. The loss is the experimentally relevant parameter and it can be evaluated via transmission measurements through the coated fibers using a broadband light source at low peak power to not introduce any nonlinear effects. Compared to the reference measurement of an uncoated fiber, the linear transmission of nano-film enhanced fibers are dominated by a broad dip near the anti-crossing wavelength. This can be directly connected to a low coupling efficiency to the distorted fundamental mode and higher losses of higher-order modes (Fig. 3.3). In order to measure the losses along the fiber without the influence of the incoupling efficiency a cut-back method (e.g. as applied in Ref. 233) needs to be used. This reveals specific losses related O–H absorption features, e.g. near $\lambda = 1.4$ µm, and a base-line absorption of (10–20) dB/m for Ta_2O_5 nano-films. The detailed loss analysis and the influence on the broadened spectrum is discussed in Sections 5.3.6 and 5.4.9.

5 Results: dispersive wave tailoring in nano-film enhanced exposed core fibers

The dispersion of the underlying waveguide plays a major role in nonlinear frequency conversion (Chapter 2). Thus, suggesting that by adding nano-films to the fibers (Chapter 4) and enabling anti-crossing through induced resonances (Chapter 3) the output spectrum can be tuned accordingly. This chapter first introduces the experimental setup and the methods to measure the nonlinearly broadened spectra, followed by the mode and polarization properties of ECFs (Section 5.1). The main experimental results are separated in three parts, starting with uniform TiO_2 nano-films with constant thicknesses as a proof of concept for the novel DW tuning mechanism (Section 5.2). The resulting spectra can be improved and optimized concerning their uniform spectral power density and bandwidth with Ta_2O_5 nano-films with gradually increasing thicknesses and thus longitudinally variable parameters (Section 5.3). This is followed by the results of periodically structured Ta_2O_5 nano-films, introducing additional multi-color QPM-DWs to the spectrum (Section 5.4). Last, Section 5.5 combines the individual features of the previous sections to cover more complex nano-film geometries in simulations.

5.1 Experimental methods & properties

5.1.1 Experimental nonlinear transmission setup

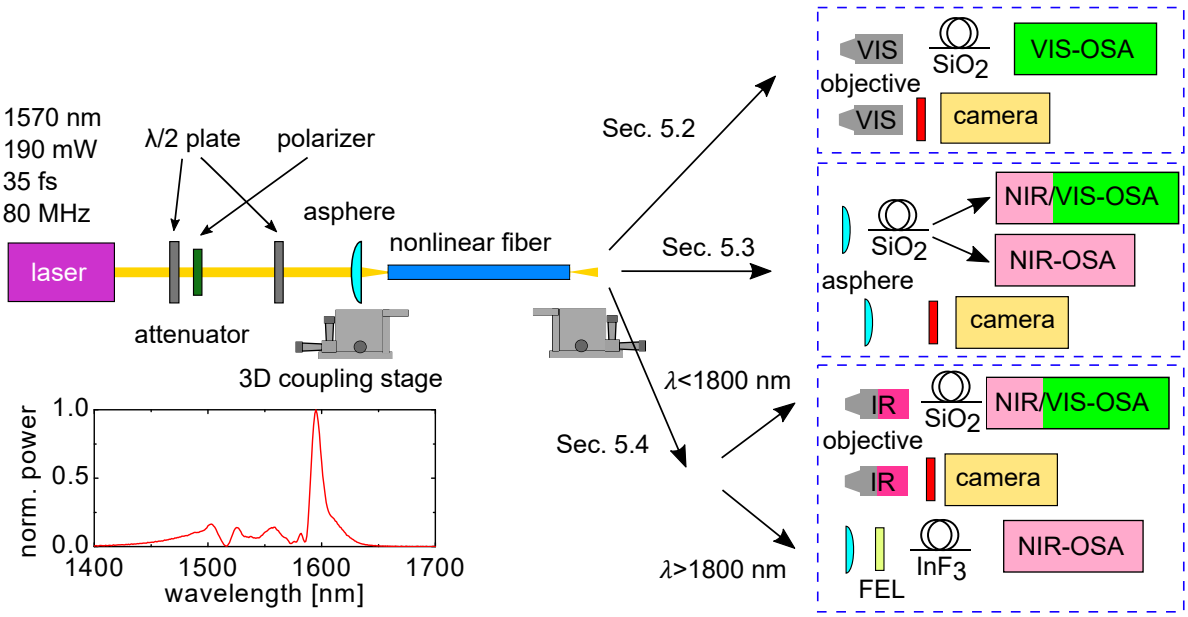

Figure 5.1: Experimental setup, consisting of an identical in-coupling part for all the following experiments, but different out-coupling and detection components as explained in the main text and indicated by the corresponding section numbers. The graph shows the laser spectrum, having an intensity weighted central pump wavelength of λ_p =1570 nm.

The experimental setup is similar for all fiber samples and includes the same laser source (FFpro IRS II, Toptica Photonics). The pump light consists of 20 fs long pulses ($1/e^2$ half width, $\sim$ 35 fs full width half maximum (FWHM)) with a repetition rate of 80 MHz and a weighted central wavelength of $\lambda_p = 1570$ nm. It is controlled in intensity by an attenuator consisting of a half wave plate and a polarizer, allowing for a maximum average power of $\sim$ 190 mW (Fig. 5.1). After passing through a second half wave plate for polarization control the pulses are launched into the fiber with an asphere (C230-TMD-C, focal length f = 4.51 mm, Thorlabs Inc.) mounted on a 3D high-precision fiber coupling stage (Martock MDE510, Elliot Scientific Ltd.). On the diagnostics side of the fiber, the actual setup depends on the wavelength range of interest.

In general, it has a beam collimating element, optional spectral filters, and a data collecting device with a collection fiber attached for optical spectrum analyzers (OSAs). The details of the experimental setup can be split up according to the corresponding sections. For the simplest case of nano-films with a constant thickness (Section 5.2) with a limited resulting bandwidth the collimating element is a 20× objective designed for visible light. It is exchanged to a C-coated aspheric lens (C230TMD-C) for nano-films with a thickness gradient (Section 5.3) in order to enhance the transmission, especially for the increased spectral range towards the infrared. Finally, for periodically structured nano-films (Section 5.4) with the largest generated bandwidth an 20× IR objective (Mitutoyo GmbH) is used instead, maximizing the transmission and reducing chromatic aberrations at the same time. This objective, however, is only designed for $\lambda < 1800$ nm, worsening the already mediocre transmission of $\sim$ 50% and inducing aberrations outside the certified wavelength range. Accordingly, for longer wavelengths up to $\lambda = 2500$ nm a D-coated aspheric lens is used instead (C028TME-D, Thorlabs Inc.). For this wavelength range also the collection fiber had to be exchanged. It is an InF_3 fiber (MF12L2, Thorlabs Inc.) with a core diameter of 100 µm, which has an extended transmission window towards the IR compared to the low-OH silica core fibers used for all other cases. The fibers used for the smaller wavelengths setups are large core, multi-mode fibers with core diameters of 400 µm (Section 5.2) and 1 mm (FT1000EMT, Thorlabs Inc., Sections 5.3 and 5.4), which are less susceptible to chromatic aberrations compared to fibers with a smaller core size. In order to reduce the total amount of optical elements that contribute to losses and are prone to self-dealigning over time, the usage of any tube lens is avoided, using the collimating element to also focus the light.

Dependent on the wavelength range, different OSAs were utilized. For short wavelengths from the visible up to $\lambda = 1750$ nm model AQ6315A (Ando Corp.) is suitable, marked in the sketch with 'VIS-OSA'. For longer wavelengths from $\lambda = 1200$ nm to $\lambda = 2400$ nm, extendable in an experimental setting to range from $\lambda = 1000$ nm to $\lambda = 2500$ nm, model AQ6375 (Yokogawa Corp., marked 'NIR-OSA') is used. Broad spec-

tra exceeding the wavelength range of a single spectrometer require a method using both devices.

For capturing far field mode images and to verify good coupling an IR camera (IK1513, ABS GmbH Jena) and optional spectral filters replace the spectrometer and collecting fiber.

Because photo diode sensors have a wavelength dependent sensitivity, the total power of the broadened spectrum can only be accurately measured with a thermal power meter (S401C, Thorlabs Inc.). It is inserted directly behind the collimating element, thus, measured values need to be corrected for the lens/objective transmission. For an uncoated fiber the maximum coupling efficiency, i.e. output power divided by incoupling asphere corrected input power, is determined to be $\sim$ 25 %. In contrast to the bare ECF, non-negligible losses inside the fiber are introduced for nano-film functionalized fibers. One purpose of monitoring the output power is to obtain the peak power needed for simulations, calculations of fiber parameters and the nonlinear phase in PM considerations. Since the peak power is needed at the input side of the fiber, the transmitted power needs to be corrected for all losses during propagation, which are individual for each fiber. Moreover, nano-films alter the shape of the mode, changing its overlap integral with the focused incoming laser beam and reducing the coupling efficiency. On top of it, cleaving the ECF is difficult as breaking the thin struts holding the core can be unpredictable. This often results in a step-like profile of the end face at random locations close to the core, also affecting the coupling efficiency (see SEM in Fig. A.4). Therefore, measuring the out-coupled light can only give a rough estimation of the incoupled power, being about 10-25 % of the laser light. Assuming a Gaussian pulse shape in time with a width of 35 fs FWHM, peak powers from $P = 7$ kW up to $P = 17$ kW seem realistic, translating to pulse energies of ≤ 0.6 nJ. The exact peak power is determined by considering it as a variable when matching simulated spectra to experimental results.

5.1.2 Spectrum gathering methods

Capturing broad spectra is necessary to comprehend and verify the underlying physics of novel nonlinear broadening concepts. However, chromatic aberrations at the out-coupling of the nonlinear fiber and the in-coupling to the collection fiber hinder accurately measuring the spectral shape that is generated inside the fiber. On top of it, spectrally varying losses of the nonlinear fiber itself, of the optical components such as the collimating element and the collection fiber, water vapor absorption in air, and the spectral sensitivity of the spectrometers induce errors to the measurement. Therefore, carefully choosing all components in the setup as explained in the last chapter is essential. To further counter the existing aberrations the following measuring method is chosen.

Chromatic aberration for a specific wavelength and its near vicinity can be minimized by optimizing the coupling conditions from the output of the nonlinear fiber to the col-

lection fiber of the OSAs concerning maximum signal for that wavelength. Because other wavelengths spectrally further away exhibit aberrations, the spectrum needs to be optimized again for a set of other wavelengths. Finally, all the spectra can be stitched together, forming a more accurate representation of the spectral output. The amount of spectra needed, i.e. the density of optimized wavelengths depends on the aberrations of all optics used and is higher for aspheres in comparison to objectives with built-in chromatic correction. For instance, the spectrum measured with an aspheric lens for long wavelengths (Fig. 5.28b) is optimized for every peak, i.e. at $\lambda = 1800$, 1900, 2050, 2260, and 2420 nm, whereas on the short-wavelength side measured with the IR objective two measurements optimized for $\lambda = 1195$ and $\lambda = 1590$ nm are enough to sufficiently represent the real spectrum up to $\lambda = 1800$ nm.

The method of combining different spectra can be schematically seen in Fig. 5.2 in the form of the purple curve, effectively optimized for short wavelengths ($\lambda = 1125$ nm) and used until $\lambda = 1405$ nm (pink shaded area), and the green curve, optimized for $\lambda = 1800$ nm and used for $\lambda > 1405$ nm (yellow shaded area). In this example the two optimized wavelengths are far apart from each other, leaving a central region near $\lambda = 1405$ nm where the stitched spectrum is probably underestimated in power compared to the real generated spectrum.

For spectra extending to spectral ranges outside the measuring range of one spectrometer, a combination of measurements with the two spectrometers are stitched together with one spectrum measured on both devices without any change of the coupling condition to correct for their power offset.

Unfortunately, the NIR-OSA does not have a protection for second order grating effects, resulting in a false signal at twice the wavelength. It requires a long pass filter with the edge at $\lambda = 1650$ nm (FEL, Edmund Optics) to unambiguously measure spectra at long wavelengths where light of half of the wavelength is also present in the broadened

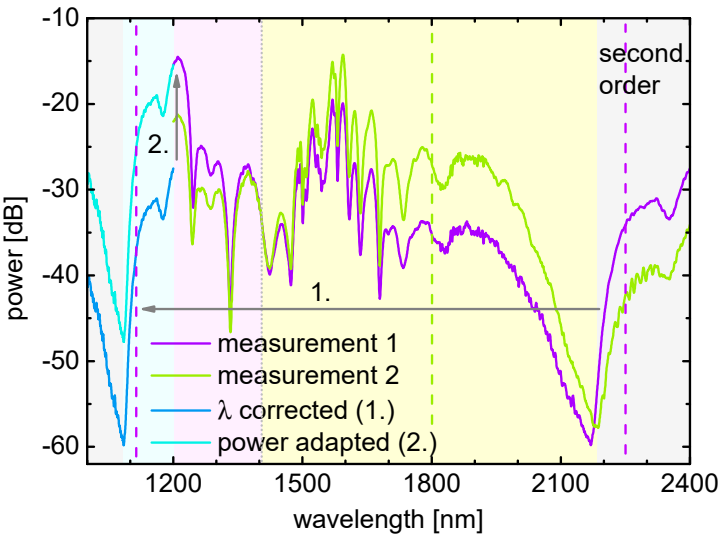

Figure 5.2: Exemplary spectra measured with the NIR-OSA to visualize data processing. Original measurements optimized (vertical dashed lines) at $\lambda = 1800$ nm (green) and $\lambda = 2250$ nm (effectively $\lambda = 1125$ nm, purple). The second order part of the purple curve is corrected for the wavelength (1.) and then adapted in power (2.). The total spectrum is stitched together consisting of the maximum value of all curves, individual sections are marked with a color-matched background. All data in the gray regions is dismissed.

spectrum. However, this can also be exploited for spectra that are narrower than one octave to artificially extend the short-wavelength edge. By reconstructing data based on the second order peaks of the monochromator grating of the spectrometer, information about light outside of the specified device wavelength range can be obtained. This technique is applied for measurements where a time-expensive switching of spectrometers could compromise the comparability of data due to laser power or coupling variations that occur over time, e.g. for power slope studies in Section 5.3.4 and for Section 5.3.5. Specifically, the measured wavelength of the second order peaks needs to be halved (step 1, dark blue curve in Fig. 5.2) and the power adapted to correct for the grating efficiency of the second order (step 2, light blue curve), smoothly connecting it to the remaining spectrum. Measurements using the VIS-OSA for the short wavelength range confirm the validity of this method, at least for wavelength close to the official wavelength range of the NIR-OSA. Finally, the spectrum needs to be cropped accordingly, cutting away the second order light at long wavelengths and the falsely corrected first order tail at short wavelengths (gray background). The ultimate spectrum consists of the maximum of all curves within the interval 1100 nm $< \lambda <$ 2190 nm, with the validity of the individual curves marked with color-matching background.

For the experimental spectra of Section 5.2 the color correcting measurement method is not carried out. Because the spectra are only optimized for the single DW, the remaining spectrum exhibits an error of about -10 dB/500 nm.

5.1.3 Mode properties of exposed core fibers

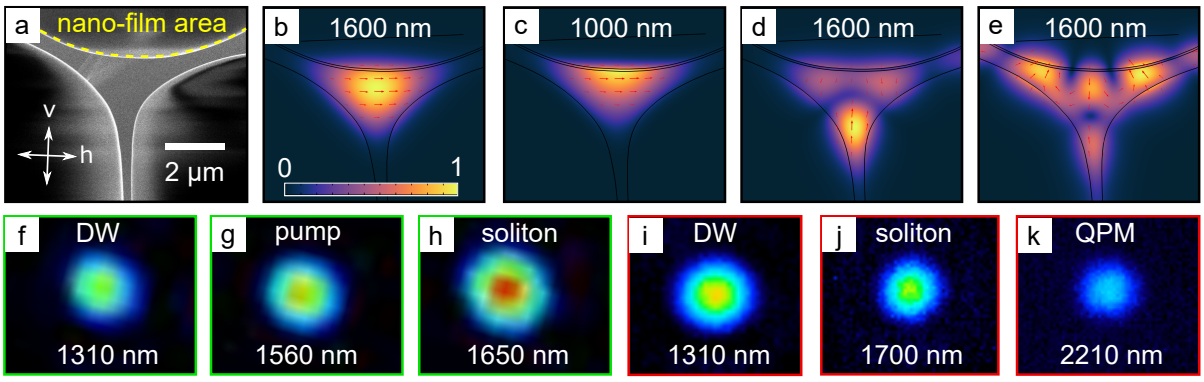

Figure 5.3: (a) SEM of the ECF core section, defining vertical (v) and horizontal (h) polarization. (b+c) Simulated fundamental mode at $\lambda = 1600$ nm and $\lambda = 1000$ nm, respectively, with a Ta_2O_5 nano-film with a thickness of $t = 70$ nm. Red arrows indicate the orientation of the electric field. (d+e) Simulated higher-order modes. (f–h) Experimental modes with a constant TiO_2 nano-film with a thickness of 52.5 nm at different wavelengths. (i–k) Experimental modes with a Ta_2O_5 nano-film with an alternating nano-film thickness of $t = 85.5$ nm and $t = 0$ nm at a period length of $\Lambda = 1.4$ mm at different wavelengths. All experimental modes and the simulated fundamental modes have horizontal polarization.

The V-number of a silica rod in air with the size of the inscribed circle diameter of the ECF (Fig. 4.1) is $V = 7.5$ for the pump wavelength (Eq. 2.1), implying that the number of modes guided is around 28. Similarly, the even larger triangular core of the ECF is supposed to be highly multi-mode. Some simulated mode profiles are presented in Fig. 5.3b–e.

In the experiments, the mode images are captured with an IR camera including spectral filters to select different wavelengths. These filters include a bandpass FB 1310-12 (Thorlabs Inc.), a bandpass FB1560-12 (Thorlabs Inc.) a combination of a long pass filter 1650 nm (Edmund Optics) with a metal interference filter IF 1700 nm (Carl Zeiss Jena GmbH), and a bandpass filter BP 2211-82 (Laser Components GmbH). Although the simulated fundamental mode adapts the triangular shape of the core, its center is still almost circular. Furthermore, the camera has a low resolution as its pixels have an edge length of 30 µm. Therefore, the round images captured experimentally for ECFs with TiO_2 (Fig. 5.3f–h) and structured Ta_2O_5 nano-films (Fig. 5.3i–k) confirm fundamental mode operation in all spectral regions. On top of it, the asymmetrical shape of the core leads to a high birefringence of the fundamental mode. With the presence of the nano-film only two base linear-like polarization states are possible: Parallel and vertical to the nano-film interface. Mode imaging experiments with rotating polarizers show highly polarized output modes aligned to the core geometry.

A potential fundamental mode with v-polarization also transforms into a mode confined to the nano-film for shorter wavelengths, similar to the transformation of the h-polarized mode discussed in detail in Section 3.2.1. Because of boundary conditions at the interfaces, h-polarization is preferred in nano-film modes. Thus, for the v-polarized fundamental mode the involved nano-film mode is of higher-order and has two intensity maxima (Fig. 5.4a–c). As the higher-order nano-film mode has a shorter cut-off wavelength, the resulting ZDW of the hybrid v-polarized fundamental fiber mode is more than 200 nm shorter compared to the h-polarized case for all TiO_2 nano-film thicknesses of interest (Fig. 5.4d). On the one hand,

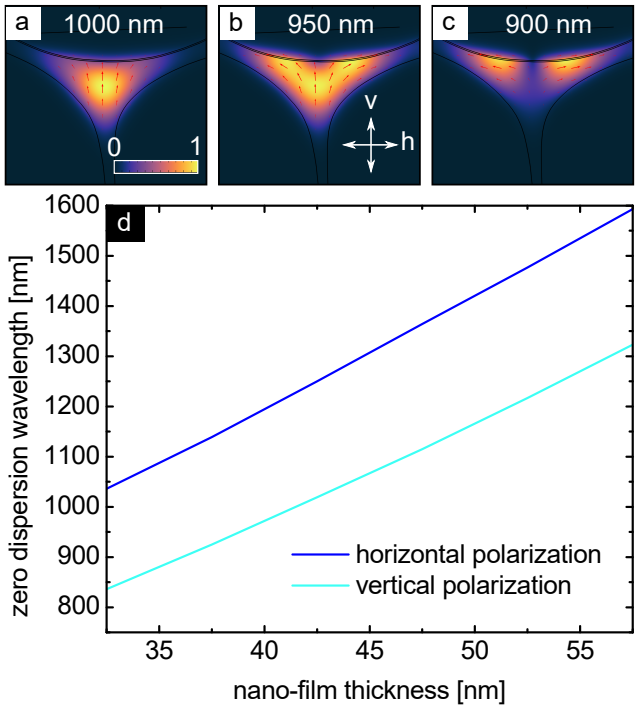

Figure 5.4: (a–c) Simulated absolute electric field distribution of the vertically polarized mode in the vicinity of its anti-crossing. The thickness of the Ta_2O_5 nano-film is $t = 70$ nm. (d) Comparison of the ZDW of the fundamental modes with different polarization.

material losses are smaller for the v-polarized case as the fraction of electric field inside the nano-film is considerably lower (0.2 % compared to 1.8 % in the horizontal case for $t_{TiO_2} = 45$ nm at $\lambda = 1600$ nm, simulated), allowing for a threefold increased transmitted power through the fiber measured in experiments. On the other hand, nonlinear frequency conversion cannot be observed as it requires thicker nano-films to achieve a similar shift in the ZDW. More importantly, the transformation to another polarization direction decreases the mode overlap integral of different spectral components, compromising efficient energy transfer through nonlinear frequency conversion. Thus, in the following, only the h-polarized fundamental mode with the electric field parallel to the nano-film interface is considered.

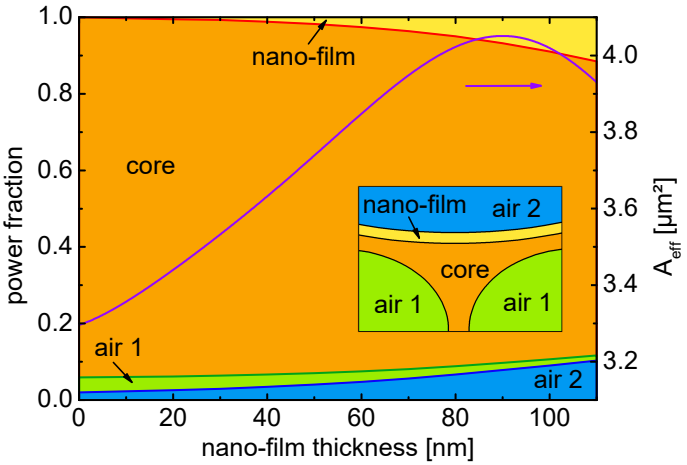

Figure 5.5: Simulated distribution of the fraction of power of the horizontally polarized mode at $\lambda = 1600$ nm dependent on the Ta_2O_5 nano-film thickness. All sections of the fiber are defined and color-matched in the inset. The purple curve indicates the effective mode area A_{eff} with its axis on the right.

Dependent on the nano-film thickness, the power of the fundamental mode is distributed differently in several geometrical regions of the ECF (Fig. 5.5). Albeit mainly confined to the silica core at $\lambda = 1600$ nm, the fraction in other regions raises with increasing thickness. Specifically, the fraction inside the nano-film can grow above 10 % for $t_{Ta_2O_5} > 105$ nm. This enlarged light-matter interaction makes this fiber attractive for studying materials with a two level electronic configuration, involved in the phenomen of self-induced transparency[234]. Moreover, the light in the air above the nano-film in comparison to the evanescent light in all three air regions increases from a third without nano-film to 88 % at $t = 110$ nm (absolutely increasing by a factor of 5). This is highly relevant for applications in sensing[197,198] and photochemistry[235], making the fiber potentially interesting for projects outside of the main scope of this work.

The effective area of the mode (Eq. 2.26, Fig. 5.5, right axis) first increases because the nano-film enhances the evanescent field fraction, but decreases again for $t > 90$ nm owing to the light confinement inside the film.

5.2 Uniform TiO_2 nano-films

As an experimental proof of concept for dispersion modification using anti-crossing in nano-films, the concept described in Chapter 3 is applied to ECFs with a constant nano-

film thickness. In order to examine the tunability of the spectrum by varying the nano-film thickness, precise and uniform films are desirable, directing the choice of deposition technique towards ALD (Section 4.2). This minimizes the peak broadening and the creation of secondary peaks by avoiding fabrication induced dispersion variations along the fiber. As a material, TiO_2 is utilized because of its high RI, great transparency, and availability of infrastructure as well as know-how. On top of it, TiO_2 is a proven functioning optical material that has been successfully used for nonlinear waveguides[236–238] including octave-spanning SCG[239].

5.2.1 Experimental DW tuning via nano-film thickness

The fiber samples with different TiO_2 nano-film thicknesses are produced by simultaneous ALD deposition. Multiple fibers are placed on a holder and are inserted into the deposition chamber. After a joint deposition time creating a base thickness using 682 ALD cycles, one sample was removed from the deposition chamber every following 114 cycles. The measured thickness values by ellipsometry (Section 4.3.1) include uncertainties that are supposedly larger than the variation of the actual nano-film growth rate using the precise ALD technique. Thus, all measured values are averaged to fit on an equidistant grid, leading to sample thicknesses of $t = 32.5$ nm to $t = 52.5$ nm in steps of $\Delta t = 5.0$ nm. These samples exhibit anti-crossing of modes, resulting in a modified dispersion as discussed in Section 3.2 (Fig. 3.4).

For thin nano-films with $t < 42.5$ nm, the ZDW is spectrally far away from the pump wavelength. Hence, no significant spectral broadening can be observed in experiments, identical to uncoated fiber samples. Concerning the sample with $t = 42.5$ nm a soliton is formed close to the pump wavelength, but it cannot be distinguished as a separate peak in the spectrum (Fig. 5.6a). Its existence, at least for larger pump powers, is proven by the appearance of the DW at 1050 nm. Here, the still large spectral distance of the ZDW

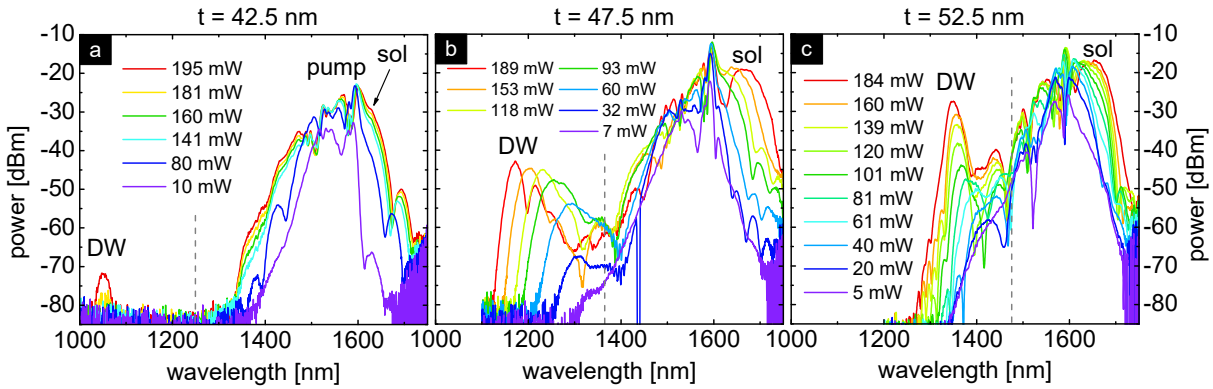

Figure 5.6: Experimental spectra at different average input powers for ECFs with a TiO_2 nano-film with a thickness of 42.5 nm (a), 47.5 nm (b), and 52.5 nm (c). The ZDWs are indicated by gray dashed lines.

and λ_p imposes a large β_2 value at λ_p, leading to a high β_2 to β_3 ratio that determines a low conversion efficiency to the DW (Eq. 2.21). Therefore, the DW is a small peak and appears only at the highest pump powers.

As the dispersion increases and the ZDW red-shifts with thicker nano-films, also the DW moves towards longer wavelengths. For $t = 47.5$ nm and $t = 52.5$ nm (Fig. 5.6b+c), the DW at the highest input power of $P \approx 190$ mW can be found at 1171 nm and 1348 nm, respectively. According to the theory, the conversion efficiency to the DW increases for thicker films as long as the fiber is AD. For ECFs with thicker nano-films of $t > 42.5$ nm, the soliton can be clearly distinguished as an individual peak which red-shifts with increasing input power. Consequently, in accordance with the phase-matching equation (Eq. 2.20), also the DW shifts away from the ZDW, i.e. towards shorter wavelengths. Linearly fitting all three data points of the DW wavelengths at the highest input power, an experimental nano-film thickness driven DW tuning rate of 29.8 nm/nm is obtained. This confirms the concept of precise DW tuning after fiber drawing, spanning a wavelength interval of 300 nm.

5.2.2 Simulations

Solving the GNLSE as described in Section 2.3.9 for ECFs with a length of 5 cm and pulse parameters imitating experimental conditions (peak power: 9 kW, transform limited 20 fs sech^2 pulses at the central wavelength of 1570 nm) leads to the spectra presented in Fig. 5.7a. As observed in the experiments, having a too thin nano-film will not induce any notable spectral changes. Starting from $t \approx 40$ nm, a soliton is formed which red-shifts and generates a DW. Here, the DW can be tuned in wavelength at a rate of 30 nm/nm (magenta dashed line). The soliton number increases as the ZDW shifts closer to λ_p, forming a singularity when they coincide (Fig. 5.7b). Although technically no soliton can be created when the pump is in the ND domain, for ZDWs close to λ_p a part of the flank of the pump spectrum still remains in the AD domain. Moreover, spectral broadening in the ND domain can transfer energy across the ZDW to the AD section, which then forms a soliton and a DW as reported by Christensen et. al[240]. Therefore, these spectral features can be seen until $t = 60$ nm although the pump enters the ND domain at $t = 56$ nm. For even thicker nano-films the fiber is all normal dispersive with only minor broadening by SPM[241] and is not suitable for the nonlinear broadening mechanisms intended in this work. In the ND domain the soliton number can still be calculated numerically to describe nonlinear parameters of the fiber without representing an actual soliton (dashed line in Fig. 5.7b). Apart from near this singularity, the soliton number for experimentally realized nano-film thicknesses stays below 2 and fission to multiple fundamental solitons can neither be observed in experiments nor be predicted by simulations.

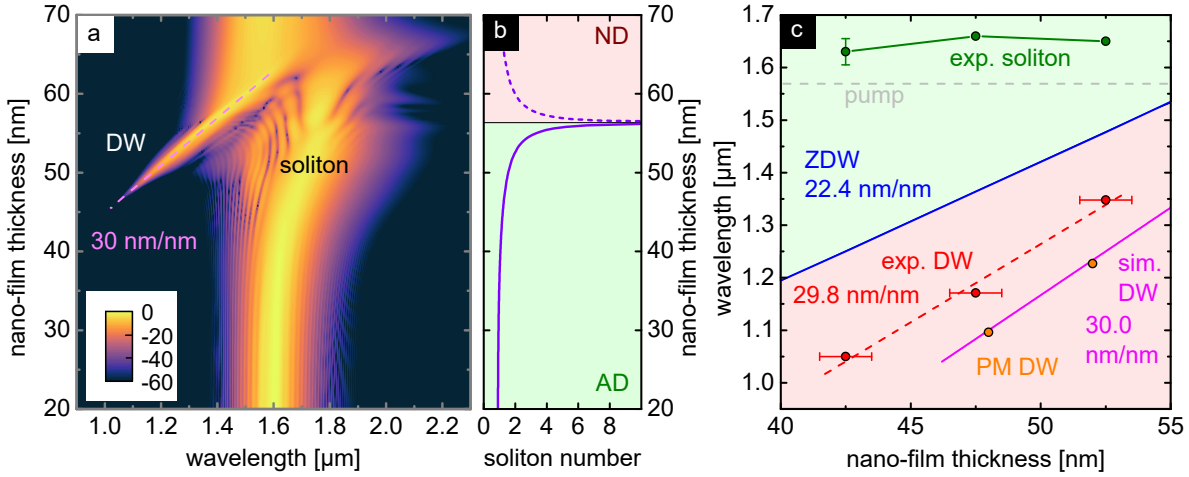

Figure 5.7: (a) Simulated output spectrum in dB of a 5 cm long ECF with varying constant TiO_2 nano-film thicknesses, excited with $T_0 = 35$ fs long pulses, a peak power of 9 kW, and $\lambda_p = 1570$ nm[1]. A dashed line marks the DW. (b) Soliton number of (a) in the normal (ND, red area) and anomalous domain (AD, green area)[1]. The term "soliton" only applies to the anomalous domain while the soliton number can technically be also calculated for the ND domain to reflect the nonlinear parameter in the nonlinear Schrödinger equation. (c) Evolution of the main experimental and simulated spectral features dependent on the nano-film thickness, including the simulated (sim., magenta) DW of (a) with a cut-off due to the vanishing conversion efficiency, and the calculated DW (orange) from phase-matching considerations.

Compared to the experimental position of the DW, the simulated ones via nonlinear pulse propagation are located at shorter wavelengths (Fig. 5.7c). Alternatively and especially when taking into account the cut-off wavelength of the DW, the discrepancy can be interpreted as an offset of 4 nm (or < 10 %) concerning the nano-film thickness. The dominant source of errors should be in measuring the the nano-film by ellipsometry. Not only is the nano-film thickness uncertain up to $\Delta t = \pm$ 1 nm (included as error bars in the plot), but also the measured dispersion $\Delta n = 0.05$ influences the wavelength of the simulated DW. A simulation with a constant RI of $n_{TiO_2} = 2.3$ and neglecting dispersion, which is within the error interval of the dispersion measurements (Fig. 4.7), shows a variation in the DW wavelengths that is equivalent to a thickness difference of 1.5 nm. Another source of errors is the geometry of the fiber used for the simulations as the SEM (Fig. 4.1) has an error of its scale bar of 5 %, contributing to effectively 0.4 nm thickness deviation. Furthermore, the thickness of the nano-film in simulations is implemented as a constant offset of the core surface in v-direction (as defined in Fig. 5.4b) instead of normal to the curved surface, i.e. conformal. For nano-films created by sputtering the implementation method is suiting, however, for ALD it is erroneous, estimated causing another effective 0.5 nm of thickness deviation. On top of it, optical losses are not included in simulations, the shape and chirp of the input spectrum is not taken from experiments, and the assumed

[1]This simulation was performed in collaboration with Kay Schaarschmidt.

peak power of 9 kW might not perfectly represent the in-fiber power for all experimental samples. Despite these small uncertainties, the qualitative behavior and in particular the tuning slope of the DW can be well predicted by simulations.

Another method to calculate and predict the wavelength of the DW is to use the phase-matching condition (Eq. 2.20, Fig. 5.8). At the position along the fiber corresponding to the fission length, the soliton wavelengths of $\lambda_{\mathrm{sol}} = 1610$ nm and $\lambda_{\mathrm{sol}} = 1630$ nm are assumed for the dispersion of the nano-film thickness of $t = 48$ nm and $t = 52$ nm, respectively. Because the PM considerations are based on the same dispersion with the

identical error sources, they can only confirm the result of the nonlinear propagation simulations and not the experiments.

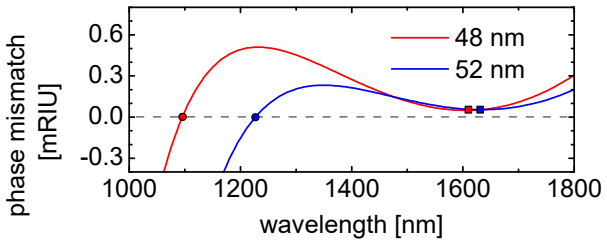

Figure 5.8: Phase mismatch curves of the DW for ECFs with a TiO_2 nano-film with a thickness of $t = 48$ nm and $t = 52$ nm according to Eq. 2.20 with the parameters $P_0 = 9$ kW, $\gamma_{48\,\mathrm{nm}} = 0.0428\ W^{-1}m^{-1}$, and $\gamma_{52\,\mathrm{nm}} = 0.0463\ \mathrm{W^{-1}m^{-1}}$. Phase matching is fulfilled for wavelengths indicated by a circle and the soliton wavelengths are marked by squares ($\lambda_{\mathrm{sol},48\,\mathrm{nm}} = 1610$ nm, $\lambda_{\mathrm{sol},52\,\mathrm{nm}} = 1630$ nm).

All simulations in this section do not include optical losses. However, the presence of loss and its association with the nano-film is obvious as the measured transmission reduces for thicker nano-films (Table 5.1). Yet, the small amount of samples in conjunction with individual contamination and scattering centers as well as the contribution of different coupling efficiencies do not allow for statistically significant conclusions. Cutting away a scattering center increased the transmission of the ECF functionalized with a $t = 42.5$ nm thick nano-film tenfold to then be in line with the data of the other samples. Still, all presented data for this fiber are taken using the fiber before this cut-back.

Successful DW shifting via TiO_2 nano-film thickness tuning can be confirmed, but the resulting spectrum is limited in bandwidth by the relatively weak laser and thus the small soliton number. In order to investigate the potential of this method, simulations with parameters corresponding to a stronger laser are performed, while keeping the identical fiber parameters and a similar fiber length of 60 mm (Fig. 5.9a). Taking the laser parameters

Table 5.1: Key linear and nonlinear properties for the TiO_2 coated ECFs. The values in brackets correspond to after cleaving off a scattering center, although all the presented spectra are measured before the cleave.

t [mm]	γ at λ_p $[W^{-1}m^{-1}]$	transversality	transmittance [%]	N_{sol}	fiber length [mm]	L_{D} [mm]	L_{NL} [mm]	ZDW [nm]	DW [nm]
0	0.036	0.96	18.6	0.9	68	2.0	2.4	771	-
42.5	0.039	0.97	0.7 (7.4)	1.09	68 (51)	2.6	2.2	1250	1050
47.5	0.042	0.97	3.7	1.28	37	3.4	2.1	1364	1171
52.5	0.046	0.97	1.9	1.73	52	5.6	1.9	1477	1348

of the laser SmartLight 50 by Raydiance Inc. offers the opportunity to increase the pulse energy by elongating the pulse duration to 800 fs (FWHM) at the same central wavelength of $\lambda_p = 1570$ nm, resulting in a slightly elevated peak power of 10 kW. This increases the dispersive length, i.e. the light-matter interaction length with high peak powers required for nonlinear interactions, and consequently also significantly raises the soliton number (Fig. 5.9b). With this laser, the tuning range of the DW increases to 570 nm, almost twice of what could be achieved experimentally with the Toptica laser, with a tuning rate of 23.3 nm/nm. The reason for the DW creation enabled at shorter wavelengths and thinner nano-films is the higher soliton number, that also leads to soliton formation at longer wavelengths with a stronger dispersion. On top of it, it enhances the Raman red shift after DW creation, extending the spectrum towards the infrared up to $\lambda = 2.5$ µm. Although the spectrum might not be extendable that far towards the infrared in experiments due to increasing losses at longer wavelengths that are neglected here, it still shows the improvement compared to using the Toptica laser. Fission of the higher-order soliton creates multiple fundamental solitons, which partially overlap in their spectra and form a ∼400 nm broad section with a flat spectral power distribution on the long-wavelength side of the pump. As soliton fission is prone to laser shot noise variations, the presented spectra are averaged using 20 individual spectra including random quantum noise, modeled by the one photon per mode model[139].

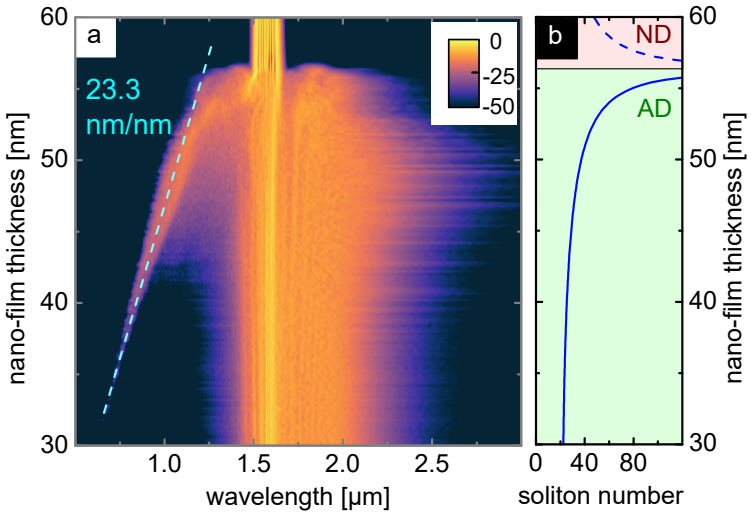

Figure 5.9: (a) Simulated output spectrum of the ECF with varying uniform TiO_2 nano-film thicknesses with laser parameters resembling SmartLight 50 made by Raydiance Inc. (pulse width: 800 fs, peak power: 10 kW, $\lambda = 1570$ nm, fiber length: 60 mm, the color bar shows the spectral power in dB)[1]. (b) Soliton number of (a) in the normal (ND, red area) and anomalous domain (AD, green area)[1]. The term "soliton" only applies to the anomalous domain while the soliton number can technically be also calculated for the ND domain to reflect the nonlinear parameter in the nonlinear Schrödinger equation.

[1]These simulations were performed in collaboration with Kay Schaarschmidt.

5.2.3 Discussion and Conclusion

Depositing TiO_2 nano-films enables tunable nonlinear frequency conversion in ECFs, which without a nano-film would be unsuitable for spectral broadening in the telecommunication regime with our laser. Specifically, nano-films with thicknesses in the range from $t = 42.5$ nm to $t = 52.5$ nm are suitable and cause a single DW that can be tuned within a spectral range of 300 nm at a rate of 30 nm/nm. The qualitative match of experimental results and simulations confirms the modeling and proves the concept of dispersion modulation by anti-crossing of modes induced by the nano-film.

An increasing nano-film thickness implies a higher geometric fraction of material with enhanced nonlinearity (30 times the one of silica) which is additionally enhanced in effect by also shifting the mode profile towards the thin film to enlarge the fraction of energy of the mode inside this nano-film. However, the total change in nonlinearity of the mode is only minor (Table 5.1). Therefore, the increase in conversion efficiency with higher nano-film thicknesses and the overall tunability is dominated by the change of the dispersion, represented by the pronounced variation of the dispersive length compared to the nonlinear length. This also suggests that resonance-induced manipulation of the waveguide dispersion is the major origin of the dispersion tunability rather than effects of material dispersion (compare to Section 2.2). Thus, also other materials should be usable for this effect as long as they have a high RI compared to the core material and are transparent in the near IR.

The presented concept allows for tunable ultrafast light sources with well-defined spectral properties. Beyond nonlinear frequency conversion, examples of applications for flexible nano-film functionalized ECFs include fine-tuning of evanescent fields in bioanalytics[242] or tailoring modal properties to study sophisticated optical phenomena such as PT phase transitions[243].

Despite the successful nonlinear broadening, the spectrum exhibits a distinct spectral gap between λ_{DW} and the pump wavelength. Furthermore, the bandwidth is limited by the soliton being spectrally close to the pump. Although the bandwidth could be potentially increased by switching to a stronger laser as confirmed by simulations, the spectral gap on the short-wavelength side will still be present. Moreover, the uniform section on the long-wavelength side of the spectrum is achieved by inducing high order soliton fission as spectral broadening mechanism and switching to longer pulses approaching the domain of MI. As they inherently are associated with a loss of coherence, being crucial for many applications, other dispersion designs are preferable to improve the uniformity of spectra from ECFs.

5.3 Ta_2O_5 nano-films with a thickness gradient

Constant thickness nano-films on ECFs are proven to be able to modify the nonlinearly broadened spectrum, while exhibiting disadvantageous features as discussed in Chapter 5.2. One promising approach to fill the spectral gap between the pump and the single DW is to create multiple DWs at different wavelengths. Instead of increasing the input power to create DWs from multiple solitons generated during soliton fission, generating multiple DWs from a single soliton is possible via longitudinal dispersion control in fibers.

On the one hand, longitudinal dispersion variation in order to shape the output spectrum can be done discretely by splicing individually constant fiber sections[244–246]. For example, cascading fibers composed of different materials is the key to enable supercontinua in the mid-IR spanning over an interval of 8000 nm[247]. On the other hand, continuously varying the dispersion can be realized by smoothly tapering waveguides, tracing back to several km long slowly dispersion decreasing or increasing fibres in 1997[248]. Ever since, numerous works present the advantages concerning flatness and bandwidth of longitudinally varying dispersion for nonlinear frequency conversion in various systems such as tapered planar waveguides[63,249], tapered photonic crystal fibers[250,251], dispersion oscillating fibers[252], tapered multimode fibers[54], and tapered fiber tapers, i.e. bare glass rods in air[253]. In contrast to these static designs, reconfigurable approaches exploit tailorable temperature profiles[74,254] and plasma density gradients along gas filled hollow core fibers[76,122].

In the following experiments, longitudinal dispersion management is achieved by inducing longitudinally varying resonances in ECFs via coating them with nano-films with a gradually increasing thickness. Because of the desired non-uniformity, magnetron sputtering with a tilted deposition is suitable for this application (Section 4.2.2). The material of choice is Ta_2O_5 as its RI is high enough to keep the required layer thickness at an acceptable value to induce anti-crossing of modes (Chapter 3). Moreover, it is transparent in the visible and near-IR until $\lambda = 9$ µm[227] and readily available. Because of these properties, Ta_2O_5 is a known optical material and is, among other applications, used in waveguides for sensing[255] and for SCG[256]. ECFs functionalized with Ta_2O_5 nano-films having a thickness gradient form a dispersion landscape as presented in Fig. 3.5.

5.3.1 Properties of nano-films with longitudinally increasing thickness

There are two main properties that can fully describe a particular nano-film gradient when considering a linear dependence of the thickness on the position along the fiber for a fixed fiber length. The first one is the starting thickness t_s at the beginning of the fiber and the second one is the steepness of the gradient named gradient strength gs. The effect of linear nano-film gradients with increasing thickness along the fiber can be best understood when analyzing the influence of the two gradient parameters on the dispersion individually. As

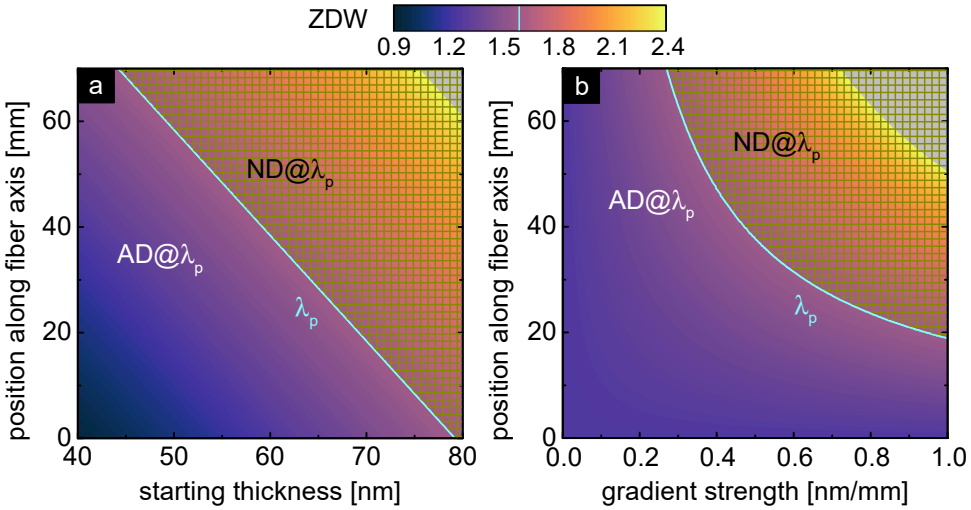

Figure 5.10: Tuning potential of the ZDW landscape along the fiber in ECFs functionalized with a Ta_2O_5 nano-film having a thickness gradient. (a) Influence of the starting thicknesses on the ZDW (in µm) for a constant gradient strength of 0.5 nm/mm and (b) of the gradient strengths considering a constant starting thickness of $t_s = 60$ nm. The cyan line divides the plots into anomalous (AD) and normal dispersive domains (ND, shaded area) with respect to the pump wavelength of 1570 nm.

the ZDW is a strong indicator of the dispersion and the behavior of a nonlinear system, this representative value is considered in the following simulation. For a fixed fiber length of 70 mm and a fixed gradient strength of $gs = 0.5$ nm/mm, the ZDW of a Ta_2O_5-coated ECF linearly depends on the starting thickness (Fig. 5.10a). For starting thicknesses $t_s < 79$ nm the used pump pulse at $\lambda_p = 1570$ nm travelling through the fiber starts in the AD domain. Considering a fission length of 6-10 mm and DW formation at that position along the fiber, the starting thickness required to stay in the AD domain at the DW creation position needs to be further decreased to $t_s < 74$ nm. For positions further along the fiber the GVD increases until the ZDW crosses the pump wavelength (cyan line) and the fiber becomes ND until the end of the fiber. Usually, this would make the remaining fiber useless for further nonlinear frequency conversion at this power level because the spectrum would not change notably in the ND domain. However, before the fiber position where the ZDW crosses λ_p, the nonlinear interaction might have led to soliton formation and its red-shift owing to the Raman-effect. In this case, if $\lambda_p < \lambda_{\mathrm{ZD}} < \lambda_{\mathrm{sol}}$, the soliton can still be in the AD domain and continue to contribute to nonlinear broadening, especially DW generation. This extends the useful fiber section beyond the cyan line in Fig. 5.10.

When considering a constant starting thickness of $t_s = 60$ nm and varying the gradient strength, the overall effect on the ZDW becomes nonlinear (Fig. 5.10b). In both simulations there is no ZDW at high gs and t_s (gray area), because the fiber becomes completely ND for $t > 110$ nm (compare to Fig. 3.5).

5.3.2 Nonlinear dynamics ECFs with a nano-film thickness gradient

Together, the gradient strength and the starting thickness form the dispersion landscape of functionalized ECFs and lead to unique spectral and temporal pulse evolutions along the fiber length, ultimately shaping the final output spectrum at the end of the fiber. For the special case of a linear nano-film gradient from $t = 62$ nm to $t = 135$ nm within a fiber length of 75 mm, corresponding to $gs = 1.04$ nm/mm, with an input power of 15 kW, the simulated pulse evolution along the fiber solving the GNLSE as described in Section 2.3.9 is presented in Fig. 5.11.

Starting from a transform limited pulse, the first 7 mm of the fiber feature SPM and temporal compression driven symmetric frequency broadening. Near the 7 mm position a soliton is formed on the long-wavelength side close to the pump, transferring energy to a first DW near $\lambda = 1.13$ µm. The spectral position of the DW can be confirmed by calculating the phase matching wavelength (marked with a cross, $\lambda = 1144$ nm) using Eq. 2.20 with the local dispersion at this specific position along the fiber and the soliton wavelength picked from the simulation data and marked with a blue circle ($\lambda_{sol} = 1650$ nm). Without any nano-film gradient this DW would be the only significant spectral feature at wavelengths shorter than the pump as presented for constant TiO_2 nano-films. However, for nano-films with a thickness gradient, around 15 mm from the fiber start a second DW emerges near $\lambda = 1.29$ µm, partly filling the gap between first DW and the pump. The wavelength of this second DW is determined by the changed waveguide dispersion and shifted soliton wavelength, induced by the Raman-effect. As the GVD increases along the fiber this opens up multiple PM opportunities to create DWs from the same constantly

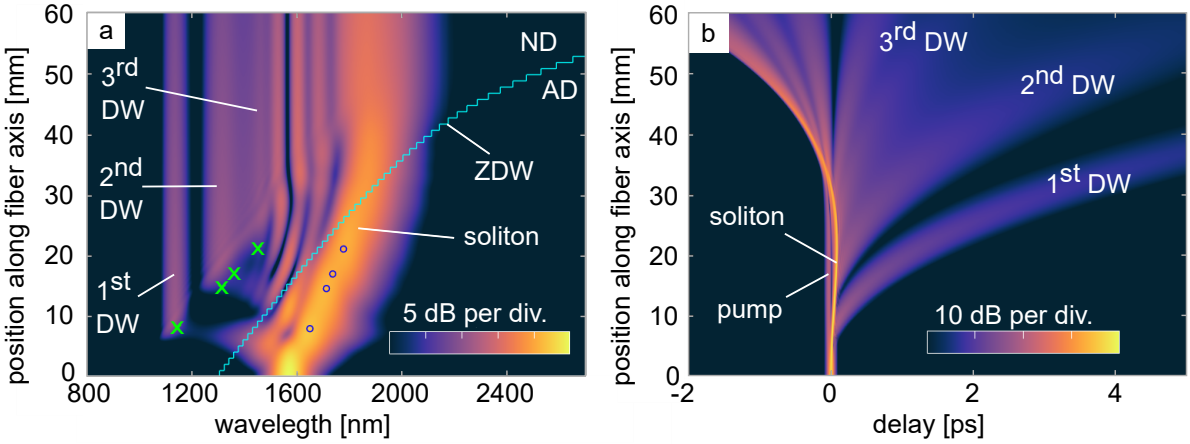

Figure 5.11: Pulse propagation simulation in the spectral (a) and temporal domain (b) of an ECF with a linearly increasing Ta_2O_5 nano-film thickness from $t_s = 62$ nm to $t = 135$ nm within a length of 75 mm with an input peak power of 15 kW. The cyan line is the ZDW, splitting the plot into the AD (below) and ND domain (above). Green crosses mark the phase-matching wavelengths calculated with Eq. 2.20 when using the soliton wavelengths indicated by the blue circles.

red-shifting soliton until the ZDW surpasses the soliton wavelength near the 30 mm mark. This happens because the ZDW shifts faster than the soliton Raman shift in this case[253]. Now being in the ND domain, the soliton disperses and the spectrum barely changes until the end of the fiber.

Interestingly, although the change of the dispersion and the red-shift of the soliton happen continuously, individual discrete DWs at specific positions are created, which can be also distinguished in the time domain as observed by Vukovic et al. in tapered planar waveguides[257]. Milian et al.[253] explain the occurrence of individual DWs, in their case starting from soliton numbers greater than 2, by a periodically stronger soliton recoil, increasing the spectral distance of the soliton to the ZDW. As a consequence, the conversion efficiency to the DW decreases, starting a section of less recoil. In this slower red-shifting soliton section of the fiber, the constantly red-shifting ZDW can close the spectral distance to the soliton. Next, the conversion efficiency increases again, enhancing the recoil and closing the circle of a periodically varying DW strength. However, no clear spectral bandwidth fluctuation of the soliton could be observed in their case and clearly discriminating cause and effect is difficult. Alternatively, the lack of a continuous spectrum can be associated with the suppressed soliton fission and the soliton breathing. With the soliton number $N_{\mathrm{sol}} = 1.7$ being larger than 1 while staying in a single pulse without soliton fission as seen in the time domain (Fig. 5.11b), the higher-order soliton can only be stable in a dynamic way leading to periodically occurring soliton self compression (SSC) in the temporal domain and related spectral broadening[139,258] (soliton breathing). The periodical broadening of the soliton spectrum can be seen in Fig. 5.11a in form of a small indentation between the creation of the first and second DW on the long-wavelength side. On top of it, it is clearly visible on the short-wavelength side in the part of the soliton extending across the ZDW. This leads to a seeding of the DW across the ZDW at λ_{DW} with varying intensity (Section 2.3.5). Thus, the conversion efficiency to the DW is varying for different positions along the fiber.

In the final spectrum there are several peaks between the long-wavelength soliton and the pump wavelength, that could be attributed to multiple solitons after fission as observed by Yin et al.[142] However, only one additional peak is generated in the AD domain below the ZDW in Fig. 5.11a and all others occur in the ND domain. Hence, not all of the additional peaks can be attributed to solitons.

According to the temporal pulse evolution (Fig. 5.11b), the final spectrum is heavily broadened in time and chirped. On the one hand, the spectral features from the DWs over the pump to the soliton are all sorted in time according to their wavelengths. This simplifies the procedure to potentially compress the pulse. On the other hand, a separation of individual spectral peaks could be interesting for pump-probe experiments at different wavelengths, with the temporal delay of the pulses being tunable with the fiber length.

5.3.3 Optimizing nano-film gradient parameters via an FoM

Although the concept of creating flatter spectra is predicted in principle in Fig. 5.11, optimizing the gradient parameters for specific output spectra is necessary for specific applications. The requirements for supercontinuum sources range from a defined total output power over the provided spectral range and shape to a good nonlinear conversion efficiency and pulse to pulse stability. Here, the focus lies on providing the largest bandwidths possible and creating the flattest spectra at the same time while using a limited input power. Simulating the output spectrum of a 75 mm long ECF for the given laser parameters (Toptica) with an input peak power of 15 kW and wavelength independent losses of 50 dB/m gives insights which combinations of multiple feasible gradient parameters might be preferable (Fig. 5.12). For some parameter combinations no soliton can be created as the fiber is not anomalous dispersive. Therefore, the simulations in the top right corner, bordered by a dashed line in Fig. 5.12a, do not include the soliton tracking feature described in Section 2.3.9.

Optimizing the bandwidth for simulations with different gradient parameters, the best case is around $gs = 1$ nm/mm with $t_s = 54$ nm, marked 'A' in Fig. 5.12a. Below the maximum there is a clear edge cutting off the bottom part of the plot. This sudden drop can be connected to the bandwidth definition, being set for the short-wavelength edge as -30 dB compared to the maximum spectral power of the entire spectrum. As the long-wavelength edge is not as sharp as the short-wavelength one, for this edge in simulations the bandwidth definition is set to -10 dB instead. Furthermore, the reduced threshold of the long-wavelength side ensures that the bandwidth is determined by the soliton instead of weaker and experimentally not detectable features near $\lambda = 2400$ nm, occurring in

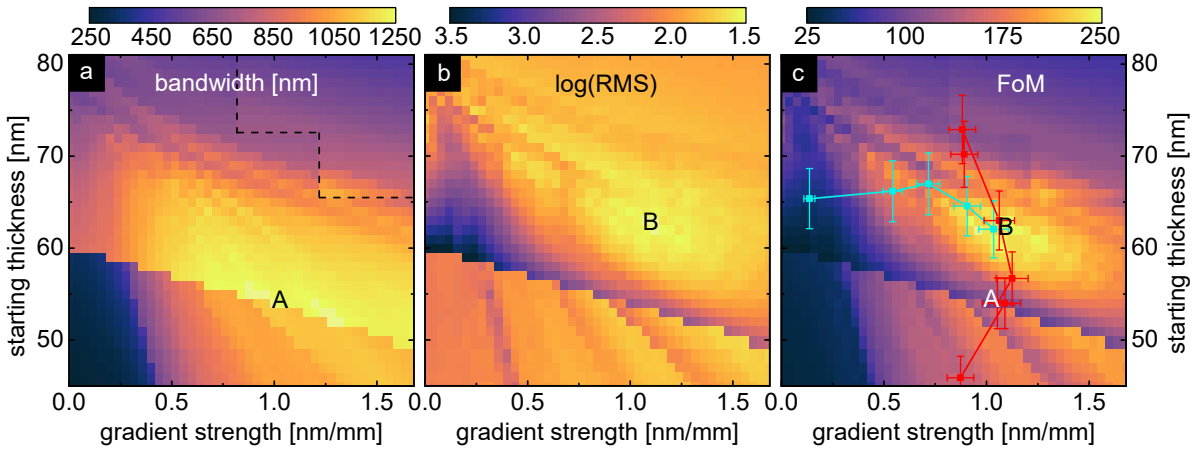

Figure 5.12: Assessment of simulated spectra at an input peak power of 15 kW dependent on different nano-film gradient parameters using their bandwidth (a), their flatness (b), and the combination of both in form of the figure of merit (FoM) in (c). The red and cyan data indicate experimentally used gradients and local maxima are marked with letters. The dashed line in (a) indicates the corner where the soliton is not traceable.

some simulations. However, the bandwidth definition for experiments (presented in the next Section) is set to -30 dB on both sides as losses increase towards the IR, resulting in a steeper edge that more or less coincides with the -10 dB definition for the corresponding simulations where these losses are neglected. With the first DW being a single peak, the bandwidth exhibits a sudden jump in case this peak suddenly fails or succeeds to fulfill the -30 dB threshold.

One method to define the flatness of spectra is to minimize the root mean square (RMS) value of the spectrum within a certain interval, for instance, its own bandwidth. Considering the RMS, the best gradient parameters are near the maximum at $gs = 1.09$ nm/mm and $t_s = 63$ nm, marked 'B' (Fig. 5.12b). The cut previously discussed for the bandwidth also appears in the RMS considerations, but contrarily the bottom side of it gives better values. The RMS recovers to lower values at thinner t_s, when the single, low power peak defining the bandwidth is not taken into account anymore. However, for the most broadband spectra this peak is crucial and gradient parameters above this cut should be considered.

In order to assess the output spectrum both the uniformity (RMS) and the bandwidth need to be taken into account. The simplest function to create a joint figure of merit (FoM) is given by the fraction of the bandwidth and the RMS value.

$$\mathrm{FoM} = \mathrm{bandwidth}_\lambda / \mathrm{RMS}_\nu = (\lambda_{\max} - \lambda_{\min}) \cdot \left(\frac{\int_{\mathrm{bandwidth}} (P(\nu) - \bar{P})^2 d\nu}{\nu_{\max} - \nu_{\min}} \right)^{-\frac{1}{2}}.$$

P stands for the spectral power and the bar above indicates the mean value of it within the bandwidth. The bandwidth is given by an interval in frequency (ν) and wavelength, enclosed by the values with the subscripts min and max. A high FoM number indicates a flat and broad spectrum.

Within the given gradient parameter space, there are two main areas of low FoM that should be avoided (Fig. 5.12c). The first one is located at large t_s values and can be associated with a low bandwidth. As the ZDW for thick layers is longer and closer to the pump, also the first DW is created close to the ZDW, resulting in overall narrow spectra. As all other potential DWs are generated at longer wavelengths than the first DW, this low FoM area based on t_s cannot be overcome by changing the gradient strength.

The second area of low FoM is located at low gs values with mixed causation dependent on the layer thickness. Below $t_s = 60$ nm the bandwidth and its definition is the limitation, whereas for thicker starting thicknesses the lack of secondary DWs without any gradient leads to the known spectral gap. This massively decreases the uniformity and thus the RMS value.

The best gradient parameters for a high FoM seem to lie near the maximum given by the RMS consideration, with additional restrictions given by the bandwidth. The separation

of the maxima A and B suggests a trade-off between uniformity and bandwidth that cannot be maximized at the same time for these laser parameters.

Two sets of experimental samples are fabricated as explained in the next sections in more detail. The first set (Set 1, cyan data in Fig. 5.12c, Section 5.3.4) aims to vary gs (horizontal cut through the parameter space of Fig. 5.12) and the second one (Set 2, red data, Section 5.3.5) principally varies t_s (vertical cut).

5.3.4 Gradient strength study

The different nano-films on the ECFs of Set 1, aiming to explore the influence of gs, are created by depositing one fiber at a time at different substrate angles φ (Fig. 5.13). The deposition time is adapted to roughly get the same starting thickness, i.e. the thickness at the end of the substrate that is further away from the sputtering target (Fig. 4.5b). Being located at an almost fixed position only leaves the cos-like dependence of the incident angle θ, simplifying the deposition time prediction. After measuring the exact thickness profile along the substrate with an ellipsometer (Section 4.3.1), the cleaving point of the fiber determining the starting position of the final sample can be fine tuned to get a constant starting thickness of $t_s \approx 73$ nm for all fibers of this set. With the second end of the sample changing both horizontal and vertical position inside the deposition chamber dependent on the substrate angle, several nano-film thickness gradient shapes are possible. Small angled fibers have a nano-film distribution following a concave function with the nano-film thickness reducing for long fiber lengths. For mid-level angles around $\varphi \approx 30°$, the thickness decreases linearly along the fiber and finally having a convex shape for steep angles. All of these shapes can be confirmed by simulations, modeling the sputtering deposition as described in Section 4.2.2. However, results from that model are only used

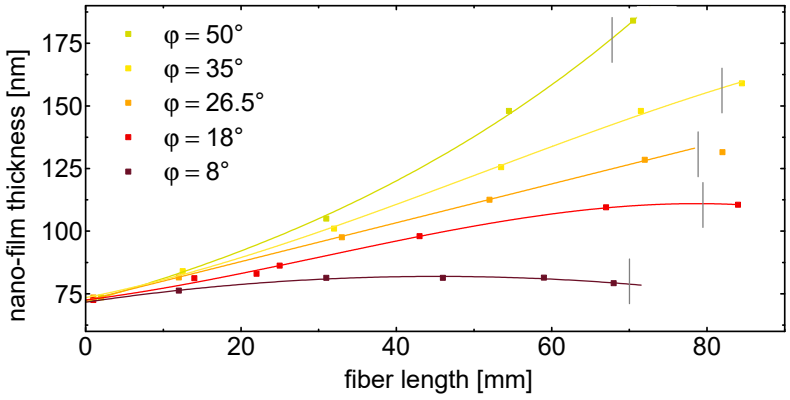

Figure 5.13: Measured nano-film thicknesses (Ellipsometry) along tilted substrates with different angles, having the same starting thickness and different gradient strengths. Solid lines are fits to the data and gray vertical lines mark the cleaved end of the fiber.

later (Fig. 5.16). In Fig. 5.13, the lines modeling the experimentally measured data (square markers) are fitted using polynoms of various orders and exponential functions.

Because most of the nonlinear effects concerning spectral broadening happen in the beginning of the fiber and the nonlinear part of the thickness gradient mostly appears near the fiber end, in the first 50 mm of the fiber the nano-film slope can be approximated by a straight line, i.e. a constant gs. This results in a variation of the averaged gradient strength from $gs = 0.15$ nm/mm for the fiber with $\varphi = 8$ °, up to $gs = 1.2$ nm/mm for the fiber with $\varphi = 50°$. The comparison to the FoM simulations using a linear gradient as in Fig. 5.12c was done based on that simplified gs value.

All in all, Set 1 can be seen as a study of the gradient strength for a fixed starting thickness, that is, a horizontal line in Fig. 5.12c. However, every fiber has its own correction factor f_c for the nano-film thickness inside the fiber (Section 4.2.2), which is kept as a variable to match experimental to simulated spectra. The values found are $f_c = 0.905$, 0.922, 0.935, 0.90, and 0.86 for the fibers with increasing angles φ of

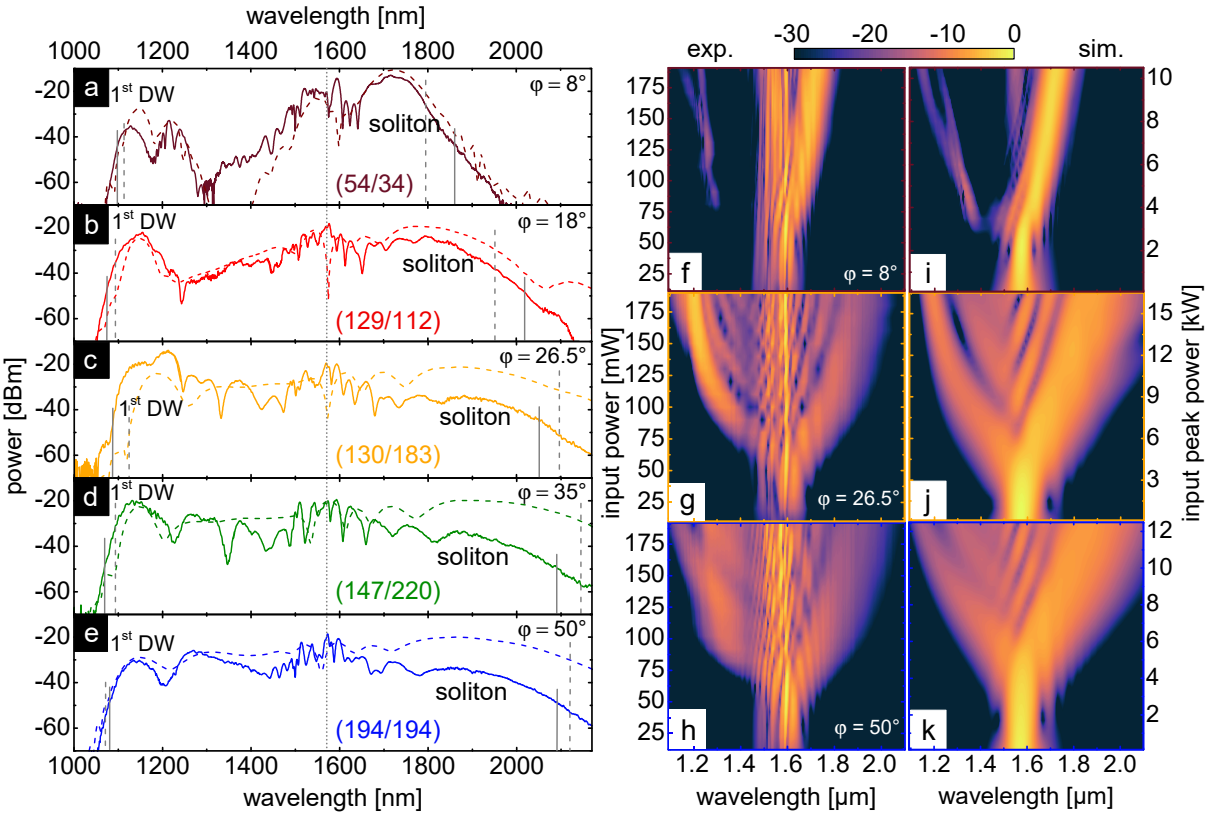

Figure 5.14: (a–e) Experimental (solid lines) and simulated spectra (dashed lines) of the gradients shown in Fig. 5.13 at maximum input power. Gray dashed and solid vertical lines mark the bandwidth of the spectra whereas the dotted line represents the central pump wavelength. The numbers in parentheses show the figure of merit (experimental/simulated). To the right are experimental (f–h) and simulated (i–k) power evolutions of the spectra in (a), (c), and (e), respectively (color-matched frame). The color map shows the spectral power in dB and is normalized to 0 for all plots individually.

Fig. 5.13. Therefore, applying this correction to the nano-film thicknesses on the substrate (Fig. 5.13), the experimental markers in Fig. 5.12c symbolizing the thicknesses on the ECF are not anymore on a straight line having the same t_s.

The experimental result of Set 1 is presented in Fig. 5.14, with the experimental output spectra at maximum average input power of $P \approx 190$ mW displayed with solid lines in the sub-figures a–e. All fibers of this set exhibit a similar starting thickness and consequentially also a similar thickness near the fiber start, about 7 mm into the fiber. Near that position the first DW is generated as confirmed by pulse propagation simulations (Fig. 5.11). Hence, the local dispersion responsible for the first DWs and their wavelengths are comparable for all fibers. Because the first DW marks the short-wavelength edge, the spectral of all samples start near $\lambda \approx 1050$ nm.

The fiber with $\varphi = 8°$ exhibits a dual-peak feature at short wavelengths, which is caused by the unique dispersion along the fiber. Because of the non-uniform deposition using sputtering, especially on smaller 4" facilities, even without angled mounting of the fiber there is a layer thickness variation (Fig. 4.4). This also influences the shape at small fiber tilting angles, leading to a thickness gradient in the beginning of the fiber and a thickness plateau covering the last two thirds of the fiber (Fig. 5.13). The occurrence of the second peak can be best visualized by plotting the power dependent fiber output spectra (Fig. 5.14f). Below 75 mW input power the pump is not strong enough to generate the soliton and the DW. At 75 mW the DW is created at the very end of the fiber. The position of the creation shifts towards the start of the fiber as the power increases. Because of the dispersion plateau, there is no effect of the creation position on the DW, it only blue-shifts because of the longer soliton wavelength with higher input power. At 140 mW pump power and above, the position of the DW creation reaches the remaining thickness gradient at the beginning of the fiber. With the dispersion being different for the first DW compared to the remaining fiber, the second emerging DW has a slightly longer wavelength and creates the second peak. This is confirmed by the pulse propagation simulation at maximum input power and the corresponding PM calculations (Fig. 5.15). Additionally, the experimental spectral power evolution matches corresponding simulations, also showing the splitting of the DW (Fig. 5.14i). As the two DWs are spectrally close together and no

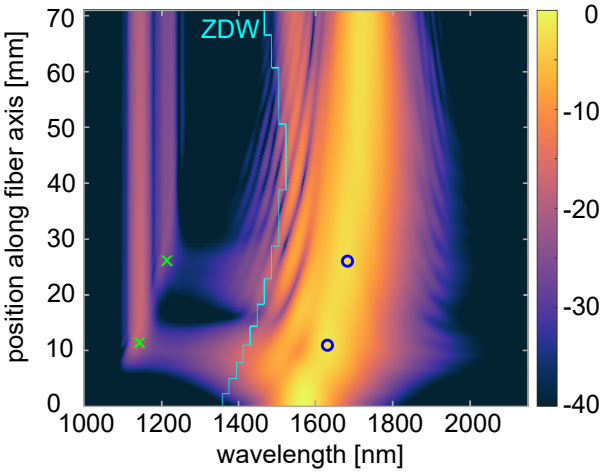

Figure 5.15: Pulse propagation simulation showing the spectral power density in dB along the fiber with $\varphi = 8°$ (Fig. 5.14a+f+i). The cyan line is the ZDW and green crosses mark the phase-matching wavelengths calculated with Eq. 2.20 when using the soliton wavelengths indicated by blue circles.

third DW is generated at the dispersion plateau, there is still a considerable spectral gap to the next longer wavelength feature, i.e. the pump, leading to a low experimental and simulated FoM.

For larger gs the layer thickness increases monotonously and more secondary DWs are created, filling up the spectrum in between the first DW and the pump wavelength. As the gradient strength increases, also the steepness of the dispersion change increases, reducing the fiber section length having the specific dispersion needed to generate the shortest wavelength DW. In combination with stronger secondary DWs, this helps to balance the power of all DWs to create a more uniform spectrum, reducing the RMS part of the FoM.

Concerning the long-wavelength side of the spectra, for the fiber with $\varphi = 8°$ the soliton is close to the pump wavelength, as observed with constant TiO_2 nano-films. For larger gs up to $\varphi = 26.5°$, the soliton shifts towards longer wavelengths, confirmed by simulations (dashed lines in Fig. 5.14a–e). The massive increase of the Raman shift from 80 nm in case of constant TiO_2 to 280 nm for gradually increasing thickness Ta_2O_5 nano-films is caused by the adapting dispersion along the fiber. Moving the ZDW simultaneously with the Raman-shifting soliton towards longer wavelength keeps the absolute value of the local dispersion at the soliton wavelength low and thus modifies the soliton width. This enhances the Raman shift (Eq. 2.17) and increases the bandwidth part of the FoM. For even steeper gradients, the increased red-shift saturates as the very thick nano-film sections just add normal dispersive light propagation near the end of the fiber that does not affect the soliton (Fig. 3.5).

All in all, Set 1 shows an increasing FoM and corresponding improvement of the spectral shape for larger gs within the investigated parameter space as predicted by the preliminary FoM study (Fig. 5.12).

For all fibers of this study the direction of propagation is important. To obtain significant broadening the light should be coupled from the fiber end with smaller layer thickness. Coupling light from the end with thick nano-films often prevents all nonlinear broadening. As the light is coupled into the ND part of the fiber (ignoring fibers with very low angles φ) the pulse experiences quick temporal dispersion and no soliton is formed. In combination with the optical losses along the fiber, when finally reaching the AD section the peak power is reduced such to prevent any nonlinear interactions.

5.3.5 Starting thickness study

In contrast to Set 1, where all fibers are coated individually on single fiber holders, Set 2 uses a joint holder with several fingers at different angles φ (see Fig. 4.5b). One fiber is attached to each finger and all of them are coated simultaneously with the same sputtering time. As before, the measured nano-film thicknesses on the substrates, resulting in various nano-film gradient shapes dependent on φ, are presented in Fig. 5.16. The

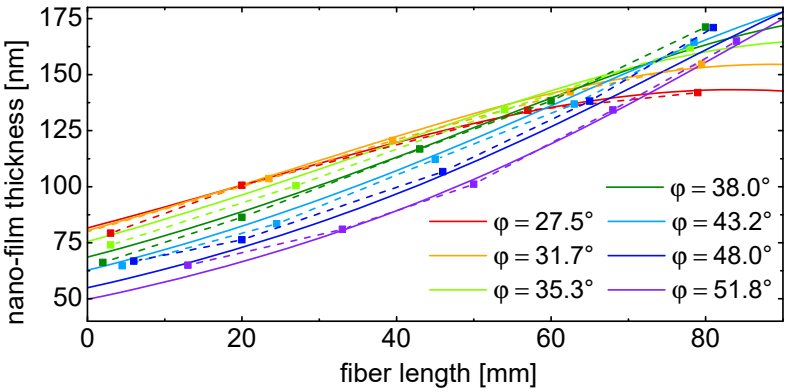

Figure 5.16: Nano-film thickness on the tilted substrate for different angles measured by ellipsometry, having similar gradient strengths in the beginning of the fiber and different starting thicknesses. Solid lines are fits using the sputtering model of Section 4.2.2 and dashed lines are guides-to-the-eye for the experimental data (squares).

dashed lines guide the eye to the the experimental thicknesses, marked with squares. This time, the solid lines are calculations using the sputtering model of Section 4.2.2. The only parameters adapted to match the model to the measurements are the positioning of the entire fiber holder in x and y relative to the center of the sputtering target and a prefactor accounting for a slightly lower sputtering rate compared to the tests in Fig. 4.4.

The model can fully explain all the different shapes of the layer thickness gradients along the ECFs from concave over linear to convex. Interestingly, despite the drastically different angles φ involved, all samples exhibit a comparable gradient strength within the first 50 mm of the fibers, where most of the nonlinear broadening occurs. At longer fiber lengths with nano-film thicknesses larger than 110 nm, where gs differs a lot for different fibers, the dispersion is fully normal dispersive, not contributing to nonlinear frequency conversion. Therefore, Set 2 can be seen as a study of different starting thicknesses at similar gradient strengths. The gradient strengths of linear fits, only considering the first 40 mm, vary from $gs = 0.87$ nm/mm to $gs = 1.13$ nm/mm including the estimated correction factor $f_c = 0.9$ and form the data points presented in Fig. 5.12c. This correction factor is a mean value of the ones individually found for Set 1 and can be confirmed in magnitude by experimentally measuring the nano-film thickness on the core compared to a position on the outside of the fiber (Section 4.3.3).

For decreasing starting thicknesses from $t_s = 74$ nm down to $t_s = 62$ nm, there is an enhancement of the bandwidth on both sides of the spectrum (Fig. 5.17). Here, the starting thickness values refer to the t_s of the model in Fig. 5.16. Because the ZDW is closer to the pump wavelength and the soliton for thicker nano-films, also the first DW appears closer to the pump. Similar to the study with constant TiO_2 nano-films, the first DW blue-shifts as the ZDW decreases in wavelength for thinner starting thicknesses. For even thinner t_s below 62 nm the conversion efficiency decreases so that the first DW cannot be detected at all. One reason is the modal overlap integral of the DW and the

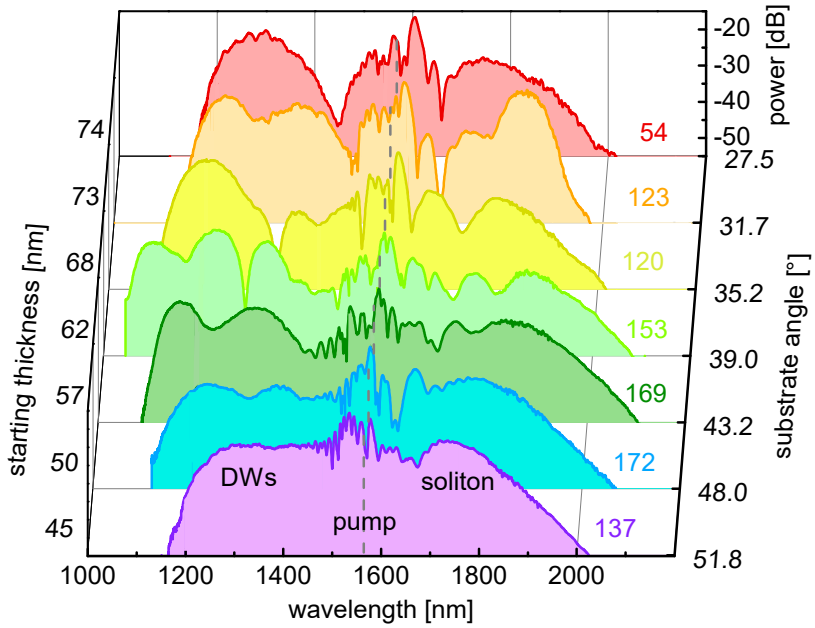

Figure 5.17: Experimental output spectra of ECFs coated with nano-films with the thickness gradients shown in Fig. 5.16 at maximum input power with their figure of merit displayed in color-matched numbers. The pump wavelength is marked with a gray dashed line.

soliton, which decreases for DWs with shorter wavelength as the mode gets more confined to the nano-film. On top of it, moving towards shorter wavelengths near the anti-crossing wavelengths, approaching the resonance will increase the optical losses. Both effects are not included in simulations, which still match the experiments and thus, cannot be the primary reason for the non-existence of the first DW in experiments below $t_s = 62$ nm. Instead, purely concerning the dispersion, the ZDW is spectrally far away from the soliton for thinner nano-films, increasing the absolute value of β_2 at the soliton frequency. This also leads to a reduction in the conversion efficiency and the corresponding vanishing of the first DW, making the second DW generated at positions further from the fiber start being the lowest wavelength feature detectable (Fig. 5.18). Because the soliton already formed, red-shifted, and suffered from optical as well as Raman losses, the creation of the second DW is not comparable to the first DW. Hence, although the dispersion at the creation point of a second DW for a fiber with low t_s might be identical to the dispersion for the first DW for a fiber with higher t_s, the second DW will never reach the same short wavelengths possible with first DWs. As the bandwidth for the samples with $t_s < 62$ nm cannot rival the ones for higher t_s, the focus for those samples was shifted more towards reaching the maximum possible uniformity. This argumentation is in line with the FoM considerations of Fig. 5.12 as the gradient parameters fall below the highly visible edge of the graph.

For Set 1, the laser parameters, in particular the prism position to control the chirp of the pulses before the main amplifier is kept constant to ensure comparable conditions for

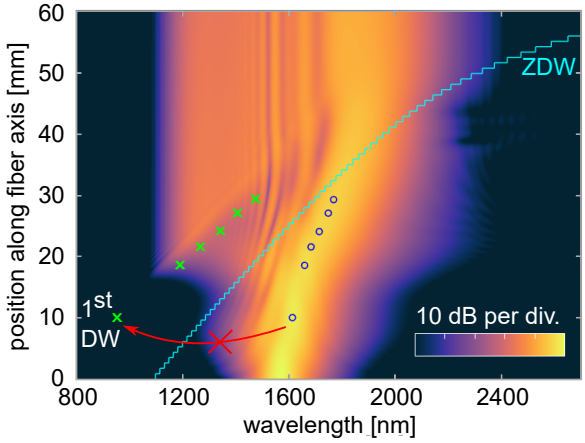

Figure 5.18: Pulse propagation simulation of an ECF with a Ta_2O_5 nano-film with linearly increasing thickness from $t_s = 50$ nm to $t = 135$ nm within a length of 75 mm ($gs = 1.13$), pumped with an input peak power of 15 kW. The cyan line is the ZDW and green crosses mark the phase-matching wavelengths calculated with Eq. 2.20 when using the soliton wavelengths indicated by the blue circles.

all samples. However, here, they are actively used to help shaping the output spectrum. For instance, non-optimal incoupling or prism positions could reduce the in-fiber peak power. On top of it, the higher absolute β_2 values for thinner t_s is connected to a smaller soliton number. With less soliton breathing the distinct generation of individual DWs is reduced, leading to a more uniform output spectrum on the short-wavelength side in the DW region.

Again, the long-wavelength side is determined by the soliton dynamics. For the fibers from $t_s = 74$ nm down to $t_s = 57$ nm the soliton is Raman-shifting further to the IR as the decreasing nano-film thickness along the entire fiber enlarges the length before the fiber gets normal dispersive. This gives the soliton more time to red-shift. For even thinner nano-films, the larger absolute dispersion and reduced soliton number overcome the length effect and lead to an overall reduced bandwidth.

In this study, the total bandwidth is maximized for the fiber with $\varphi = 39°$ while the enhanced spectral uniformity for steeper angles shift the maximum of the FoM to the sample with $\varphi = 48.0°$. For the latter, a spectral interval with a maximum variation of 5 dB from 1180 nm to 1505 nm with a standard deviation of 1.4 dB could be achieved. The best flatness realized was possible with the steepest fiber at $\varphi = 51.8°$. Within 1270 nm and 1460 nm the maximum variation and the standard deviation is 1.5 dB and 0.4 dB, respectively. On top of it, at longer wavelengths across some nonuniform section near the pump wavelength, the soliton at 1750 nm ($\varphi = 48.0°$) and 1700 nm ($\varphi = 51.8°$) are on a similar power level compared to the DW section.

Set 2 shows that both nearly octave-spanning spectra and excellent uniformity are possible by longitudinally varying the dispersion in resonance enhanced ECFs. However,

it is not possible to maximize both of them simultaneously within one sample as there is a trade-off. Nonetheless, also the fibers with the broadest spectra consist of multiple DWs that, especially in comparison to uniform TiO_2 nano-films, exhibit greatly improved flattened spectral coverage.

5.3.6 Losses

In the nonlinear pulse propagating simulations, losses were used as a variable and are varied from 0.1 dB/cm to 1.4 dB/cm to match the simulated to the experimentally obtained spectra. Although losses are assumed to be constant, in reality, they are wavelength dependent. For instance, distinct O-H absorption bands, broadband infrared silica absorption and losses associated with resonances are present and influence the measured spectra. For two samples with nano-film thicknesses of 73 nm and 115 nm, the losses are measured with a cut-back method[233]. In detail, broadband light from a supercontinuum source (SuperK Compact, NKT Photonics) is coupled into the fiber with a 20× objective (for VIS). The long pulse durations (2 ns) in combination with a moderate average power ensure the avoidance of any nonlinear frequency conversion within the fiber. The output light is collected with a butt-coupled fiber (P1-980A, Thorlabs Inc.) and analyzed with a spectrometer (AQ6374, Yokogawa Corp.). Having the collection fiber gently touch the sample fiber minimizes spectral errors from potentially different outcoupling conditions. The method is based on cutting back the sample fiber on the outcoupling side while keeping the incoupling side constant. This way the difference of the output spectra for different fiber lengths represents the losses of the length of the cut-back section, ideally without the influence of in- and outcoupling.

For an uncoated ECF, this method reveals fiber losses of < 5 dB/m within the spectral interval from 600 nm to 1.7 µm, with the exception of an O–H absorption band at $\lambda = 1398$ nm (Fig. 5.19a). This absorption band could be caused by adsorbed water on the surface of the core, water vapor in the air holes interacting with the evanescent field or O-H groups within the core material[259]. Apart from this peak, the losses measured for the coated fibers are to be associated with the nano-film. These include the enhanced base-line absorption of (10–20) dB/m and the enhanced losses at the short-wavelength side up to 50 dB/m. The latter can be connected to losses of the nano-film resonance, as they coincide with the mode anti-crossing wavelength. In agreement with Fig. 3.4, the anti-crossing is located at shorter wavelengths for thinner nano-films, matching the findings of the loss measurements. In contrast to the simulated spectra, the experimentally measured ones exhibit O–H absorption band caused dips near $\lambda = 1.4$ µm, best visible in the power evolution plots (Fig. 5.14f–h), matching the loss peaks shown in Fig. 5.19. On top of it, they also show the start of the next O–H absorption band starting from $\lambda \approx 1.9$ µm, which is outside of the measurement range of the cut-back measurement.

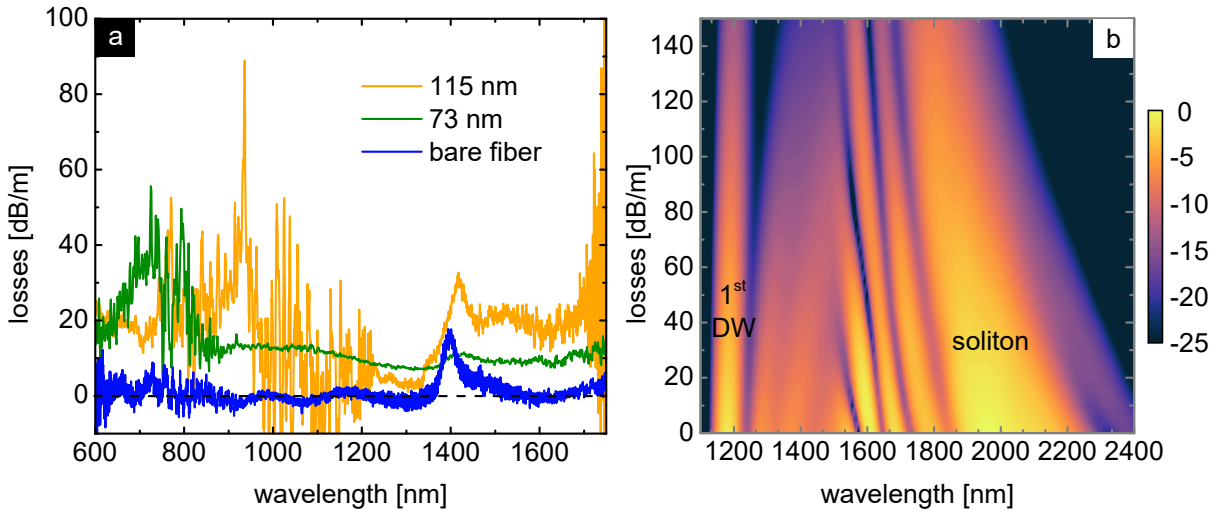

Figure 5.19: (a) Losses of ECFs with various Ta_2O_5 nano-film thicknesses measured with the cut-back method. (b) Simulated spectrum and the influence of spectrally constant losses for the fiber of Fig. 5.11c (t_s = 62 nm, t_{end} = 135 nm, fiber length: 75 mm, input peak power P = 15 kW).

Apart from spectrally localized dips in the spectra, losses also have a global effect as they modify the pulse propagation along the fiber. Especially the long-wavelength edge of the spectra is affected by losses as a reduction of the soliton power reduces its Raman red-shifting. For instance, solely varying the spectrally constant losses in simulations from a lossless situation to 140 dB/m can shorten the -10 dB long-wavelength edge from 2245 nm down to to 1960 nm (Fig. 5.19b) on the example of the fiber also used in Fig. 5.11. There are peaks visible at shorter wavelengths that shift parallel to the broadest and most red-shifted soliton, that can be partly attributed to other solitons after soliton fission. As the broadest soliton mainly contributes to the DW generation, here, all the other solitons can be ignored. As a consequence of the blue-shifting, the main soliton with reduced wavelength generates secondary DWs that, in turn, are located closer to the pump wavelength. However, as the soliton is generated at a similar wavelength and only experiences a loss-dependent red-shift further into the fiber, the first DW created before the red-shift and thus the short-wavelength edge of the spectrum is nearly unaffected by losses.

The example of this section shows the importance of keeping the losses as low as possible in order to achieve broader spectra and decrease the potential spectral gap between different DWs. Simulations suggest that potentially increasing the input power (not possible with our laser) or reducing losses will enhance the overall Raman shift. Losses can be attributed to scattering at the rough surface of the nano-film and its defects within the layer. Perfectly stoichiometric Ta_2O_5 has little material losses[227], but deviations in the material composition will increase them[230]. The surface quality can be potentially improved by adapting a surfactant sputtering technique[231,232] or annealing[229] to avoid

the formation of the bigger particles present in the current nano-films (Fig. 4.8). Yet, optimizing the material properties of nano-films is beyond the scope of this work.

5.3.7 Coherence

Because of the low soliton number and the short pulse duration used here, neither high order soliton fission nor MI is utilized as broadening mechanism. This suggests a high pulse-to-pulse stability, which is required for many applications such as scanning techniques. A hypothetical test fiber with a length of 75 mm and a linear gradient having a nano-film thicknesses increasing from $t_s = 62$ to $t = 135$ nm ($gs = 1.04$ nm/mm, same fiber as in Fig. 5.11) is excited with a pulse with a width of 35 fs (FWHM) at $\lambda = 1570$ nm and 15 kW peak power. Calculating the ensemble averaged first-order degree of coherence (Eq. 2.29) for a set of 20 individually simulated spectra with 190 unique pairs confirms excellent spectral stability throughout the entire spectrum and along the whole fiber (Fig. 5.20). Here, the noise used includes a 10^{11}-fold multiplied one photon per mode with random phase model[165], effectively generating a noise floor of -44 dB compared to the broadened pulse. On top of it, random independent peak power and pulse duration fluctuations of up to 2 % (equally distributed) modify the pulse as expected for a realistic mode-locked fiber laser at the telecommunication wavelength[260].

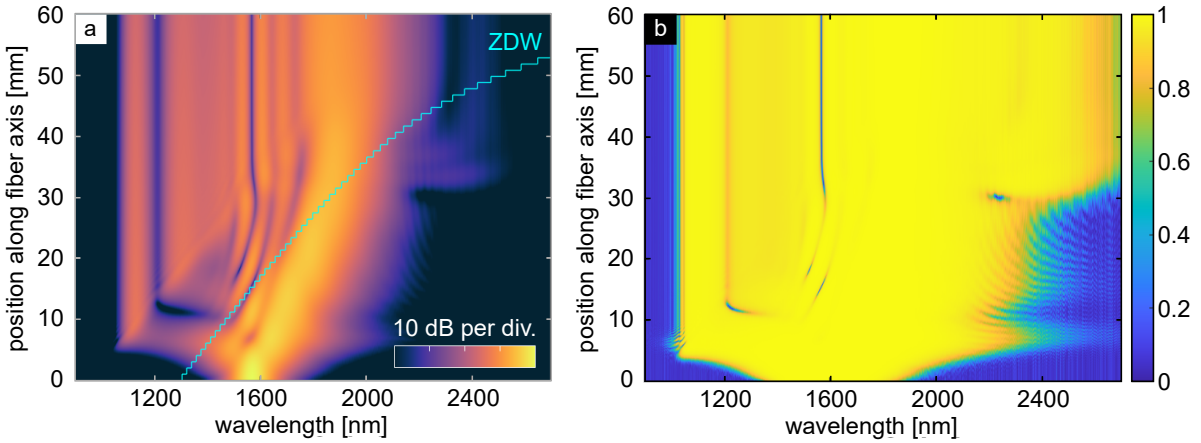

Figure 5.20: (a) Simulated spectrum along the fiber also used in Fig. 5.11 (nano-film thickness from $t_s = 62$ nm to $t = 135$ nm within a length of 75 mm, input peak power $P = 15$ kW). The cyan line indicates the ZDW. (b) Ensemble averaged first-order degree of coherence of 20 individual spectra of the fiber of (a) including noise defined in the main text and using Eq. 2.29.

5.3.8 Discussion and conclusion

Individually shaping the output spectrum for specific applications demands precise dispersion management in fibers. Especially for limited pump energy with femtosecond pulses, realizing tailored broadband and flat output spectra is challenging. Longitudinally varying

the dispersion in fibers starting in the AD domain and increasing the dispersion along the fiber enables the generation of multiple DWs from a single soliton at low soliton numbers $N_{\mathrm{sol}} < 2$. In contrast to the constant TiO_2 nano-films, the phase-matching condition is adaptable for every DW at the local creation position along the fiber. The DWs spread across the spectrum on the short-wavelength side of the pump and fill the gap between the first DW and the soliton to form a more uniform, but strongly chirped spectrum. This technique uniquely achieves the creation of soliton based broadband and uniform spectra at low input energies while maintaining excellent coherence according to simulations. The required dispersion with a red-shifting ZDW is realized by nano-films with a gradually increasing thickness along the ECFs, achieved by a tilted deposition method. The nano-film properties, especially the starting thickness and the gradient strength are optimized to tune the output spectrum for maximizing uniformity and bandwidth. Characterizing the quality of the resulting spectra, a meaningful FoM is introduced and the spectra are evaluated. The presented concept not only enables the creation of more uniform spectra, longitudinally varying the dispersion also modifies the soliton dynamics and extends the bandwidth towards the infrared by 200 nm. Therefore, it has the potential to realize novel types of highly coherent ultrafast nonlinear light sources with tailored properties.

Despite the success to tune the spectral output simply by varying the angle of the substrate in the sputtering chamber, further improvements on the spectrum could be achieved by shaping the nano-film in a more sophisticated way. Coating a bent fiber instead of using straight substrates could overcome the limited shapes dictated by the deposition characteristics described by the sputtering model. On top of it, ultimately unlocking full control of the nano-film thickness along the entire fiber implies surpassing the restriction of a continuous thickness function. This could be implemented by subsequent nano-film depositions with exchangeable masks or a freely moving slit mask, externally readjustable during the deposition process. With the new degrees of freedom, for example, enabling cascaded DW formation[252] at wavelengths closer to each other and overlapping in wavelength, advanced spectral tailoring can be envisioned.

One method taking advantage of the freely designable non-continuous nano-films is using periodic structures, enriching the nonlinear frequency conversion by adding quasi-phase matched features to the spectrum as will be discussed in Section 5.4.

5.4 Periodically structured Ta_2O_5 nano-films

SCG excels at providing bright light sources with a broad spectral range. Especially by tailoring the dispersion longitudinally along the waveguide and through cascaded processes, creation of spectra ranging over seven octaves is possible[261]. However, most applications only require a light source with a specific wavelength range that is overspun by most broadband sources. This wastes energy in unwanted spectral regions, causing thermal

load, photo-toxicity, and reduces the conversion efficiency towards the wavelengths of interest[262]. Therefore, tailored frequency conversion to selected wavelengths is desirable. In particular, multi-color light sources are of interest for applications in medical diagnostics[263], biophotonics[264] and environmental science[21]. Compact and robust fiber laser based sources are needed for miniaturizing and single-fiber solutions reduce the complexity of systems for clinical applications, for example in-vivo hyperspectral imaging[35,70,265]. Parametric processes such as four wave mixing can generate bright coherent light at user-defined spectral bands[266,267], yet, they are mostly limited to two to three simultaneous output wavelengths. Hence, multi-color coherent ultrafast tunable light generation requires novel simple-to-use approaches.

Here, multi-color light creation is realized by multi-order DW generation using QPM. Periodically coating ECFs with nano-films modifies the fiber dispersion substantially, creating an effective dispersion (Section 3.2.3). With the additional geometric wave vector the phase-matching condition of the soliton to the DW changes, allowing for the generation of multiple new higher-order DW peaks (Section 2.3.6). The flexible design and the fast adaptability of the nano-film geometry form an excellent basis for optimization and tuning of the output spectra.

5.4.1 Fabrication of structured nano-films

Fabricating periodically modulated nano-films could be done with high precision lithography as used for waveguides or in the wafer/semiconductor industry. However, this technique would require expensive equipment, heavy machinery and special working environments. On top of it, it is a challenge to apply it to curved surfaces, movable substrates, and inside partly covered fiber grooves. As sub-micrometer tolerances are not required for millimeter sized structures for the goals of these experiments, a physical mask is sufficient, faster, cheaper, and more practicable. Here, the mask is precisely cut from standard kitchen-grade aluminum foil using a TruMark Station 1000 commercial laser cutter (Trumpf GmbH, Fig. 5.21a). Creating an array of rectangular holes with a height of 4 mm and a width of half a period length allows for a flexible wrapping of the foil around the fiber in the transverse direction without compromising the periodicity of the mask in the longitudinal direction. Taping the foil to the substrate through the holes with Kapton Tape ensures a tight contact of the mask to the top of the fiber for every single ridge (Fig. 5.21b).

This method of spanning the mask across the outside of the fiber leaves a gap of 70 µm from the mask to the fiber core. Thus, a directed nano-film deposition technique needs to be employed for the mask to work as intended. Because of the successes and experiences with sputtered Ta_2O_5, this deposition method and material are also chosen for periodic nano-film fabrication. Because sputtering is not as directed as, e.g. thermal evaporation, the sample-mask geometry causes a small transition region between the coated and un-

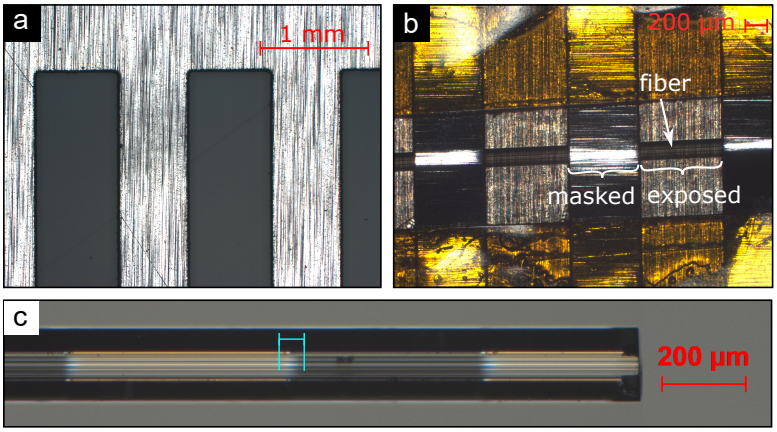

Figure 5.21: (a) Microscope image of a laser-cut aluminum foil mask with $\Lambda = 1.409$ mm. (b) A partly covered ECF with the mask of (a) fixed with Kapton tape (yellow) on a metal substrate. (c) Microscope image of a periodically coated ECF ($\Lambda = 1$ mm) with the view through the fiber groove on the core. Bright regions of the fiber are coated sections and the transition region is marked with a cyan line (60 µm).

coated sections. With preliminary experiments testing the masking properties for different spacers on planar substrates, a transition region of about 60 µm can be estimated for the ECF. Microscope images of the coated fiber showing a discoloring confirm the dimensions (marked cyan in Fig. 5.21c). Albeit realistically trapeze-shaped with rounded edges, in simulations, the nano-film is assumed to have sharp transitions and follow a periodic square function. With the transition region being a tenth of the period length in the worst case ($\Lambda = 0.625$ mm), the effect of the transition region on the nonlinear pulse propagation is only minor, vindicating the simplification of neglecting it.

After deposition the fibers are cleaved within the periodically coated section, avoiding longer uncoated sections at the fiber ends to ensure that the entire fiber has a uniform effective dispersion. Interestingly, the exact cleaving position determining the type (coated/uncoated) and length of the first segment has no significant influence on the resulting spectrum. For instance for a fiber with a long period length of $\Lambda = 3$ mm, where the effect is expected to be stronger compared to shorter period lengths, simulations suggest a maximum variation of only $\Delta\lambda = 1.7$ nm in the wavelength and $\Delta P = 0.3$ dB in peak height of the DW.

Characterizing the samples, the period lengths can be measured with a microscope across multiple periods of the mask. Additionally, this also reveals the cutting laser width and design-flaw based non-symmetry of the mask grating. The latter can be expressed by the filling fraction *ff*, defined as the fraction of cut-away material in comparison to the total period length (Section 3.2.3). Finally, the thickness of the nano-film is evaluated by ellipsometry on planar substrates placed next to the fiber during the deposition process. Yet, it is adapted and treated as a free parameter to match simulated results to the

experimental spectra, effectively accounting for the unknown factor f_c (in-fiber nano-film thickness correction factor, Section 4.2.2). On the example of the fiber used for Fig. 5.22, the measured thickness is $t_{\text{ellipsomety}} = 104.5$ nm, leading to $f_c = 0.82$.

5.4.2 Multi-order DWs in experiments

Launching a femtosecond laser at the maximum average power of $P = 192$ mW into the ECF with a nano-film period length of $\Lambda = 1.409 \pm 0.005$ mm and a thickness of $t = 85.5$ nm as depicted in the experimental setup (Fig. 5.1) gives the output spectrum presented in Fig. 5.22b. The core spectrum (white background) is similar to the spectra presented before for the constant thickness nano-films (Section 5.2). It can be explained and recreated by nonlinear pulse propagation simulations using the effective dispersion (spectrum: pink dotted line). In all simulations of this figure, a wavelength independent loss of 10 dB/m is included. The pure individual sections of the fiber are not suitable for nonlinear frequency conversion as the uncoated section has a ZDW (near $\lambda = 800$ nm) spectrally too far away from the pump wavelength and the coated sections are ND at λ_p

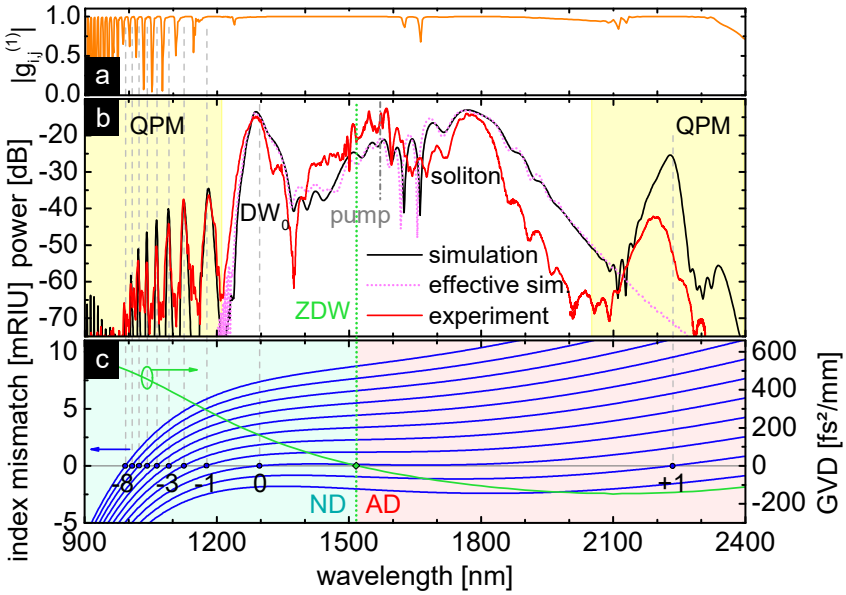

Figure 5.22: (a) Ensemble first order coherence of 20 individual simulated spectra (one of them shown in (b)) with the noise defined in the main text. (b) Experimental (red) and simulated (black) output spectrum of a periodically coated ECF with a maximum thickness of $t = 85.5$ nm and a period length of $\Lambda = 1.409$ mm at maximum average input power of 192 mW. The pink dotted line is a simulation using the effective dispersion. The spectrum is enhanced by QPM peaks, highlighted by yellow shaded areas and the central pump wavelength is marked by the vertical dash-dotted grey line. (c) Phase mismatch calculations for different values of q (left ordinate). The phase matching wavelengths are marked with blue circles and vertical dashed gray lines. Right ordinate: Effective GVD including the effective ZDW marked with a green diamond and a vertical dotted line, dividing the plot in a normal dispersive (ND, turquoise) and anomalous dispersive domain (AD, red).

(Fig. 3.5). Solely by combining them to a longitudinally invariant effective dispersion via the filling fraction weighted mean dispersion of the coated and uncoated fiber sections (Eq. 3.32) enables nonlinear spectral broadening. The effective dispersion (green line in Fig. 5.22c) exhibits a ZDW at 1515 nm, making the fiber AD at the pump wavelength of $\lambda_p = 1570$ nm.

A soliton is formed on the long-wavelength side of the pump that generates a DW at 1289 nm. This is the usual DW associated with soliton based SCG without QPM, being termed DW_0 (Section 2.3.6). Phase matching calculations using Eq. 2.20, the effective dispersion, and the soliton wavelength $\lambda_s = 1675$ nm can accurately confirm the spectral position of the DW_0 (Fig. 5.22c), which is identical to using Eq. 2.23 with $q = 0$.

Including the QPM term in the PM equation, multiple higher-order PM wavelengths are predicted. On the short-wavelength side of the DW_0 are the ones with negative q values and on the long-wavelength side of the soliton are the ones with positive q values. Comparing these PM wavelengths with the additional peaks of the experimental spectrum outside of the core region (yellow background in Fig. 5.22b) confirms the origin of those peaks. The mean deviation of the PM wavelengths to the experimental peak wavelengths from q = -8 to $q = 0$ is only 2 nm. This match validates the usage of the effective dispersion for PM considerations, accurately predicting the QPM peaks.

Pulse propagation simulations using the effective dispersion do not show the QPM peaks. They become visible only when switching to the realistic alternating dispersion along the fiber length (black line in Fig. 5.22b). The simulation matches well with the experimental spectrum in the whole wavelength range and closely overlaps with the simulated spectrum using the effective dispersion within the core spectral region without the QPM peaks.

Owing to the low input power and the low soliton number, MI and high order soliton fission is avoided as for the previously discussed fiber designs (Section 5.3). The absence of these effects keeps the spectral evolution deterministic and leads to a high coherence (Eq. 2.29). As before, the ensemble averaged first-order degree of coherence is calculated based on 20 individually simulated spectra with noise (Fig. 5.22a). Here, the noise consists of a 10^{12} fold multiplied one photon per mode model with random phase [165]. On top of this -35 dB noise floor compared to the maximum spectral power of the pulse, there is a random pulse amplitude and pulse duration variation of 2%, consistent with the argumentation in Section 5.3.7. The coherence is close to 1 within the core spectral region and for every QPM peak, proving excellent pulse-to-pulse stability in simulations. Low coherence can only be found between the QPM peaks and outside the spectrum where the spectral power and the signal to noise ratio is small.

5.4.3 Spectral-spatial evolution of the QPM peaks

To better understand the system it is worth analyzing the evolution of the QPM peaks in the spectral and temporal domain, comparing simulations using the alternating dispersion (Fig. 5.23a+b+e) with simulations based on the effective dispersion (Fig. 5.23c+d+f). For the temporal evolution, the reference time frame is given by the group velocity of the pump wavelength. With the dispersion changing twice during one period length, this leads to the zig-zag behaviour in time in the alternating dispersion case. As for the single spectrum at the end of the fiber discussed in the previous sub-section, the pulse evolution of the core spectral region is almost identical in both simulations compared here and the main difference only lies in the existence of the QPM peaks. For the effective dispersion simulation, there is a spectral broadening visible that occurs within the interval from 5 mm to 20 mm from the start of the fiber. This can be associated with the temporal compression of the pulse, i.e. SSC at the initial formation of the soliton[268]. The spectral broadening can be also seen in the integral of specific spectral intervals along the fiber (Fig. 5.23f). Because the dark green curve represents the interval featuring the DW_0, it

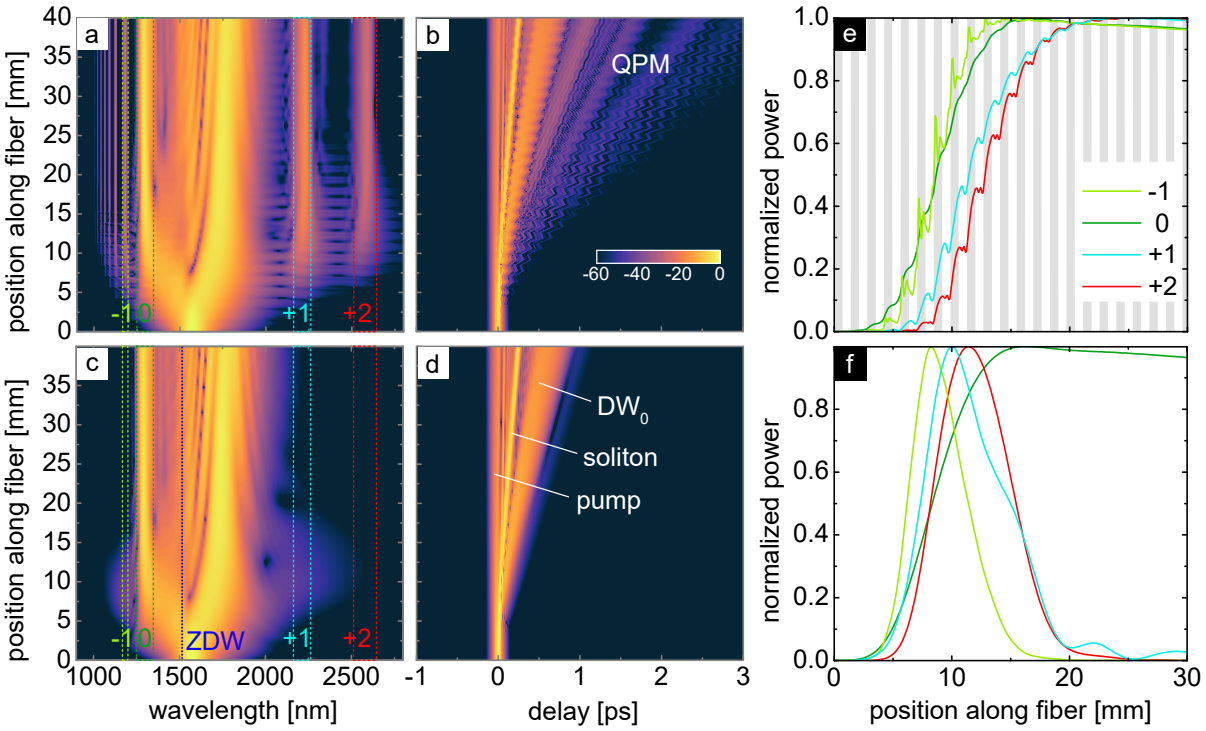

Figure 5.23: Simulated nonlinear pulse propagation for the fiber used for Fig. 5.22 ($\Lambda = 1.409$ mm, $t = 0...85.5$ nm, $P = 11.8$ kW) in the spectral (a+c) and temporal (b+d) domain, using the alternating dispersion (a–b) and effective dispersion (c–d). The common color scale, displayed in (b), is in dB. (e–f) Evolution of the normalized linear optical power integrated within certain spectral intervals, referring and color-matched to QPM-DW peaks of order $q = -1$ to $q = +2$ in (a+c). The gray areas in (e) represent the sections of large nano-film thickness. All curves in (e+f) are normalized individually and cannot be compared in their relative intensity.

is the only one not vanishing after the SSC region. The slow exponential decay near the fiber end (better visible when extending the x-axis) is fully explainable by the linear losses included in the simulation.

In line with Section 2.3.5, the spectrally broadened soliton not only seeds the DW_0, but also the higher-order DWs. The required spectral overlap of the soliton and the higher-order DWs can be best seen when comparing the integrated power along the fiber of the simulation using the effective dispersion (Fig. 5.23f) with the simulation using the alternating dispersion (Fig. 5.23e). The integrated power of the intervals containing the QPM peaks of order -1, $+1$, and $+2$ reveal that they are only generated within the SSC region. It is notable that the $q = +1$ peak emerges earlier and overlaps the $q = +2$ peak at the end of their creation, which is exactly mirrored in their SSC region. The QPM peaks with positive q value (blue and red curves) are amplified within the fiber sections coated with the nano-film, represented by the light gray background. Meanwhile, in the sections without nano-film, the power of the QPM peaks almost stagnates. Contrarily, for the $q = -1$ power evolution (light green curve), it increases sharply near the transition to the coated fiber sections. The difference in the exact amplification positions could be connected to the different GVD sign of the QPM peaks compared to the soliton. This causes the QPM peaks with positive q value to zig-zag in phase with the soliton in the temporal pulse evolution diagram (Fig. 5.23c) while the ones with negative q value have a pi phase shift.

The overall similar shape of the QPM peak power evolution compared to the DW_0 power evolution suggests a similar origin and physical principles. That is, the DW requires spectral overlap with the soliton, causing seeding and amplification. Yet, solely by analyzing the two situations in both simulations here, a clear comparison of the spectra with and without additional peaks is possible. Getting this insight into the spectral evolution cannot be achieved for the DW_0, showing also educational advantages of QPM-DWs.

The creation of the spectrum can also be visualized by a spectrogram at different positions along the fiber, i.e. the spectrum resolved at different temporal delays. At the fiber position of 19.5 mm, the situation is displayed for the alternating dispersion simulation in Fig. 5.24a and for the effective dispersion in Fig. 5.24b. Both are calculated by the FROG method described in Section 2.3.10 using a 60 fs sech^2 gating (FWHM) to balance spectral and temporal resolution. Considering the simulation using the effective dispersion, no QPM peaks can be found. Instead, the spectral SSC braodening is visible, indicating the region where QPM peak generation happens. This region is highlighted in the plot for the alternating dispersion with dashed ellipses. The FROG simulations reveal that the QPM peaks are generated at the same delay as the soliton in several waves once per period, consistent with the findings of Fig. 5.23. In contrast to the soliton, the DWs disperse in time during their propagation, but overall remain within a time slot of a few hundred femtoseconds. The front edge of the spectrogram facing towards positive delays

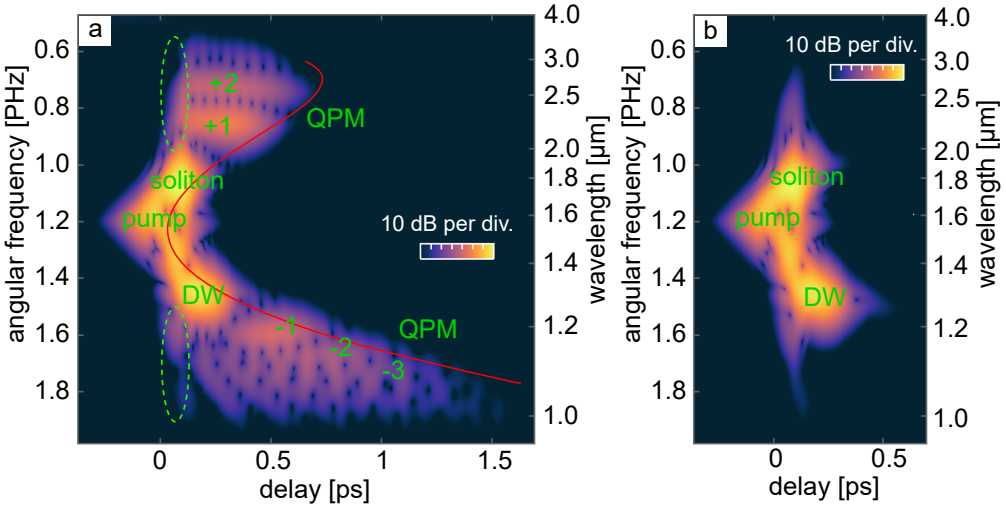

Figure 5.24: FROG simulation of the fiber used in Fig. 5.22 ($\Lambda = 1.409$ mm, $t = 0...85.5$ nm, $P = 11.8$ kW) with alternating dispersion (a) and effective dispersion (b) at a fiber length of 19.5 mm (gating: 60 fs sech²). QPM peak creating regions are marked with green dashed ellipses and the red line indicates the group-velocity-caused walk-off over a length of 14 mm.

matches well with the shape of the effective group velocity (Fig. 3.6). It is consistent with the anticipated walk-off of different spectral features having different group velocities over the length of 14 mm (red line in Fig. 5.24a), ignoring the propagation length of ~ 5.5 mm before the spectral broadening initiates (see Fig. 5.23a). The QPM peaks with positive q values span in time from this front edge up to the QPM creation area (green dashed ellipse) as they are created continuously up to this position along the fiber (19.5 mm). Contrarily, the peaks with negative q already passed their main amplification region, thereby also starting from the front edge but not reaching the soliton temporal position. As for the fibers with a thickness gradient, the resulting spectra are chirped, but here, the temporal order of the different spectral features is not consistent with the wavelength ordering. All QPM pulses arrive later at the end of the fiber compared to the remaining pump pulse and the exact time delay depends on the order q and the fiber length.

Additionally, the spectrogram enables easy access to read out the temporal width $\Delta\tau_{\text{spect}}$ of the individual spectral features of the spectrum. Another approach for obtaining the pulse duration is to measure the experimental -3 dB bandwidth $\Delta\lambda$ of the individual QPM peaks and calculate the Fourier-transform limited temporal width $\Delta T_{\text{FT-limited}}$ under the assumption of sech² pulse shapes. Furthermore, the walk-off of the QPM peaks during their creation length l_{creation} (taken from Fig. 5.23e) needs to be considered to estimate the temporal width of the created pulses[18]

$$\Delta\tau_{\text{walk-off}} = (\beta_{1,\text{DW}_x} - \beta_{1,\text{soliton}}) \cdot l_{\text{creation}}. \tag{5.36}$$

Table 5.2: Estimation of temporal and spectral properties of the QPM-DWs.

DW order (DW_x)	$\Delta\lambda_{-3\ dB}$ [nm]	$\Delta\tau_{FT\text{-}limited}$ [fs]	$\Delta\tau_{walk\text{-}off}$ [fs]	$\Delta\tau_{spect}$ [fs]
-4	4.1	290	-	-
-3	3.9	320	-	-
-2	5.2	255	-	-
-1	11	136	280	217
0	32	54	140	116
1	43	119	336	197

The results of all three methods are collected in Table 5.2 and clearly suggest sub-picosecond pulse durations. This opens the possibility of tunable femtosecond pump probe experiments using separate features of the spectrum, e.g. to reveal ultrafast electronic dynamics in single molecules[269].

5.4.4 Input power dependency

Launching the pump pulses at various powers into the fiber leads to the different experimental and simulated spectra shown in Fig. 5.25a and b, respectively. As the power increases, the soliton is created at longer wavelengths and on top of it experiences a more pronounced Raman red-shift. This directly affects the spectral position of the DW_0 through the PM condition, resulting in a blue shift with increasing power. Interestingly, the spectral positions of the QPM peaks are nearly unaffected by the power level compared to light in the core spectral region. This can be explained by the steeper phase mismatch

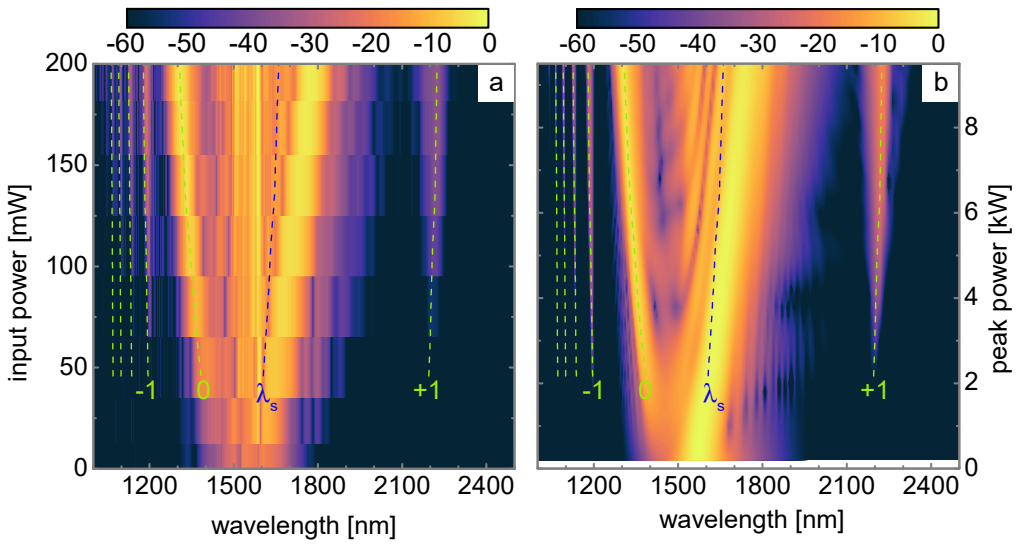

Figure 5.25: Experimental (a) and simulated (b) input power evolution of the spectrum of the fiber used for Fig. 5.22 (Λ = 1.409 mm, t = 0...85.5 nm, P = 11.8 kW, color scale in dB). The green dashed lines are phase-matching calculations using Eq. 2.23 and the soliton wavelength marked by the blue dashed line.

curves at the outer regions of the spectrum (Fig. 5.22c), making them less susceptible to the offset by the power dependent nonlinear phase in Eq. 2.23.

The experimental findings can be completely reproduced by nonlinear pulse propagation simulations, matching the spectrum at all power levels. Furthermore, PM considerations can track the theoretical position of all spectral features (Eq. 2.23), assuming the soliton wavelength indicated by the blue dashed line. Here, the soliton wavelength at the creation point of the DWs is of importance. That is why the used soliton wavelengths do not overlay with the spectral position of the solitons visible in the figure as they include the Raman shift after the DW creation.

5.4.5 Nano-film modulation depth

For the exemplary periodically coated ECF discussed so far, the modulation depth of the nano-films is the maximum possible one for the selected effective dispersion. That is, the fiber consists of sections without nano-film (thickness: $t = 0$ nm) and sections with a thickness of $t = 85.5$ nm. As a consequence, the ZDW changes its sign twice each period for all wavelengths of the spectrum shorter than $\lambda = 1740$ nm, while for longer wavelengths it is constantly AD along the entire fiber. In comparison to the required change of the sign of the nonlinearity in periodically poled crystals for QPM enabled parametric amplification[270], the modulation of the GVD is the origin of QPM[71], which does not necessarily demand a change in sign. This can be proven by reducing the modulation depth of the thickness of the nano-film in simulations. In order to allow for a direct comparison, it is useful to consider a fiber with a similar effective dispersion. Therefore, a nano-film thicknesses variation around the uniform thickness situation with $t = 74$ nm of Fig. 3.6 is appropriate, e.g. from $t = 73.5$ nm to $t = 74.5$ nm. In this case the change of the GVD sign only occurs within the small wavelength interval of 1514 nm $< \lambda <$ 1533 nm,

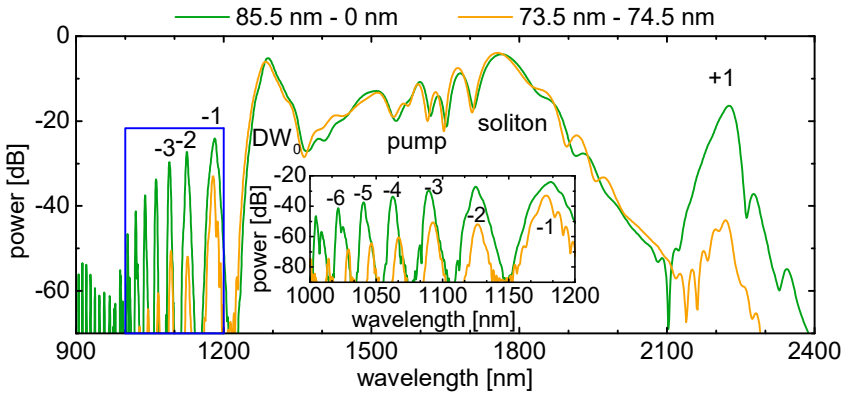

Figure 5.26: Comparison of the simulated spectrum shown in Fig. 5.22 ($\Lambda = 1.409$ mm, $t = 0...85.5$ nm, $P = 11.8$ kW) (green) to a simulation with identical parameters, except for a smaller nano-film modulation depth of 1 nm around $t = 74$ nm with comparable effective dispersions (yellow, compare to Fig. 3.6). The inset shows the magnified negative q QPM-DWs of the blue box.

which does not include λ_p. Nonetheless, clear QPM peaks are observable in simulations, although being less pronounced compared to the stronger GVD modulation (Fig. 5.26). The similar effective dispersion in the core region from the DW_0 to the soliton leads to a close match of the spectra of both modulations. However, at both spectral ends further away from the central wavelength, the dispersions of the constantly $t = 74$ nm case and thereby also the closely related weakly modulated case differ from the effective dispersion of the highly modulated case (Fig. 3.6). The resulting difference of the spectral positions of the QPM peaks can be seen in the inset of Fig. 5.26, showing that the the effective dispersion of strongly modulated nano-films is unique and cannot be reproduced by any ECF with a constant nano-film thickness.

This study demonstrates that a higher modulation depth of the GVD causes a higher conversion efficiency to the QPM peaks. In comparison to the literature using mostly small geometric modulations of the fiber cross section, the concept of resonance enhanced mode anti-crossing enables high modulation depths (Table 5.3). For a feasible nano-film thickness of $t = 140$ nm the GVD modulation amplitude can reach up to $\Delta\beta_2 = 1300$ fs²/mm, rivaling the ones achieved with on-chip designs.

Table 5.3: Comparison of GVD modulation amplitudes of different periodically modulated fibers and waveguides (in gray) achieved in the literature.

waveguide type	modulation method	GVD modulation amplitude at λ_p	reference
fiber	mode anti-crossing	270 fs^2 mm^{-1}	this work (Figure 5.22)
fiber	outer fiber diameter	3 fs^2 mm^{-1}	Droques et al.[78]
fiber	outer fiber diameter	2 fs^2 mm^{-1}	Copie et al.[271]
fiber	outer fiber diameter	1.2 fs^2 mm^{-1}	Conforti et al.[73,272]
fiber	splicing of fiber sections	45 fs^2 mm^{-1}	Zia et al.[273]
on-chip	waveguide width	364 fs^2 mm^{-1}	Driscoll et al.[68]
on-chip	periodical poling	15 fs^2 mm^{-1}	Jankowski et al.[274]
on-chip	waveguide width	1000 fs^2 mm^{-1}	Lefevre et al.[69]

5.4.6 Influence of the period length

The spectral positions of all QPM peaks can be tuned with the period length. As verified by simulations using identical waveguide and laser parameters as for the fiber used for Fig. 5.22, the longer the period length, the more peaks appear that overall shift towards the DW_0 (Fig. 5.27a). At first glance, the core region of the spectrum excluding the QPM peaks seems to be unaltered by a change of the period length, as is predicted in theory by the effective dispersion consideration. Yet, the close up (Fig. 5.27b) reveals that the period length independence is only valid for small period lengths. Solely there, the spectrum with periodical GVD modulation perfectly coincides with the spectrum using the effective dispersion. At longer period lengths starting from $\Lambda \sim 1.5$ mm, the soliton

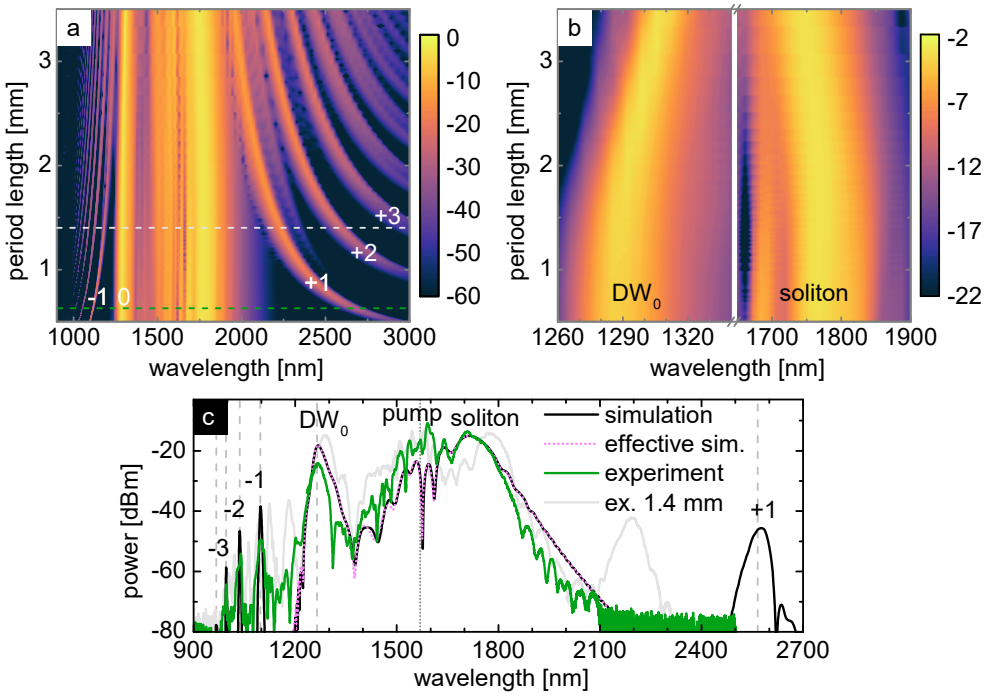

Figure 5.27: (a) Simulated influence of the period length on the output spectrum at maximum input power for the fiber and laser parameters of Fig. 5.22 ($\Lambda = 1.409$ mm, $t = 0...85.5$ nm, $P = 11.8$ kW, colorscale in dB). (b) Magnification of the DW_0 and the soliton of (a). (c) Experimental spectrum of a fiber with a period length of $\Lambda = 0.625$ mm (green) at maximum input power along with simulations using the alternating (black) and effective dispersion (pink, dotted), compared to the spectrum of Fig. 5.22b (light gray line). Vertical dashed lines are phase-matching wavelengths using Eq. 2.23 and the vertical dotted line marks the pump wavelength. Both period lengths are indicated in (a) by color-matched horizontal dashed lines.

and the DW_0 both move towards the pump wavelength. All effective media have a critical length scale Λ_c where the approximation to treat it as a homogeneous medium breaks down. For meta-materials, the scale of the used wavelength is the accepted criterion[275]. Here, the effective approximation holds for much longer length scales, coinciding with the nonlinear length of the sample (Table 5.4). For longer period lengths, the soliton dynamics change, leading to a step-wise different shift of the spectrum consistent with the edges of the nano-film. This overall changes the spectral position of the soliton, also causing the DW_0 to be at a different wavelength. Yet, the change in wavelengths is only a few tens of nm and does not completely resemble the result of the individual sections, both not being able to cause nonlinear frequency conversion as discussed before.

Compared to the sample with $\Lambda = 1.4$ mm, the experimental spectrum from a fiber with a period length of $\Lambda = 0.625$ mm has less QPM peaks at the short-wavelength side of the spectrum and they are further away from each other (Fig. 5.27c). In line with the nonlinear pulse propagation simulation and the PM considerations the QPM peaks at the long-wavelength side with positive q values are outside of the detectable wavelength range. Both simulations using the effective dispersion and the realistically alternating dispersion

Table 5.4: Experimentally measured[a], simulation matched[b], and calculated[c] fiber parameters. L_D: dispersive length, L_NL: nonlinear length, L_f: fission length, *ff*: filling fraction, and t: nano-film thickness.

period[a] mm	*ff*[a]	fiber length[a] mm	P[b] kW	t[b] nm	loss[b] dB m^{-1}	λ_s^b nm	L_D^c mm	L_NL^c mm	L_f^c mm
0.625	0.588	34	8.5	81.3	10	1645	9.6	2.3	4.7
1.409	0.521	39	11.8	85.5	10	1675	18	1.6	5.3
2.494	0.511	36	7.7	79.2	10	1590	5.8	2.7	4.0
3.000	0.506	45	13.0	89.7	10	1690	106	1.4	12

perfectly overlap within the core spectral region. As discussed before, this is a result of the shorter period length and the strengthened effective dispersion approximation. Yet, the core spectrum is slightly different from the sample with $\Lambda = 1.4$ mm, explainable by a different nano-film thickness. Although being coated within the same deposition process, the lateral shift in the position inside the deposition chamber and the different fiber rotational alignments corresponding to individual f_c values lead to a thinner nano-film of only 81.3 nm for the fiber with $\Lambda = 0.625$ mm.

5.4.7 Spectral tuning via the nano-film thickness

Apart from the period length, also the nano-film thickness has an influence on the spectral positions of the QPM peaks, as it determines the effective dispersion, being the basis of the PM considerations.

Coating two more samples with period lengths of $\Lambda = 2.5$ mm ($t = 79.2$) and $\Lambda = 3.0$ mm ($t = 89.7$ nm) gives the experimental and simulated spectra presented in (Fig. 5.28a+b). Despite the simulation of Fig. 5.27a predicting denser QPM peaks for samples with longer period lengths, the fiber with $\Lambda = 2.5$ mm exhibits more peaks on the long-wavelength side. Instead, this contradiction can be attributed to the difference in the nano-film thickness, having a more dominant effect on the QPM peaks in this particular example. On the short-wavelength side, the ECF with $\Lambda = 3.0$ mm has more QPM peaks that together with the DW_0 are located at longer wavelengths.

The influence of the nano-film thickness can be seen in a simulation (Fig. 5.28c) using the otherwise constant fiber, nano-film, and laser parameters of the fiber with $\Lambda = 1.4$ mm used in Fig. 5.22. The core spectral region and especially the DW_0 behave as expected from the thickness dependent considerations of the constant nano-films discussed in Section 5.2. The DW_0 shifts towards longer wavelengths for thicker nano-films. Considering the remaining spectrum outside the core region, all QPM peaks shift almost parallel to the DW_0. This leads to more and more dense QPM peaks for fibers with thinner nano-films at the long-wavelength side, limited by thin layers that also fail to generate the DW_0. Interestingly, the absence of the DW_0 and all negative q QPM peaks for thin nano-films does not prevent the creation of the $q = +1$ peak. The close proximity to the soliton makes

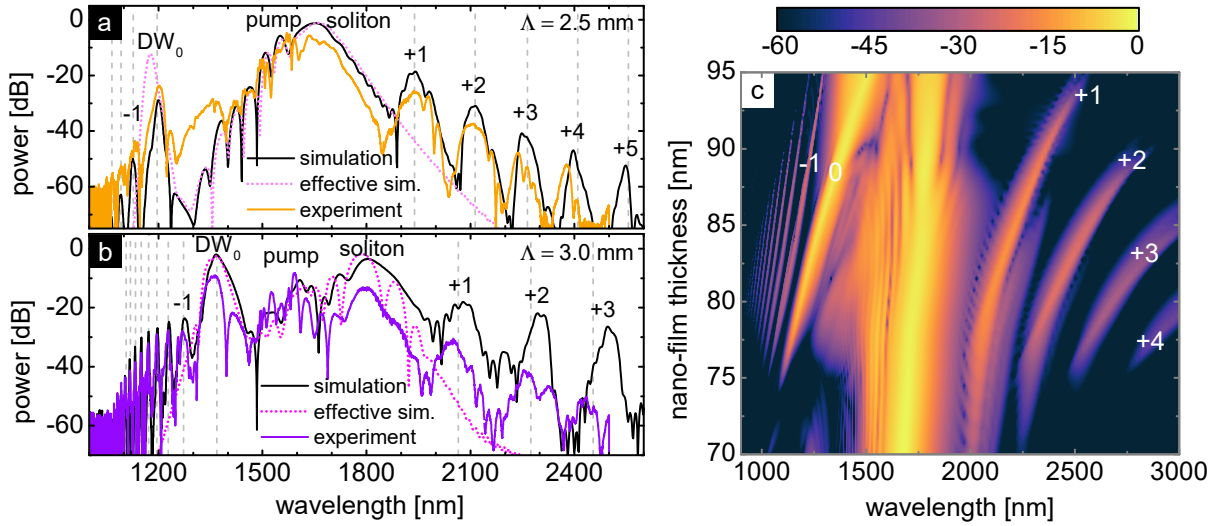

Figure 5.28: Experimental and simulated output spectra of fibers with period lengths of $\Lambda = 2.5$ mm (a, $t = 79.2$ nm) and $\Lambda = 3.0$ mm (b, $t = 89.7$ nm) at maximum input power. The black curves are simulations using the alternating dispersion and the pink dotted curves are simulations using the effective dispersion. Vertical dashed lines are phase-matching wavelengths calculated with Eq. 2.20 and the parameters of Table 5.4. (c) Simulated effect of the nano-film thickness on the output spectrum when using the fiber and laser parameters of Fig. 5.22 ($\Lambda = 1.409$ mm, $t = 0...85.5$ nm, $P = 11.8$ kW, color scale in dB).

it easier to be seeded by the edge of the soliton spectrum and proves the independence of QPM-DWs from conventional DWs.

The overall envelope of the long and short edge of the entire spectrum reaches its maximum at $t \approx 81$ nm for $\Lambda = 1.4$ mm (Fig. 5.28c), slightly shifting towards thicker layers for longer period lengths. When aiming to reach wavelengths that are spectrally far away from the pump, using nano-film thicknesses near that value is advantageous.

5.4.8 Influence of different filling fractions

One further free parameter of the nano-film geometry is the filling fraction *ff*, whose effect on the spectrum for different period lengths is presented in Fig. 5.29. The result closely resembles the study featuring different nano-film thicknesses as the DWs red-shift with increasing *ff*. A higher filling fraction modifies the integrated amount of GVD within one period, thus, changing the effective dispersion. For Eq. 3.32 it is non-significant how the GVD is distributed within one period, therefore, increasing *ff* or the nano-film thickness has the same effect in principle. One difference is the wavelength dependent dispersion associated with a specific nano-film thickness. Hence, although being able to result in the same GVD at one wavelength, different *ff* and t combinations will have unique dispersion landscapes.

All simulations of this study with different period lengths (Fig. 5.29b–d) have the same effective dispersion which could lead to the assumption that the core spectral region should

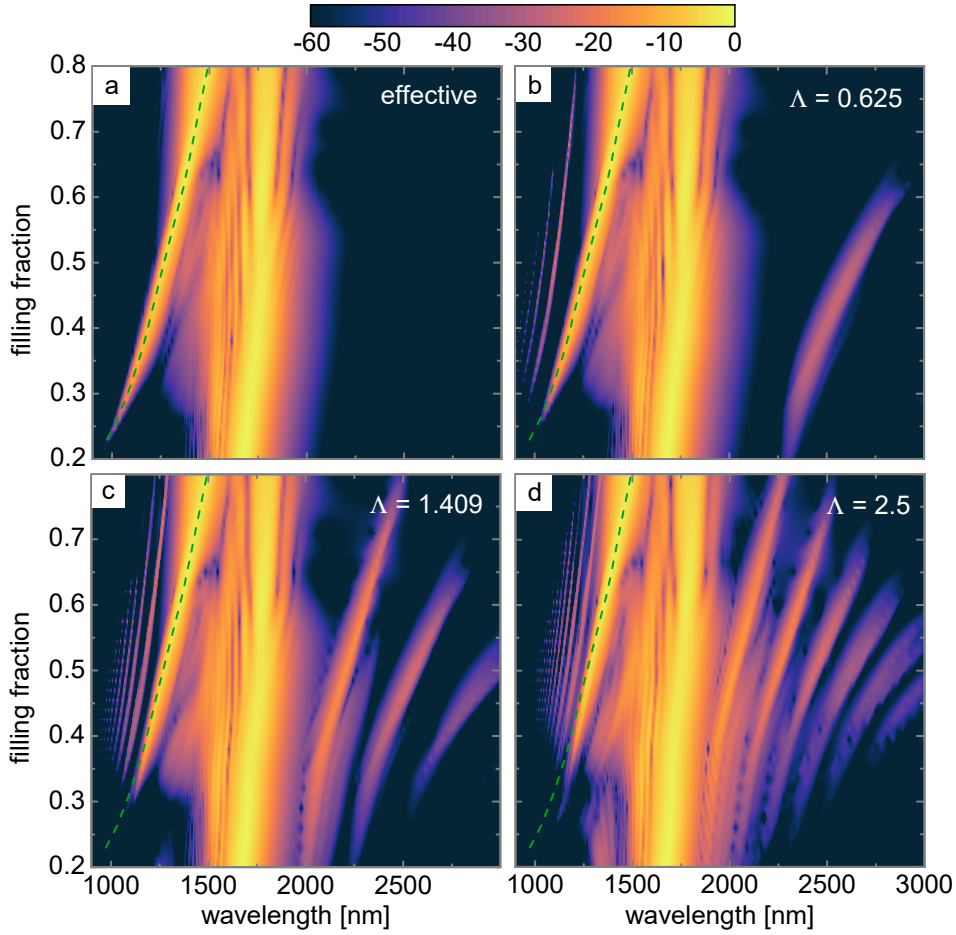

Figure 5.29: Simulation of the output spectra for different filling fractions for fiber and laser parameters used for Fig. 5.22 ($P = 11.8$ kW; $\lambda_p = 1570$ nm; loss: 10 dB/m; fiber length: 40 mm; $t = 0...85.5$ nm; color scale in dB). The common effective dispersion simulation (a) is compared to fibers with a period length of $\Lambda = 0.625$ mm (b), $\Lambda = 1.409$ mm (c), and $\Lambda = 2.5$ mm (d). The dashed line marks the DW_0 peak position of the effective dispersion simulation (a) throughout all panels.

be identical to the simulation using that effective dispersion (Fig. 5.29a). As discussed earlier, the effective dispersion approximation is valid for small period lengths compared to L_{NL}, being fulfilled for $\Lambda = 0.625$ mm (Fig. 5.29b), but deviating for longer ones. For the simulation with $\Lambda = 1.4$ mm (Fig. 5.29c), the core spectral region resembles the effective dispersion case only for $ff > 0.45$. Equivalently, it deviates if the DW_0 is located at too short wavelengths. This effect is even more pronounced for the simulation with $\Lambda = 2.5$ mm (Fig. 5.29d), moving the lower limit to $ff = 0.55$. The filling fraction resolved analysis reveals that the validity of the effective dispersion approximation is not only period length dependent, but also wavelength dependent. This can also be seen in the example of Fig. 5.28a, where the effective dispersion simulation matches well with the modulated dispersion simulation, except for the DW_0. Because L_{NL} decreases slightly with rising ff, the difference to the effective dispersion simulation cannot be entirely explained by the nonlinear length criterion, limiting its use for these fibers to $ff \approx 0.5$ only.

For the parameters of this simulation, $ff \approx 0.5$ gives the best results concerning total bandwidth and nonlinear conversion efficiency towards wavelength spectrally far away from λ_p.

5.4.9 Losses

In all simulations for periodically modulated ECFs presented so far the losses are assumed to be wavelength independent at 10 dB/m. Yet, the considerations in Section 5.3.6 reveal more realistic wavelength dependent losses. Especially the O-H group absorption, also present in silica, limits the low loss region of fibers towards the infrared and causes absorption beyond $\lambda = 2$ µm. Specifically for spectra with an extended spectral coverage of the QPM peaks towards the infrared, neglecting the IR absorption (Fig. A.5) causes all simulations to overestimate the spectral power density at the long-wavelength side compared to the experimentally measured spectra. Apart from material losses, the open fiber structure makes the fiber susceptible to pre and post coating contamination of the core's surface, adding additional scattering losses. Moreover, losses are expected to differ for the coated and uncoated fiber sections which can be averaged within the periods, yet, there are additional losses owing to the transitions between the sections. The step-wise change of the nano-film is directly connected to a shift of the electric field distribution of the fiber mode (Section 3.2), which is associated with optical losses. Samples with a short period length have more modal transitions within the same length and consequently their losses are higher (Fig. 5.30a). All samples produced have a total transmission that roughly follows an exponential fit considering their total amount of periods. The transmission includes additional common sources of losses for all samples such as scattering

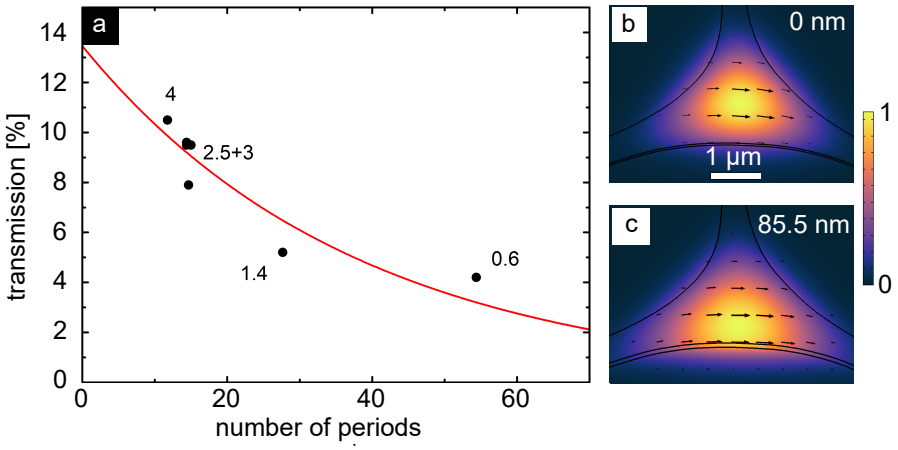

Figure 5.30: (a) Total transmission including coupling optics losses dependent on the total number of periods for all evaluated samples. The black data points are marked by their period lengths (in mm) and are fitted with an exponential curve. Normalized electric field distribution of the fundamental mode of the ECF without (b) and with (c) a Ta_2O_5 nano-film of thickness $t = 85.5$ nm.

losses, coupling losses, and losses of external lenses. Yet, the specifically fiber dependent losses dependent on the different fiber lengths, *ff* values, and nano-film thicknesses do not differ that much for all samples, making all losses not associated with the reflection losses at the mode transition vaguely comparable. Hence, the period number dependency following the Lambert-Beer law suggests a constant loss for each period. The fit concludes a transmission of 98.7 % per modal transition in experiments. Alternatively, the losses of the modal transitions can be calculated by the overlap integral of the electric fields E_i of the modes i = 1,2 (as used in Ref. 276), shown in Fig. 5.30b+c for λ = 1.6 µm.

$$\text{Transmission} = \frac{|\int E_1 E_2^* dA|^2}{\int |E_1|^2 dA \int |E_2|^2 dA} \tag{5.37}$$

The modal overlap of 85 % predicts higher losses in theory than estimated in experiments. This can be explained by the realistic smooth transition between the coated and uncoated fiber sections within a length of 60 µm (Section 5.4.1), leading to a more adiabatic change of the mode transition and reducing the losses.

5.4.10 Potential of QPM towards the IR

The limits in experiments using QPM-DW are set by the available fibers and the experimental hardware, first of all the laser source and the spectral detectors. However, hypothetical but realistic scenarios can be explored in simulations giving more insight into the potential of QPM for nonlinear frequency conversion. For instance, using more powerful lasers can expand the wavelength range of the output spectra. For spectra extending beyond $\lambda = 2.5$ µm the disregard of wavelengths dependent losses in the IR is no longer acceptable for silica based fibers. Therefore, while still avoiding including individual spectral absorption bands that are dependent on the type of silica glass used, in the following simulation, losses are approximated by a linear function in the logarithmically scaled imaginary part of the RI of silica collected by Kitamura et al.[277] $\text{Imag}(n) = -10^{0.001305\ \text{nm}^{-1}\lambda - 9.1122}$ (see Fig. A.5 in the appendix). This corresponds to losses of more than 4000 dB/m at $\lambda > 4.5$ µm. Furthermore, simulations including the extended long wavelengths lead to larger mode areas. For the simplification of finding the fundamental mode, the fiber cross section in the finite element simulations is only partially based on the real SEM image of the ECF (Fig. 4.1). Outside the central area, the three struts holding the fiber core are extended linearly while maintaining their dimension starting from the position where they are thinnest.

The first hypothetical scenario simulates launching a pulse with a pulse duration of 35 fs (FWHM) at a central wavelength of λ = 2 µm and a peak power of P = 70 kW into an ECF functionalized with a t = 70 nm thick Ta_2O_5 coating having a period length of Λ = 1.5 mm (Fig. 5.31). The adapted laser parameters enable the use of the second ZDW near λ_{ZD} = 2.7 µm for nonlinear frequency broadening, which was neglected in

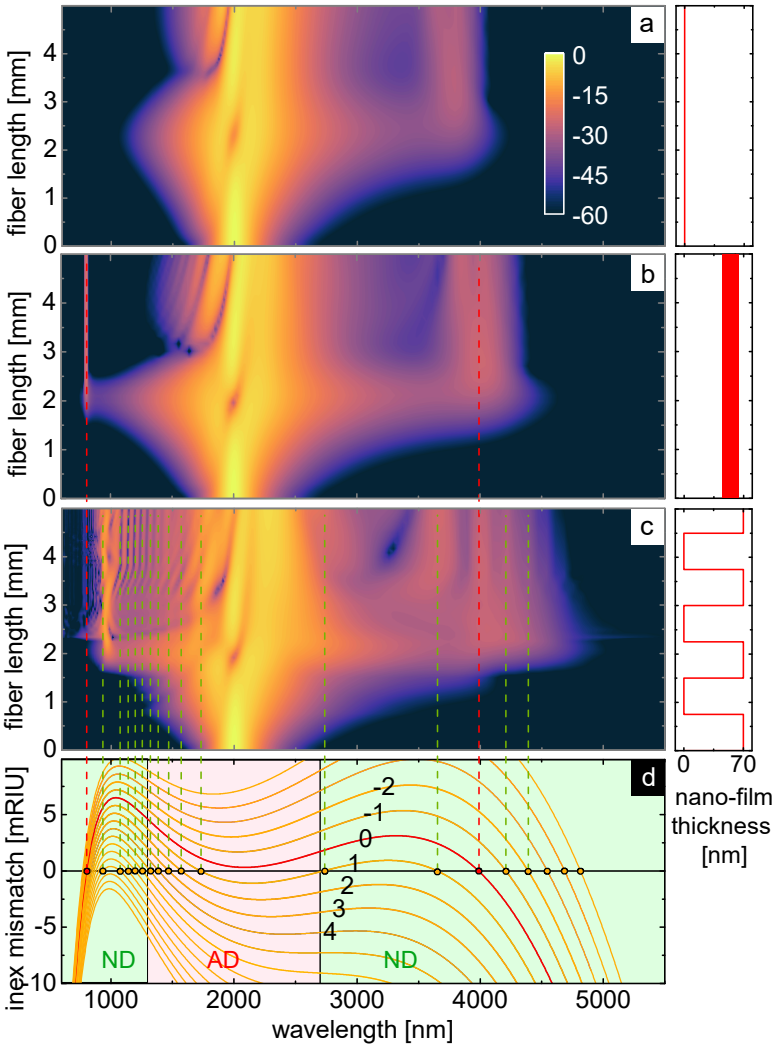

Figure 5.31: Spectral pulse propagation simulation of a laser with $\lambda_p = 2$ µm, $P = 70$ kW and a pulse duration (FWHM) of 35 fs in a 5 mm long ECF coated with a Ta_2O_5 nano-film of thickness $t = 70$ nm and a period length of $\Lambda = 1.5$ mm. Realistic losses are assumed as stated in the main text. To the right are the nano-film profiles: (a) uncoated, (b) coated, using the effective dispersion, and (c) coated, using the alternating dispersion. (d) Phase mismatch calculations based on Eq. 2.23 with $\lambda_s = 2.1$ µm. PM wavelengths are marked with dots and dashed lines and the red lines correspond to $q = 0$. Normal dispersive (ND) and anomalous dispersive (AD) domains are marked with light green and red backgrounds, respectively.

the previous simulations with a peak power of only 15 kW. Hence, the fiber dispersion changes from a single usable ZDW design to a dual ZDW case with ND domains at both sides of the spectrum (Fig. 5.31d). In contrast to using the realistic laser parameters, here, the uncoated fiber exhibits a DW_0 which is located at the long-wavelength side only (Fig. 5.31a). Yet, the short-wavelength DW_0 emerges at $\lambda = 802$ nm for a coated fiber and using the new effective dispersion (Fig. 5.31b). Despite the massively higher peak power, in combination with the stronger dispersion at the longer pump wavelength the soliton number is still low at $N_{sol} = 2.5$. Soliton fission leads to the formation of two peaks at the

long-wavelength side of the pump, but only a single high power soliton peak is observable in the temporal domain. There is a 700 nm wide spectral gap in between the isolated short-wavelength DW_0 and the next equally powerful spectral feature towards the pump wavelength, as anticipated for fibers with a constant nano-film thickness (Section 5.2).

Now applying the fully modulated dispersion in the simulations and enabling QPM ($\Lambda = 1.5$ mm), multiple peaks emerge both inside the above mentioned gap as well as on the long-wavelength side near the second DW_0. All peaks can be explained and verified by PM considerations using Eq. 2.23 and an assumed soliton wavelength of $\lambda_s = 2.1$ µm (Fig. 5.31c). Contrarily to the cases with experimentally realized laser parameters, here, additional PM wavelengths appear within the core spectral region defined by the spectral edges using the effective dispersion. On top of it, they can be found on both sides of the short-wavelength ZDW. This proves that QPM peaks are neither limited to the outer spectral regions as suggested by the experiments, nor influenced by the ZDW. The possibility to generate DWs both in the AD and in the ND domains of the fiber is a clear advantage compared to classical DW generation, being limited to the ND domain.

The amount of additional QPM peaks within the entire spectrum increases with longer period lengths. At a fixed period length, fibers with a strong dispersion exhibit more QPM peaks than dispersion flattened fibers, making QPM especially beneficial for fibers that are usually considered worse for classical SCG [278].

Despite including IR losses, the spectrum extends up to $\lambda = 4.5$ µm in a silica system. This is solely possible by using femtosecond pulses, keeping required fiber length for nonlinear frequency generation within a few millimeters. Thus, the total amount of periods within the entire fiber is less than four and only two of them fall within the QPM generating section. Although not experimentally verified, these length scales are easily realizable and suggest successful QPM generation with few nano-film thickness transitions, reducing the mode conversion losses. The feasibility of this idea considering optical damage of the front face and the nano-film at higher peak powers than the tested 15 kW requires further examination and is not part of this work.

In the second hypothetical scenario the pump wavelength is kept at $\lambda_p = 1570$ nm and only the peak power is increased to $P = 40$ kW compared to the real laser parameters. In contrast to the first scenario, losses are now assumed to be wavelength independent at 10 dB/m to be able to explore the potential towards the IR. Albeit unrealistic for silica based fibers, it gives insights into possibilities achievable by using other materials with less IR losses such as chalcogenides, fluorides, soft glasses, and liquids. Similar to the first scenario, the bare fiber exhibits a long-wavelength DW, but it is weaker due to the shortened λ_p. This is also the reason why the long-wavelength DW is located at even longer wavelengths ($\lambda_{DW_0} = 4.9$ µm, Fig. 5.32a) compared to the first scenario. When considering a Ta_2O_5 nano-film with a thickness of $t = 70$ nm and a period length of $\Lambda = 1$ mm, the short-wavelength DW appears at $\lambda = 937$ nm for the effective dispersion

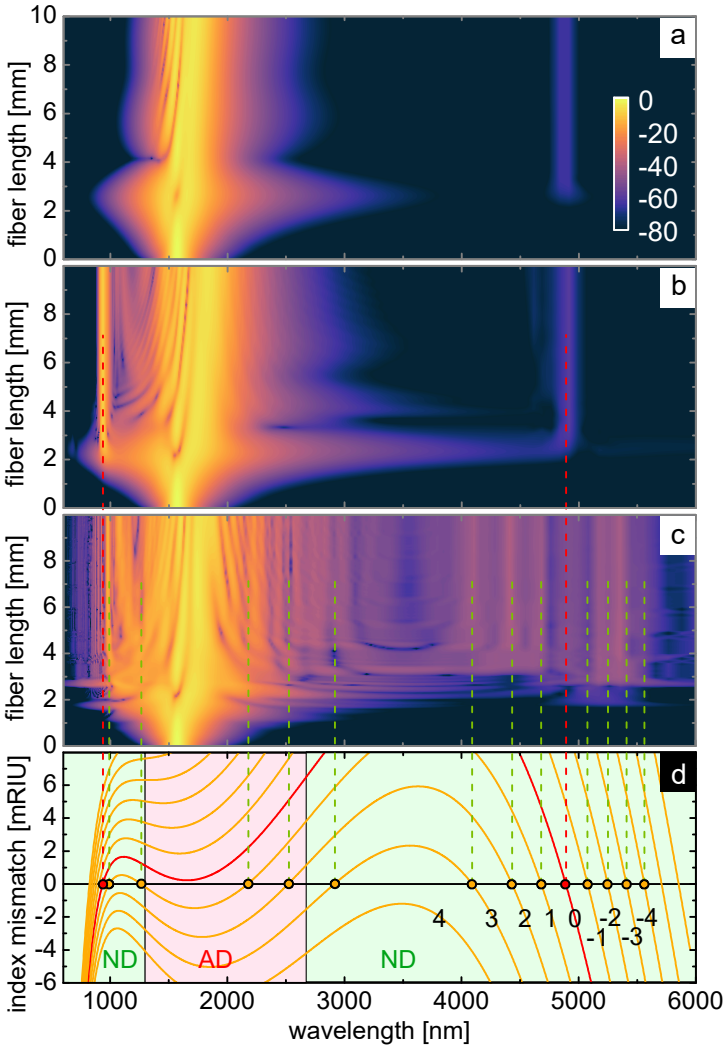

Figure 5.32: Spectral pulse propagation simulation of a laser with $\lambda_p = 1.57$ µm, $P = 40$ kW and a pulse duration (FWHM) of 35 fs in a 10 mm long ECF coated with a Ta_2O_5 nanofilm of thickness $t = 70$ nm, constant losses of 10 dB/m, and a period length of $\Lambda = 1$ mm ((a) uncoated ECF, (b) coated fiber, using the effective dispersion, and (c) coated ECF, using the alternating dispersion). (d) Phase mismatch calculations based on Eq. 2.23 with $\lambda_s = 1665$ nm. PM wavelengths are marked with dots and dashed lines and the red lines correspond to $q = 0$. Normal dispersive (ND) and anomalous dispersive domains (AD) are marked with light green and red backgrounds, respectively.

case (Fig. 5.32b). Using the real alternating dispersion (Fig. 5.32c) the additional QPM peaks near the second, long-wavelength DW_0 are notably stronger compared to the DW_0 of the effective dispersion (+20 dB) and the DW_0 of the alternating dispersion simulation itself. Hence, this proves the potential of strong conversion efficiencies towards QPM peaks in some cases, at least compared to classical DW generation. PM calculations (Eq. 2.23 with $\lambda_s = 1665$ nm, Fig. 5.32d) verify the spectral positions of the three peaks at the short-wavelength side of the second DW_0, but miss the ones on the long-wavelength side. Hence, this suggests that the effective dispersion approximation is not accurately replacing

the real alternating dispersion, as could have been suspected by comparing the nonlinear to the period length ($L_{\mathrm{NL}} = 0.9\ \mathrm{mm} < 1\ \mathrm{mm} = \Lambda$). Nonetheless, this scenario suggests the use of QPM to be an effective method for nonlinear frequency conversion in the mid-IR up to $\lambda = 5.6\ \mu\mathrm{m}$.

5.4.11 Discussion and conclusion

Multi-color light sources are the foundation for many modern optical applications in life science, metrology, and multimodal imaging in biophotonics. One promising approach for ultra-fast light generation in fibers featuring multiple user-defined spectral bands exploits multi-order DW formation from one soliton. The key is the usage of QPM, enabled by periodically modulating the fiber dispersion. The flexibility in nano-film thickness, period length, and filling fraction allows for tailoring the output spectrum to meet individual needs. Multiple high order DWs can be generated on both sides of the pump wavelength, reaching spectral domains partially inaccessible by conventional DW generation. Simulations reveal a great potential for nonlinear frequency conversion and SCG, ranging far in the IR. The additional spectral features all over the spectrum might be especially advantageous when having a high input power such that the new peaks themselves are capable of nonlinear interactions such as four wave mixing to further broaden and potentially flatten the spectrum. However, this is beyond the scope of this work.

Requiring period lengths in the mm scale with cm long fibers keeps the product compact and easy to handle and fabricate compared to hundreds of meter long diameter-oscillating fibers with meters of period length[67,73] and µm scale on-chip waveguides[71,279]. The concept of the dispersion mixing of the individual fiber sections leads to macro-scale effective media with an effective dispersion, whose validity in terms of nonlinear parameters is evaluated. As a quick estimation for $ff \approx 0.5$ the fiber should fulfill $L_{\mathrm{NL}} > \Lambda$. New possible dispersion landscapes enabled by the nano-film thickness modulation and not available with homogeneously coated ECFs open up novel methods for sensitive dispersion management for precisely shaping spectra or to design dispersion flattened fibers. The high pulse-to-pulse stability of the light source makes it desirable for scanning and single pulse applications while the wavelength of the QPM-DWs being robust to power modifications in combination with the variable spectral chirp is interesting for pump-probe experiments. On top of it, the overall sub-picosecond duration of the individual spectral features let this approach stand out and push the potential for novel light source designs for applications in sensing, spectroscopy and quantum technology.

5.5 Interplay of different effects

In the previous sections of Chapter 5 the effects of nano-films with uniform, gradually increasing or periodically modulated thickness were analyzed individually. In principle,

combining those effects is possible, which is tested in the following simulations as a brief outlook.

5.5.1 Nano-films with a chirped period length

One possibility is using height modulated Ta_2O_5 nano-films where the period length is gradually increasing along the fiber, as also considered by Langrock et al.[279] for periodically poled lithium niobate waveguides. In the example analyzed here, the period length ranges from $\Lambda = 0.5$ mm in the beginning of the fiber up to $\Lambda = 4.6$ mm, following the relation $\Lambda(N_\mathrm{p}) = 0.5\ \mathrm{mm} \cdot (1 + 0.0006 \cdot N_\mathrm{p}^3)$, with the consecutively numbered period N_p. Apart from a nearly constant section in the beginning that only covers the initial SPM broadening section before the soliton formation happens, the slope of the period length is almost linear at 0.12 mm/mm (green line in Fig. 5.33a). The resulting nano-film thickness distribution along the fiber with a maximum thickness of $t = 85.5$ nm is displayed in Fig. 5.33b.

When launching 50 fs pulses with a peak power of 10 kW and a central pump wavelength of $\lambda_p = 1570$ nm into the fiber, the simulated spectrum exhibits a multitude of peaks in the spectral area associated with QPM peak occurrence (Fig. 5.33c, green curve). At the onset of the QPM-DW peak creation along the fiber there are only a few peaks present as can be associated with the local period length. Further along the fiber more peaks emerge that fill up the outer regions of the spectrum on both the short and long-wavelength side. This high peak density can also be observed in ECFs with a constant and long period

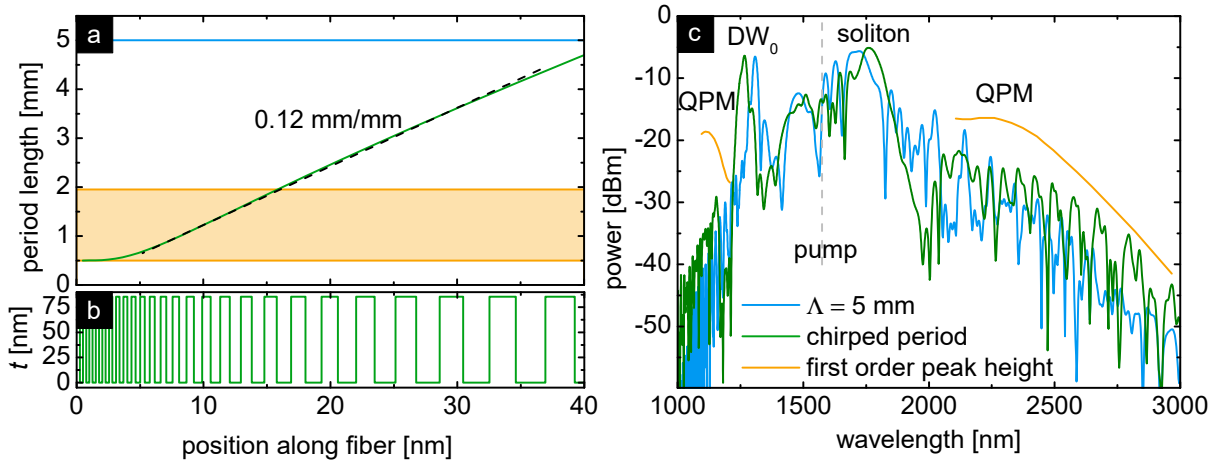

Figure 5.33: (a) Period length landscape of a fiber with a chirped period length (green) in contrast to fibers with a constant period length within the parameter range indicated by the orange area and the single blue line. (b) Actual Ta_2O_5 nano-film thickness distribution of the green curve in (a). (c) Output spectra of the fibers defined in (a). The orange line tracks the maximum of the positive and negative first order QPM peak for different period lengths. Pulse duration (FWHM): 50 fs, Peak power: 10 kW, pump wavelength: 1570 nm, nano-film thickness: $t_\mathrm{max} = 85.5$ nm, constant losses: 20 dB/m, filling fraction: $ff = 0.5$.

length such as $\Lambda = 5$ mm (blue curve). However, in spectral ranges further away from the pump on both sides of the spectrum ($\lambda > 2270$ nm and $\lambda < 1160$ nm), the conversion efficiency to the QPM peaks is up to 10 dB worse compared to the fiber with a chirped period length.

As a comparison, the peak maximum of the isolated first order QPM peaks of uniformly coated ECFs are tracked for different period length, also indicated by the yellow shaded area in Fig. 5.33a. They start in the outer regions of the spectrum far away from the pump for $\Lambda = 0.5$ mm and move towards the center for longer period lengths up to $\Lambda = 2$ mm. Although the conversion efficiency varies notably dependent on the period length of periodically modulated ECFs, it is higher than using chirped period configurations at all wavelengths. Thus, modulating the period length can generate denser QPM peaks, but the reduced fiber length of a locally constant period length limits the conversion efficiency to particular wavelengths. Because the effective dispersion does not depend on the period length (Eq. 3.32), the core spectrum resembles the ones of uniformly coated ECFs (Section 5.2).

5.5.2 Periodically structured nano-films with a thickness gradient

Another combination is using periodically modulated Ta_2O_5 nano-films with a constant period length, additionally having an overall gradually increasing thickness along the fiber. Because the effective dispersion depends on the position in the fiber, the core spectrum (ignoring QPM peaks) is similar to the ones for nano-films with a thickness gradient discussed in Section 5.3. Specifically, the soliton experiences a strong red-shift empowered by the co-moving effective short-wavelength ZDW (Fig. 5.34). Because the effective ZDW is under the influence of the dispersion of the uncoated fiber, it has a cut-off at 2.3 µm, which is at a slightly shorter wavelength compared to unmodulated nano-films. As discussed before, the shifting soliton generates multiple DW_0 at different wavelengths at several positions along the fiber, indicated by the white dotted line marked '0'. On top of it, the periodic modulation enables the creation of higher-order QPM-DWs. In contrast to Section 5.4, they are generated at different wavelengths along the fiber dependent on the local dispersion and soliton wavelength. The intra-order interference of the DWs created at different positions along the fiber leads to periodic spectral fringes, which can be seen best for the $q = +1$ DW. At the end of the fiber these fringes overlap with the Raman-shifted soliton for $\lambda > 2$ µm. With carefully choosing the right fiber parameters, this allows for a seamless connection of the core spectral region to the QPM peaks at the soliton side, which otherwise would exhibit a spectral gap (e.g. see Fig. 5.22). The spectral frequency of these fringes depends on the gradient strength, and increases for smaller gs. Close to the soliton the fringes are evenly distributed and become irregular at longer wavelengths when they also overlap with the fringes of the $q = +2$ DW. Reducing the period length

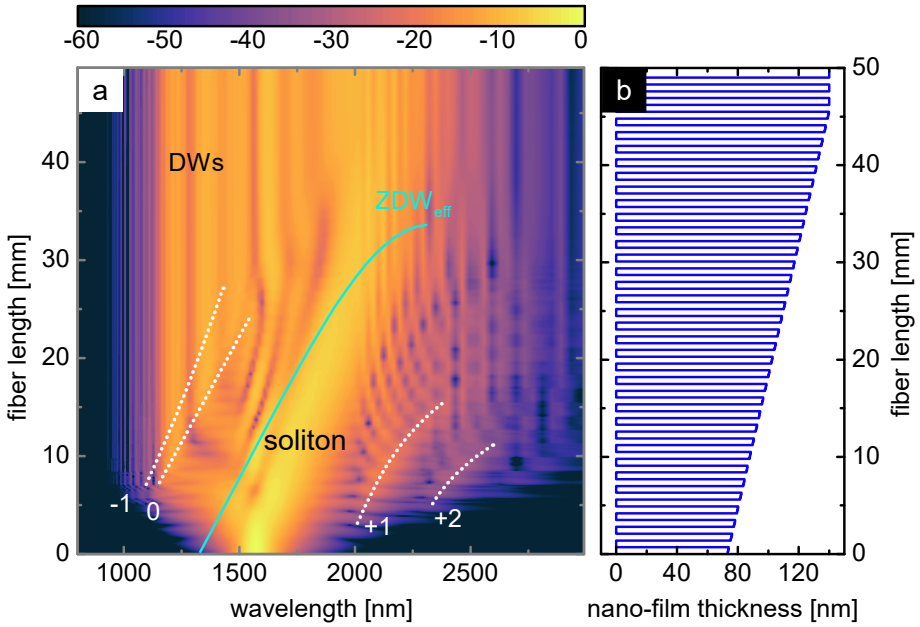

Figure 5.34: (a) Nonlinear pulse propagation simulation of a fiber with a periodically modulated Ta_2O_5 nano-film having an overall thickness gradient. The cyan line marks the short-wavelength ZDW of the effective dispersion with a cut-off at 2.3 µm. White dotted lines guide the eye to the positions of DWs, distinguished by their order q. The color scale is in dB. (b) Actual nano-film thickness distribution of the fiber used in (a). Pulse duration (FWHM): 35 fs, Peak power: 14 kW, pump wavelength: 1570 nm, period length $\Lambda = 1.4$ mm: $t = 85.5$ nm, constant losses: 10 dB/m, fiber length: 50 mm starting thickness: $t_s = 73$ nm, gradient strength: $gs = 1.46$ nm/mm, filling fraction: $ff = 0.5$.

can result in an isolated $q = +1$ DW, adding frequency comb-like features to the spectrum over a range of more than 500 nm in the IR.

On the short-wavelength side of the pump the fringes of the DWs with $q < 0$ have a smaller visibility and overlap with the DW_0s for $\lambda < 1.5$ µm. Because the fringes are connected to the creation of the QPM-DWs, there is a small area of unmodulated DW_0s in between the two white dotted lines for the zeroth and minus first order DW.

All in all combining gradient and periodical nano-film modifications unites features of both effects in one spectrum, enhancing the diverse possibilities to tailor nonlinear frequency conversion and to create unique SC sources.

6 | Conclusion

A suitable light source is a prerequisite for every optical application, with an ever increasing variation of demands for specific light properties. Among others, this includes coherent, ultrafast, and broadband sources with flat spectra or tailorable light in well-defined user controlled spectral bands for metrology, life sciences, biophotonics, and hyperspectral imaging. SCG in fibers is a promising technology for tunable light generation and the light properties heavily depend on the fiber parameters, especially their dispersion. Therefore, exploring new possibilities to modify the dispersion in fibers and shaping nonlinear frequency conversion is desired.

In this thesis, the key to precisely control the dispersion is the novel method of adding high RI nano-films to waveguides, inserting resonances in form of additional modes to the system. The nano-films are deposited directly on the core of ECFs conformally with ALD or non-conformally with direct current reactive magnetron sputtering. The nano-film modes form a modal anti-crossing with the fundamental mode of the fiber, predominantly impacting the waveguide dispersion part of the fiber dispersion. Increasing the thickness of the nano-films leads to a highly sensitive red-shifting of the ZDW towards the pump wavelength and beyond at a rate of 22.4 nm/nm and 17.3 nm/nm for TiO_2 and Ta_2O_5, respectively. In contrast to geometry and temperature tuning approaches, the short-wavelength ZDW of a two-ZDW system is affected primarily instead of the long wavelength one. Solely by adding the nano-films and appropriate positioning of the ZDW allows for the creation of solitons and the subsequent formation of DWs in silica based ECFs, which are otherwise ineffective concerning broadband nonlinear frequency conversion in the telecommunications regime using a low energy femtosecond pump at $\lambda_p = 1570$ nm.

Uniform conformal TiO_2 nano-films with thicknesses of only around $t = 50$ nm are sufficient to notably influence the dispersion of ECFs and the output spectrum of SCG. Specifically, tailoring the wavelength of a single and isolated DW over a large spectral range of 300 nm in the near-IR at a rate of 30 nm/nm is demonstrated. This enables tailorable light sources at specific frequency bands that cannot be reached with natural laser frequencies.

Introducing Ta_2O_5 nano-films with a gradually increase of the film thickness along the fiber via tilted sputtering deposition raises the degrees of freedom designing an optimized dispersion landscape in fibers. It allows for the creation of multiple DWs from the same soliton, filling up the spectrum owing to the longitudinally varying PM condition and leading to a more uniform spectral power density distribution. Spectrally flat light sources are e.g. required for high quality optical coherence tomography. The effect of the gradient strength and the starting thickness defining a linear-like gradient is investigated and

the spectra are evaluated using a suitable FoM. For example, at a gradient strength of $gs = 1.1$ nm/mm and $t_s = 50$ nm a 325 nm broad part of the spectrum with a standard deviation of the spectral power of $\sigma = 1.4$ dB could be realized. The in-fiber pulse energy of < 0.6 nJ is comparably small, avoiding the large powers required for additional nonlinear effects such as MI and high order soliton fission usually needed for flatter spectra in soliton-based SCG or in all-normal dispersive fibers. High quality light sources at low pump power enable portable devices for spectroscopy and metrology that can be used in-field. Furthermore, longitudinally varying the dispersion affects the soliton dynamics and can strengthen the Raman red-shift, resulting in an increase of the bandwidth towards the IR by 200 nm.

A further expansion of the bandwidth of SC is possible by periodically modulating the nano-film thickness. In this thesis, structured nano-films are manufactured by placing a precise laser-cut mask in direct contact to the outside of the fiber during sputtering deposition. Using period lengths of $\Lambda = 0.6$ mm to $\Lambda = 3.0$ mm in experiments enables QPM and causes the emergence of additional multi-color higher-order DWs on both sides of the pump wavelength beyond the reach of approaches using nano-films with uniform and gradually increasing thicknesses. These relatively narrow bands can be tailored to user-defined and mostly power-stable wavelengths by adapting the nano-film period length as well as designing the film thickness and filling fraction. In contrast to conventional DWs, QPM-DWs are not limited to the normal dispersive domain and can be generated all over the spectrum. With DWs in the AD domain, this opens the possibility for all-anomalous dispersive broadband nonlinear light sources without the need of a ZDW. The spectral shape in the core region and the PM considerations are based on the effective dispersion. This model of a filling fraction weighted averaging of the dispersion within one period length is valid for short period lengths that correlate with L_{NL} at first glance. Various simulations reveal the limits of the effective dispersion, which creates millimeter-size optical meta-materials. The effective dispersion is notably different from dispersions possible with uniformly coated fibers, thus resulting in novel dispersion landscapes and SC spectra even without the QPM-DWs.

Combining features of nano-films with gradually increasing thickness and periodical modulations adds fast modulated spectral features on top of broad and flat spectra, extending the spectral range without major spectral power density dips to the QPM-DWs in the IR.

The novel method of dispersion management via modal anti-crossing leads to light sources with unique properties and shifts the fabrication challenge from precise fiber drawing to nano-film deposition. Film deposition facilities are more widely available than fiber drawing towers and in combination with the handy sample and structure sizes it leads to a comparably easy, fast, and cost efficient fabrication technique. On top of it, the concept is analogously applicable to other high RI nano-film materials or other wave-

length ranges and can be straightforwardly extended to different fiber types and on-chip waveguides.

With the multitude of possibilities to shape nano-films on ECFs discussed in this work, resonance-driven dispersion engineering advances the field of researching novel nonlinear broadband light sources with tailored properties.

Outlook

Nonlinear effects aside, the nano-film functionalized ECFs exhibit modes with an enhanced light matter interaction overlap of tailorable evanescent fields that reach into the sideways easily accessable open groove. Filling the groove with solvents enables sensing of soluble biological samples and particles, investigations for photo-chemistry, or the study of materials with self-induced transparency.

Using the functionalized ECF as a nonlinear light source could benefit a multitude of applications, albeit partly only possible with further advancements in manufacturing and additional research.

With an improvement of the nano-film deposition technique, e.g. via a moving mask during deposition, the nano-film shape can be accurately controlled and is not longer bound to monotonously changing thicknesses. Thus, the dispersion of fibers can be designed to precisely follow and exploit the pulse dynamics along the fiber. Considering that the DW is controllable at every position of the fiber by an independent and individual locally adaptable nano-film thickness in principle, this allows to exactly shape the DW part of the output spectrum of SCG in ECFs. Thereby, the spectra with a uniform spectral density should be extendable to cover an even broader bandwidth. Using AI or machine learning could help to find the ideal nano-film shape for every desirable output spectrum.

All spectra are generated using an ultrafast laser with a pulse duration of 35 fs. Several considerations suggest that the QPM features and the DW_0 remain at a sub-picosecond time scale, implying the same for the spectra of continuously coated ECFs. The temporal separation of individual short-pulsed QPM-DWs could be used for pump-probe experiments. The individual pulses are not only tailorable in frequency, their relative delay can also be controlled with the fiber length. This makes a light source using functionalized ECFs interesting for ultrafast sensing, for example for electronic transitions in molecules and understanding light-activated local medical treatment.

Moreover, the short pulse duration keeps the nonlinear interactions at a small scale, allowing for short fibers and compact devices. This diminishes the influence of strong losses and thus extends the feasible bandwidth of silica-based systems towards the infrared up to $\lambda = 4.5$ µm as shown in simulations. This wavelength domain is interesting for sensing and spectroscopy as it covers the molecular fingerprint region. Yet, it might require further optimization of the nano-film's morphology and chemical composition to reduce avoidable losses.

The low pulse energy prevents the onset of MI and the fission of high order solitons, keeping the nonlinear broadening deterministic and leading to a high coherence along the entire spectrum. This is especially important for scanning and single pulse applications, e.g. using the dispersive Fourier transformation. Increasing the peak power and investigating the improved spectral broadening and soliton Raman shift behaviour while testing the limits to maintain good coherence is also of interest. In this context, verifying the coherence experimentally and measuring the damage threshold of the functionalized fibers might be advised.

As the nano-film thickness can modify the short-wavelength ZDW and temperature tuning approaches shift the long-wavelength ZDW, combining both effects in a hybrid fiber including liquids and nano-films could be innovative. It can be accomplished either by adding a liquid filled channel inside the core of an ECF or by adding a low RI liquid such as perflourononane in the groove of ECFs. Restricting the liquid to their respective area in a multi-hole, not spliceable, microstructured fiber and keeping the system of volatile liquids sealed requires advanced fiber engineering. Those fibers can potentially lead to individual tailoring of multiple ZDWs independently of each other. Being able to tune two DWs separately could enable f–2f interferometry for carrier envelope offset monitoring and stabilization at tailorable wavelengths.

The promising results of this work focusing on the novel concept of nano-film-based dispersion tuning lay the foundation for the instrumentalization of nonlinear light sources and further application oriented research.

References

1. Lühder, T. A. K. *et al.* Resonance-induced dispersion tuning for tailoring nonsolitonic radiation via nanofilms in exposed core fibers. *Laser Photonics Rev.* **14**, 1900418 (2020).
2. Lühder, T. A. K., Schneidewind, H., Schartner, E. P., Ebendorff-Heidepriem, H. & Schmidt, M. A. Longitudinally thickness-controlled nanofilms on exposed core fibres enabling spectrally flattened supercontinuum generation. *Light Adv. Manuf.* **2**, 21 (2021).
3. Lühder, T. A. K. *et al.* Tailored multi-color dispersive wave formation in quasi-phase-matched exposed core fibers. *Advanced Science* **9**, 2103864 (2022).
4. Maiman, T. H. Stimulated emission of radiation in ruby. *Nature* **187**, 493–494 (1960).
5. Kaiser, W. & Garrett, C. G. B. Two-photon excitation in CaF_2: Eu^{2+}. *Phys. Rev. Lett.* **7**, 229–231 (1961).
6. Franken, P. A., Hill, A. E., Peters, C. W. & Weinreich, G. Generation of optical harmonics. *Phys. Rev. Lett.* **7**, 118–119 (1961).
7. Goeppert-Mayer, M. Über Elementarakte mit zwei Quantensprungen. *Ann. Phys.* **9**, 273–295 (1931).
8. Shi, X. *et al.* Attosecond light science and its application for probing quantum materials. *J. Phys. B: At. Mol. Opt. Phys.* **53**, 184008 (2020).
9. Chang, D. E., Vuletić, V. & Lukin, M. D. Quantum nonlinear optics — photon by photon. *Nat. Photonics* **8**, 685–694 (2014).
10. Kaneda, F., Garay-Palmett, K., U'Ren, A. B. & Kwiat, P. G. Heralded single-photon source utilizing highly nondegenerate, spectrally factorable spontaneous parametric downconversion. *Opt. Express* **24**, 10733–10747 (2016).
11. Rota-Rodrigo, S. *et al.* Watt-level green random laser at 532 nm by SHG of a Yb-doped fiber laser. *Opt. Lett.* **43**, 4284–4287 (2018).
12. Warren-Smith, S. C. *et al.* Third harmonic generation in exposed-core microstructured optical fibers. *Opt. Express* **24**, 17860–17867 (2016).
13. Warren-Smith, S. C. *et al.* Nanofilm-induced spectral tuning of third harmonic generation. *Opt. Lett.* **42**, 1812–1815 (2017).
14. Beutler, M. *et al.* Difference-frequency generation of ultrashort pulses in the mid-IR using Yb-fiber pump systems and $AgGaSe_2$. *Opt. Express* **23**, 2730–2736 (2015).
15. Yang, K. *et al.* Polarization switch of four-wave mixing in a tunable fiber optical parametric oscillator. *Opt. Express* **26**, 2995–3003 (2018).
16. Demircan, A. & Bandelow, U. Supercontinuum generation by the modulation instability. *Opt. Commun.* **244**, 181–185 (2005).
17. Stolen, R. H. & Lin, C. Self-phase-modulation in silica optical fibers. *Phys. Rev. A* **17**, 1448–1453 (1978).
18. Agrawal, G. P. *Nonlinear Fiber Optics* (Academic Press, San Diego, 2006), 4 edn.
19. Doherty, B. *et al.* Plasmonic nanoparticle-functionalized exposed-core fiber; an optofluidic refractive index sensing platform. *Opt. Lett.* **42**, 4395–4398 (2017).
20. Edwards, P. S., Wyant, A. M., Brown, D. M., Liu, Z. & Philbrick, C. R. Supercontinuum laser sensing of atmospheric constituents. In Turner, M. D. & Kamerman, G. W. (eds.) *Laser Radar Technology and Applications XIV*, vol. 7323, 213 – 220. International Society for Optics and Photonics (SPIE, 2009).
21. Hult, J., Watt, R. S. & Kaminski, C. F. High bandwidth absorption spectroscopy with a dispersed supercontinuum source. *Opt. Express* **15**, 11385–11395 (2007).

22. Tu, H. & Boppart, S. A. Coherent fiber supercontinuum for biophotonics. *Laser Photonics Rev.* **7**, 628–645 (2013).
23. Jahromi, K. E. *et al.* Fourier transform and grating-based spectroscopy with a mid-infrared supercontinuum source for trace gas detection in fruit quality monitoring. *Opt. Express* **29**, 12381–12397 (2021).
24. Werblinski, T., Engel, S. R., Engelbrecht, R., Zigan, L. & Will, S. Temperature and multi-species measurements by supercontinuum absorption spectroscopy for ic engine applications. *Opt. Express* **21**, 13656–13667 (2013).
25. Wildanger, D., Rittweger, E., Kastrup, L. & Hell, S. W. STED microscopy with a supercontinuum laser source. *Opt. Express* **16**, 9614–9621 (2008).
26. Dupont, S. *et al.* IR microscopy utilizing intense supercontinuum light source. *Opt. Express* **20**, 4887–4892 (2012).
27. Moon, S. & Kim, D. Y. Ultra-high-speed optical coherence tomography with a stretched pulse supercontinuum source. *Opt. Express* **14**, 11575–11584 (2006).
28. Hosaka, Y. *et al.* Construction of nanosecond and picosecond pulse radiolysis system with supercontinuum probe. *Radiat. Phys. Chem.* **84**, 10–13 (2013).
29. Lin, Y. *et al.* Research of relative spectral responsivity calibration of InGaAs photodetector based on supercontinuum light source. In Han, S., Ehret, G. & Chen, B. (eds.) *Optical Metrology and Inspection for Industrial Applications VII*, vol. 11552, 295 – 300. International Society for Optics and Photonics (SPIE, 2020).
30. Udem, T., Holzwarth, R. & Hänsch, T. W. Optical frequency metrology. *Nature* **416**, 233–237 (2002).
31. Woodward, J. T. *et al.* Supercontinuum sources for metrology. *Metrologia* **46**, S277–S282 (2009).
32. Lee, J. H. *et al.* Experimental comparison of a kerr nonlinearity figure of merit including the stimulated brillouin scattering threshold for state-of-the-art nonlinear optical fibers. *Opt. Lett.* **30**, 1698–1700 (2005).
33. Liu, X.-L. *et al.* Broadband supercontinuum generation in air using tightly focused femtosecond laser pulses. *Opt. Lett.* **36**, 3900–3902 (2011).
34. Jang, D. G., Nam, I. H., Kim, M. S., Kang, K. & Suk, H. Generation of broadband supercontinuum light by double-focusing of a femtosecond laser pulse in air. *Appl. Phys. Lett.* **107**, 131105 (2015).
35. Rowlands, C. J. *et al.* Wide-field three-photon excitation in biological samples. *Light Sci. Appl.* **6**, e16255 (2017).
36. Dobryakov, A., Pérez Lustres, J., Kovalenko, S. & Ernsting, N. Femtosecond transient absorption with chirped pump and supercontinuum probe: Perturbative calculation of transient spectra with general lineshape functions, and simplifications. *Chem. Phys.* **347**, 127–138 (2008).
37. Reichardt, C. *et al.* Excited state dynamics of a photobiologically active Ru(II) dyad are altered in biologically relevant environments. *J. Phys. Chem. A* **121**, 5635–5644 (2017).
38. Lin, H. *et al.* 3.7 kW monolithic narrow linewidth single mode fiber laser through simultaneously suppressing nonlinear effects and mode instability. *Opt. Express* **27**, 9716–9724 (2019).
39. Kikuchi, K., Lorattanasane, C., Futami, F. & Kaneko, S. Observation of quasi-phase matched four-wave mixing assisted by periodic power variation in a long-distance optical amplifier chain. *IEEE Photonics Technol. Lett.* **7**, 1378–1380 (1995).
40. Chen, C.-M. & Kelley, P. L. Nonlinear pulse compression in optical fibers: scaling laws and numerical analysis. *J. Opt. Soc. Am. B* **19**, 1961–1967 (2002).
41. Islam, M. N. *Ultrafast Fiber Switching Devices and Systems* (AT&T, Cambridge, Australia, 1992).
42. Yasumoto, K. On a zig-zag ray picture in a planar waveguide. In Hung-Chia, H. & Snyder, A. W. (eds.) *Optical Waveguide Sciences*, 299–305 (Springer Netherlands, Dordrecht, 1983).

43. Petersen, C. R. *et al.* Mid-infrared supercontinuum covering the 1.4–13.3 µm molecular fingerprint region using ultra-high na chalcogenide step-index fibre. *Nat. Photonics* **8**, 830–834 (2014).
44. Grassani, D. *et al.* Mid infrared gas spectroscopy using efficient fiber laser driven photonic chip-based supercontinuum. *Nat. Commun.* **10**, 1553 (2019).
45. Peeters, J. *et al.* IR reflectography and active thermography on artworks: The added value of the 1.5–3 µm band. *Appl. Sci.* **8** (2018).
46. Zorin, I., Gattinger, P., Ebner, A. & Brandstetter, M. Advances in mid-infrared spectroscopy enabled by supercontinuum laser sources (2021).
47. Travers, J. C. Blue extension of optical fibre supercontinuum generation. *Journal of Optics* **12**, 113001 (2010).
48. You, Y.-J. *et al.* Ultrahigh-resolution optical coherence tomography at 1.3 µm central wavelength by using a supercontinuum source pumped by noise-like pulses. *Laser Phys. Lett.* **13**, 025101 (2015).
49. Urraca, R., Sanz-Garcia, A., Tardaguila, J. & Diago, M. P. Estimation of total soluble solids in grape berries using a hand-held NIR spectrometer under field conditions. *J. Sci. Food Agric.* **96**, 3007–3016 (2016).
50. Hernandez-Garcia, J. C. *et al.* Experimental study on a broad and flat supercontinuum spectrum generated through a system of two PCFs. *Laser Phys. Lett.* **10**, 075101 (2013).
51. Michalska, M., Mikolajczyk, J., Wojtas, J. & Swiderski, J. Mid-infrared, super-flat, supercontinuum generation covering the 2–5 µm spectral band using a fluoroindate fibre pumped with picosecond pulses. *Sci. Rep.* **6**, 39138 (2016).
52. Jin, A., Zhou, H., Zhou, X., Hou, J. & Jiang, Z. High-power ultraflat near-infrared supercontinuum generation pumped by a continuous amplified spontaneous emission source. *IEEE Photonics J.* **7**, 1600409 (2015).
53. Yin, K. *et al.* Ultrahigh-brightness, spectrally-flat, short-wave infrared supercontinuum source for long-range atmospheric applications. *Opt. Express* **24**, 20010–20020 (2016).
54. Eftekhar, M. A. *et al.* Accelerated nonlinear interactions in graded-index multimode fibers. *Nat. Commun.* **10**, 1638 (2019).
55. Demircan, A. & Bandelow, U. Analysis of the interplay between soliton fission and modulation instability in supercontinuum generation. *Appl. Phys. B* **86**, 31–39 (2007).
56. Solli, D. R., Herink, G., Jalali, B. & Ropers, C. Fluctuations and correlations in modulation instability. *Nat. Photonics* **6**, 463–468 (2012).
57. Goda, K. & Jalali, B. Dispersive fourier transformation for fast continuous single-shot measurements. *Nat. Photonics* **7**, 102–112 (2013).
58. Liao, J., Wang, Z., Huang, T., Wei, Q. & Li, D. Design of step-index-microstructured hybrid fiber for coherent supercontinuum generation. *Optik* **243**, 167393 (2021).
59. Guo, Y. *et al.* Generation of supercontinuum and frequency comb in a nitrobenzene-core photonic crystal fiber with all-normal dispersion profile. *Opt. Commun.* **481**, 126555 (2021).
60. Rao, D. S. S. *et al.* Ultra-low noise supercontinuum generation with flat-near zero all normal dispersion pure silica fiber at GHz reptition rate. In *Advanced Photonics 2018 (BGPP, IPR, NP, NOMA, Sensors, Networks, SPPCom, SOF)*, NpTh2I.7 (Optical Society of America, 2018).
61. Junaid, S. *et al.* Supercontinuum generation in a carbon disulfide core microstructured optical fiber. *Opt. Express* **29**, 19891–19902 (2021).
62. Kuyken, B., Billet, M., Leo, F., Yvind, K. & Pu, M. Octave-spanning coherent supercontinuum generation in an AlGaAs-on-insulator waveguide. *Opt. Lett.* **45**, 603–606 (2020).
63. Wei, J. *et al.* Supercontinuum generation assisted by wave trapping in dispersion-managed integrated silicon waveguides. *Phys. Rev. Applied* **14**, 054045 (2020).

64. Bartnick, M. *et al.* Cryogenic second-harmonic generation in periodically poled lithium niobate waveguides. *Phys. Rev. Applied* **15**, 024028 (2021).
65. Zhang, X. *et al.* Highly coherent light at 13 nm generated by use of quasi-phase-matched high-harmonic generation. *Opt. Lett.* **29**, 1357–1359 (2004).
66. Hickstein, D. D. *et al.* High-harmonic generation in periodically poled waveguides. *Optica* **4**, 1538–1544 (2017).
67. Droques, M., Kudlinski, A., Bouwmans, G., Martinelli, G. & Mussot, A. Dynamics of the modulation instability spectrum in optical fibers with oscillating dispersion. *Phys. Rev. A* **87**, 013813 (2013).
68. Driscoll, J. B. *et al.* Width-modulation of Si photonic wires for quasi-phase-matching of four-wave-mixing: experimental and theoretical demonstration. *Opt. Express* **20**, 9227–9242 (2012).
69. Lefevre, Y., Vermeulen, N. & Thienpont, H. Quasi-phase-matching of four-wave-mixing-based wavelength conversion by phase-mismatch switching. *J. Lightwave Technol.* **31**, 2113–2121 (2013).
70. Koester, H. J., Baur, D., Uhl, R. & Hell, S. W. Ca^{2+} fluorescence imaging with pico- and femtosecond two-photon excitation: Signal and photodamage. *Biophys. J.* **77**, 2226–2236 (1999).
71. Hickstein, D. D. *et al.* Quasi-phase-matched supercontinuum generation in photonic waveguides. *Phys. Rev. Lett.* **120**, 053903 (2018).
72. Phillips, C. R. *et al.* Supercontinuum generation in quasi-phasematched waveguides. *Opt. Express* **19**, 18754–18773 (2011).
73. Conforti, M., Trillo, S., Mussot, A. & Kudlinski, A. Parametric excitation of multiple resonant radiations from localized wavepackets. *Sci. Rep.* **5**, 9433 (2015).
74. Chemnitz, M. *et al.* Thermodynamic control of soliton dynamics in liquid-core fibers. *Optica* **5**, 695–703 (2018).
75. Russell, P. S. J., Hölzer, P., Chang, W., Abdolvand, A. & Travers, J. C. Hollow-core photonic crystal fibres for gas-based nonlinear optics. *Nat. Photonics* **8**, 278–286 (2014).
76. Sollapur, R. *et al.* Resonance-enhanced multi-octave supercontinuum generation in antiresonant hollow-core fibers. *Light Sci. Appl.* **6**, e17124–e17124 (2017).
77. Roberts, A. S. *et al.* Ultra-thin titanium nitride films for refractory spectral selectivity. *Opt. Mater. Express* **8**, 3717–3728 (2018).
78. Droques, M., Kudlinski, A., Bouwmans, G., Martinelli, G. & Mussot, A. Experimental demonstration of modulation instability in an optical fiber with a periodic dispersion landscape. *Opt. Lett.* **37**, 4832–4834 (2012).
79. Lühder, T., Plentz, J., Kobelke, J., Wondraczek, K. & Schmidt, M. A. All-fiber integrated in-line semiconductor photoconductor. *J. Lightwave Technol.* **37**, 3244–3251 (2019).
80. Verhoef, A. *et al.* Ytterbium fiber system using a dispersion compensating fiber stretcher. In *CLEO/Europe and EQEC 2011 Conference Digest*, CJ4_2 (Optical Society of America, 2011).
81. Heuermann, T., Gaida, C., Gebhardt, M. & Limpert, J. Thulium-doped nonlinear fiber amplifier delivering 50 fs pulses at 20 W of average power. *Opt. Lett.* **43**, 4441–4444 (2018).
82. ne, J. C. *et al.* Multi-core fiber integrated multi-port beam splitters for quantum information processing. *Optica* **7**, 542–550 (2020).
83. Pitilakis, A. K., Zografopoulos, D. C. & Kriezis, E. E. In-line polarization controller based on liquid-crystal photonic crystal fibers. *J. Lightwave Technol.* **29**, 2560–2569 (2011).
84. Bahaa E. A. Saleh, M. C. T. *Fundamentals of Photonics* (John Wiley & Sons, New York, USA, 1991).
85. Snyder, A. & Love, J. D. *Optical Waveguide Theory* (Chapman and Hall, New York, U.S.A., 1983).
86. Malitson, I. H. Interspecimen comparison of the refractive index of fused silica∗,†. *J. Opt. Soc. Am.* **55**, 1205–1209 (1965).

87. Zeisberger, M., Hartung, A. & Schmidt, M. A. Understanding dispersion of revolver-type anti-resonant hollow core fibers. *Fibers* **6** (2018).
88. Osório, J. H. *et al.* Tailoring modal properties of inhibited-coupling guiding fibers by cladding modification. *Sci. Rep.* **9**, 1376 (2019).
89. Li, G., Zeisberger, M. & Schmidt, M. A. Guiding light in a water core all-solid cladding photonic band gap fiber; an innovative platform for fiber-based optofluidics. *Opt. Express* **25**, 22467–22479 (2017).
90. Rahman, M. Z. & Islam, M. S. Effect of chromatic dispersion on four-wave mixing in WDM optical transmission system. *J. Media Commun. Stud.* **3**, 323 – 330 (2011).
91. Roy, S., Bhadra, S. K. & Agrawal, G. P. Dispersive waves emitted by solitons perturbed by third-order dispersion inside optical fibers. *Phys. Rev. A* **79**, 023824 (2009).
92. Akhmediev, N. & Karlsson, M. Cherenkov radiation emitted by solitons in optical fibers. *Phys. Rev. A* **51**, 2602–2607 (1995).
93. Marcuse, D. Interdependence of waveguide and material dispersion. *Appl. Opt.* **18**, 2930–2932 (1979).
94. W.A. Gambling, C. R., H. Matsumura. Mode dispersion, material dispersion and profile dispersion in graded-index single-mode fibres. *IEE J. microw. opt. acoust.* **3**, 239–246 (1979).
95. Zhang, D., Sheng, Q. & Dong, X. Analysis of the error of chromatic dispersion when using approximation of material dispersion plus waveguide dispersion in photonic crystal fibers. In Li, M.-J., Chen, J., Kawanishi, S. & White, I. H. (eds.) *Passive Components and Fiber-based Devices IV*, vol. 6781, 1052 – 1056. International Society for Optics and Photonics (SPIE, 2007).
96. Stark, S. P., Biancalana, F., Podlipensky, A. & St. J.Russell, P. Nonlinear wavelength conversion in photonic crystal fibers with three zero-dispersion points. *Phys. Rev. A* **83**, 023808 (2011).
97. Zhang, L. *et al.* Silicon waveguide with four zero-dispersion wavelengths and its application in on-chip octave-spanning supercontinuum generation. *Opt. Express* **20**, 1685–1690 (2012).
98. Fatema, S., Mia, M. B. & Kim, S. Multiple mode couplings in a waveguide array for broadband near-zero dispersion and supercontinuum generation. *J. Lightwave Technol.* **39**, 216–222 (2021).
99. Riesen, N., Zhang, W. Q. & Monro, T. M. Dispersion in silica microbubble resonators. *Opt. Lett.* **41**, 1257–1260 (2016).
100. Ghosh, D., Roy, S. & Bhadra, S. K. Efficient supercontinuum sources based on suspended core microstructured fibers. *IEEE J. Sel. Top. Quantum Electron.* **20**, 597–604 (2014).
101. Han, X. *et al.* Mid-infrared supercontinuum generation in a three-hole Ge20Sb15Se65 chalcogenide suspended-core fiber. *Opt. Fiber Technol.* **34**, 74–79 (2017).
102. Granzow, N. *et al.* Supercontinuum generation in chalcogenide-silica step-index fibers. *Opt. Express* **19**, 21003–21010 (2011).
103. Sakr, H., Hussein, R. A., Hameed, M. F. O. & Obayya, S. Analysis of photonic crystal fiber with silicon core for efficient supercontinuum generation. *Optik* **182**, 848–857 (2019).
104. Peacock, A. C. *et al.* Wavelength conversion and supercontinuum generation in silicon optical fibers. *IEEE J. Sel. Top. Quantum Electron.* **24**, 5100309 (2018).
105. Ordu, M. & Basu, S. N. Recent progress in germanium-core optical fibers for mid-infrared optics. *Infrared Phys. Technol.* **111**, 103507 (2020).
106. Bozolan, A., de Matos, C. J. S., Cordeiro, C. M. B., dos Santos, E. M. & Travers, J. Supercontinuum generation in a water-core photonic crystal fiber. *Opt. Express* **16**, 9671–9676 (2008).
107. Xuan, K. D. *et al.* Dispersion characteristics of a suspended-core optical fiber infiltrated with water. *Appl. Opt.* **56**, 1012–1019 (2017).
108. Norwood, R. A. Liquid core optical fiber for nonlinear frequency generation. In *Laser Congress 2017 (ASSL, LAC)*, ATu5A.1 (Optical Society of America, 2017).

109. Ermolov, A., Mak, K. F., Frosz, M. H., Travers, J. C. & Russell, P. S. J. Supercontinuum generation in the vacuum ultraviolet through dispersive-wave and soliton-plasma interaction in a noble-gas-filled hollow-core photonic crystal fiber. *Phys. Rev. A* **92**, 033821 (2015).
110. Conti, C., Schmidt, M. A., Russell, P. S. J. & Biancalana, F. Highly noninstantaneous solitons in liquid-core photonic crystal fibers. *Phys. Rev. Lett.* **105**, 263902 (2010).
111. Raja, R. V. J., Husakou, A., Hermann, J. & Porsezian, K. Supercontinuum generation in liquid-filled photonic crystal fiber with slow nonlinear response. *J. Opt. Soc. Am. B* **27**, 1763–1768 (2010).
112. Dai, F., Xu, Y. & Chen, X. Enhanced and broadened SRS spectra of toluene mixed with chloroform in liquid-core fiber. *Opt. Express* **17**, 19882–19886 (2009).
113. Hasan, M. M., Kumar, D. S., Mahdy, M., Hasan, D. N. & Matin, M. Robust optical fiber using single negative metamaterial cladding. *IEEE Photonics Technol. Lett.* **25**, 1043–1046 (2013).
114. Belli, F., Abdolvand, A., Chang, W., Travers, J. C. & Russell, P. S. Vacuum-ultraviolet to infrared supercontinuum in hydrogen-filled photonic crystal fiber. *Optica* **2**, 292–300 (2015).
115. Monfared, Y. E. & Ponomarenko, S. A. Extremely nonlinear carbon-disulfide-filled photonic crystal fiber with controllable dispersion. *Opt. Mater.* **88**, 406–411 (2019).
116. Haakestad, M. *et al.* Electrically tunable photonic bandgap guidance in a liquid-crystal-filled photonic crystal fiber. *IEEE Photonics Technol. Lett.* **17**, 819–821 (2005).
117. Meng, F. *et al.* Controllable two-color dispersive wave generation in argon-filled hypocycloid-core kagome fiber. *Opt. Express* **25**, 32972–32984 (2017).
118. Novoa, D., Cassataro, M., Travers, J. C. & Russell, P. S. J. Photoionization-induced emission of tunable few-cycle midinfrared dispersive waves in gas-filled hollow-core photonic crystal fibers. *Phys. Rev. Lett.* **115**, 033901 (2015).
119. Tarnowski, K. *et al.* Nonlinear frequency conversion in a birefringent microstructured fiber tuned by externally applied hydrostatic pressure. *Opt. Lett.* **38**, 5260–5263 (2013).
120. Martin-Lopez, S. *et al.* Temperature effects on supercontinuum generation using a continuous-wave raman fiber laser. *Opt. Commun.* **267**, 193–196 (2006).
121. Wang, C. *et al.* Effect of temperature on supercontinuum generation in CS_2-core optical fiber. *IEEE Photonics J.* **10**, 1400211 (2018).
122. Köttig, F. *et al.* Mid-infrared dispersive wave generation in gas-filled photonic crystal fibre by transient ionization-driven changes in dispersion. *Nat. Commun.* **8**, 813 (2017).
123. Im, S.-J., Husakou, A. & Herrmann, J. High-power soliton-induced supercontinuum generation and tunable sub-10-fs VUV pulses from kagome-lattice HC-PCFs. *Opt. Express* **18**, 5367–5374 (2010).
124. Wang, A. *et al.* Visible supercontinuum generation with sub-nanosecond 532-nm pulses in all-solid photonic bandgap fiber. *IEEE Photonics Technol. Lett.* **24**, 143–145 (2012).
125. Shavrin, I., Novotny, S. & Ludvigsen, H. Mode excitation and supercontinuum generation in a few-mode suspended-core fiber. *Opt. Express* **21**, 32141–32150 (2013).
126. Scheibinger, R. *et al.* Higher-order mode supercontinuum generation in dispersion-engineered liquid-core fibers. *Sci. Rep.* **11**, 5270 (2021).
127. Diemer, S. *et al.* Liquid-core light guides for near-infrared applications. *Appl. Opt.* **36**, 9075–9082 (1997).
128. Mandon, J., Sorokin, E., Sorokina, I. T., Guelachvili, G. & Picqué, N. Supercontinua for high-resolution absorption multiplex infrared spectroscopy. *Opt. Lett.* **33**, 285–287 (2008).
129. Kato, T., Suetsugu, Y., Takagi, M., Sasaoka, E. & Nishimura, M. Measurement of the nonlinear refractive index in optical fiber by the cross-phase-modulation method with depolarized pump light. *Opt. Lett.* **20**, 988–990 (1995).
130. Granzow, N. *Microstructured Optical Fibers with Incorporated Nonlinear Glasses.* Ph.D. thesis, Friedrich-Alexander-Universität Erlangen-Nürnberg, Germany (2013).

131. Evans, C. C. *Nonlinear optics in titanium dioxide: from bulk to integrated optical devices.* Ph.D. thesis, Harvard University, Cambridge, MA, USA (2013).
132. Jung, H. *et al.* Kerr solitons with tantala ring resonators. In *Nonlinear Optics (NLO)*, NW2A.3 (Optical Society of America, 2019).
133. Foster, M. A., Moll, K. D. & Gaeta, A. L. Optimal waveguide dimensions for nonlinear interactions. *Opt. Express* **12**, 2880–2887 (2004).
134. Steel, M. J. Reflection symmetry and mode transversality in microstructured fibers. *Opt. Express* **12**, 1497–1509 (2004).
135. V., S. A. & Monro, T. M. A full vectorial model for pulse propagation in emerging waveguides with subwavelength structures part I: Kerr nonlinearity. *Opt. Express* **17**, 2298–2318 (2009).
136. DeMartini, F., Townes, C. H., Gustafson, T. K. & Kelley, P. L. Self-steepening of light pulses. *Phys. Rev.* **164**, 312–323 (1967).
137. Tomlinson, W. J., Stolen, R. H. & Johnson, A. M. Optical wave breaking of pulses in nonlinear optical fibers. *Opt. Lett.* **10**, 457–459 (1985).
138. Allen, J. E. The early history of solitons (solitary waves). *Phys. Scr.* **57**, 436–441 (1998).
139. Dudley, J. M., Genty, G. & Coen, S. Supercontinuum generation in photonic crystal fiber. *Rev. Mod. Phys.* **78**, 1135–1184 (2006).
140. Ciret, C. *et al.* Physical origin of higher-order soliton fission in nanophotonic semiconductor waveguides. *Sci. Rep.* **8**, 17177 (2018).
141. Wai, P. K. A., Menyuk, C. R., Lee, Y. C. & Chen, H. H. Nonlinear pulse propagation in the neighborhood of the zero-dispersion wavelength of monomode optical fibers. *Opt. Lett.* **11**, 464–466 (1986).
142. Yin, L., Lin, Q. & Agrawal, G. P. Soliton fission and supercontinuum generation in silicon waveguides. *Opt. Lett.* **32**, 391–393 (2007).
143. Herrmann, J. *et al.* Experimental evidence for supercontinuum generation by fission of higher-order solitons in photonic fibers. *Phys. Rev. Lett.* **88**, 173901 (2002).
144. Jalali, B., Raghunathan, V., Dimitropoulos, D. & Boyraz, O. Raman-based silicon photonics. *IEEE Journal of Selected Topics in Quantum Electronics* **12**, 412–421 (2006).
145. Vanholsbeeck, F., Emplit, P. & Coen, S. Complete experimental characterization of the influence of parametric four-wave mixing on stimulated raman gain. *Opt. Lett.* **28**, 1960–1962 (2003).
146. Gordon, J. P. Theory of the soliton self-frequency shift. *Opt. Lett.* **11**, 662–664 (1986).
147. Atieh, A. K., Myslinski, P., Chrostowski, J. & Galko, P. Measuring the raman time constant (T_r) for soliton pulses in standard single-mode fiber. *J. Lightwave Technol.* **17**, 216 (1999).
148. Chen, Z., Taylor, A. J. & Efimov, A. Soliton dynamics in non-uniform fiber tapers: analytical description through an improved moment method. *J. Opt. Soc. Am. B* **27**, 1022–1030 (2010).
149. Kormokar, R., Shamim, M. H. M. & Rochette, M. High-order analytical formulation of soliton self-frequency shift. *J. Opt. Soc. Am. B* **38**, 466–475 (2021).
150. Cristiani, I., Tediosi, R., Tartara, L. & Degiorgio, V. Dispersive wave generation by solitons in microstructured optical fibers. *Opt. Express* **12**, 124–135 (2004).
151. Bendahmane, A. *et al.* Seeded intermodal four-wave mixing in a highly multimode fiber. *J. Opt. Soc. Am. B* **35**, 295–301 (2018).
152. Yang, C. C. & Wang, A. J. S. Cross-polarization cross-phase modulation of femtosecond pulses in erbium-doped fiber amplifiers. *J. Opt. Soc. Am. B* **9**, 682–686 (1992).
153. Wang, W., Yang, H., Tang, P., Zhao, C. & Gao, J. Soliton trapping of dispersive waves in photonic crystal fiber with two zero dispersive wavelengths. *Opt. Express* **21**, 11215–11226 (2013).
154. Warren-Smith, S. C. *et al.* Tunable multi-wavelength third-harmonic generation using exposed-core microstructured optical fiber. *Opt. Lett.* **44**, 626–629 (2019).

155. Allayarov, I., Schmidt, M. A. & Weiss, T. Theory of four-wave mixing for bound and leaky modes. *Phys. Rev. A* **101**, 043806 (2020).
156. Travers, J. C., Frosz, M. H. & Dudley, J. M. *Supercontinuum Generation in Optical Fibers* (Cambridge University Press, Cambridge, 2010).
157. Xia, C. *et al.* Supercontinuum generation in silica fibers by amplified nanosecond laser diode pulses. *IEEE J. Sel. Top. Quantum Electron.* **13**, 789–797 (2007).
158. Couairon, A. *et al.* Practitioner's guide to laser pulse propagation models and simulation. *Eur. Phys. J.: Spec. Top.* **199**, 5–76 (2011).
159. Stolen, R. H., Gordon, J. P., Tomlinson, W. J. & Haus, H. A. Raman response function of silica-core fibers. *J. Opt. Soc. Am. B* **6**, 1159–1166 (1989).
160. Karasawa, N. *et al.* Comparison between theory and experiment of nonlinear propagation for a-few-cycle and ultrabroadband optical pulses in a fused-silica fiber. *IEEE J. Quantum Electron.* **37**, 398–404 (2001).
161. Trebino, R. *et al.* Measuring ultrashort laser pulses in the time-frequency domain using frequency-resolved optical gating. *Rev. Sci. Instrum.* **68**, 3277–3295 (1997).
162. Xu, L., Zeek, E. & Trebino, R. Simulations of frequency-resolved optical gating for measuring very complex pulses. *J. Opt. Soc. Am. B* **25**, A70–A80 (2008).
163. Klenner, A. *et al.* Gigahertz frequency comb offset stabilization based on supercontinuum generation in silicon nitride waveguides. *Opt. Express* **24**, 11043–11053 (2016).
164. Bellini, M. & Hänsch, T. W. Phase-locked white-light continuum pulses: toward a universal optical frequency-comb synthesizer. *Opt. Lett.* **25**, 1049–1051 (2000).
165. Frosz, M. H. Validation of input-noise model for simulations of supercontinuum generation and rogue waves. *Opt. Express* **18**, 14778–14787 (2010).
166. Dudley, J. M. & Coen, S. Coherence properties of supercontinuum spectra generated in photonic crystal and tapered optical fibers. *Opt. Lett.* **27**, 1180–1182 (2002).
167. Genty, G., Surakka, M., Turunen, J. & Friberg, A. T. Complete characterization of supercontinuum coherence. *J. Opt. Soc. Am. B* **28**, 2301–2309 (2011).
168. Gonzalez-Valencia, E., Villar, I. D. & Torres, P. Novel bloch wave excitation platform based on few-layer photonic crystal deposited on d-shaped optical fiber. *Sci. Rep.* **11**, 11266 (2021).
169. Anishchik, S. & Ivanov, K. A method for simulating level anti-crossing spectra of diamond crystals containing nv^- color centers. *J. Magn. Reson.* **305**, 67–76 (2019).
170. Chen, S., Zhang, W., Yang, B., Wu, T. & Zhang, X. Tailoring exceptional points with one-dimensional graphene-embedded photonic crystals. *Sci. Rep.* **9**, 5551 (2019).
171. Okamoto, K. *Fundamentals of optical waveguides* (Academic Press, Burlingtin, MA, USA, 2006), 2 edn.
172. Smith, N. J. & Doran, N. J. Modulational instabilities in fibers with periodic dispersion management. *Opt. Lett.* **21**, 570–572 (1996).
173. Luo, D. *et al.* Influence of source and drain contacts on the properties of indium–gallium–zinc-oxide thin-film transistors based on amorphous carbon nanofilm as barrier layer. *ACS Appl. Mater. Interfaces* **7**, 3633–3640 (2015).
174. Lee, S. H., Kim, J. W., Lee, T. I. & Myoung, J. M. Inorganic nano light-emitting transistor: p-type porous silicon nanowire/n-type ZnO nanofilm. *Small* **12**, 4222–4228 (2016).
175. Hartsough, L. D. & McLeod, P. S. High-rate sputtering of enhanced aluminum mirrors. *J. Vac. Sci. Technol.* **14**, 123–126 (1977).
176. Pierro, V. *et al.* On the performance limits of coatings for gravitational wave detectors made of alternating layers of two materials. *Opt. Mater.* **96**, 109269 (2019).

177. Ghazaryan, L. *et al.* On the properties of nanoporous SiO_2 films for single layer antireflection coating. *Adv. Eng. Mater.* **21**, 1801229 (2019).
178. Sikder, U. & Zaman, M. A. Optimization of multilayer antireflection coating for photovoltaic applications. *Opt. Laser Technol.* **79**, 88–94 (2016).
179. Zheng, J., Zhou, C., Feng, J., Cao, H. & Lu, P. A metal-mirror-based reflecting polarizing beam splitter. *J. Opt. A: Pure Appl. Opt.* **11**, 015710 (2008).
180. Niu, Q. *et al.* Research of anti-ultraviolet nano-film structure based on the FDTD method. *Optik* **127**, 539–543 (2016).
181. Saravanan, S. & Dubey, R. Optical absorption enhancement in 40 nm ultrathin film silicon solar cells assisted by photonic and plasmonic modes. *Opt. Commun.* **377**, 65–69 (2016).
182. Liu, J.-X. *et al.* Design and numerical simulation of a bandpass filter nano-film. *Chin. J. Phys.* **69**, 230–239 (2021).
183. ElKabbash, M. *et al.* Fano-resonant ultrathin film optical coatings. *Nat. Nanotechnol.* **16**, 440–446 (2021).
184. Wieduwilt, T. *et al.* Ultrathin niobium nanofilms on fiber optical tapers – a new route towards low-loss hybrid plasmonic modes. *Sci. Rep.* **5**, 17060 (2015).
185. Hasan, M. R., Akter, S., Ahmed, K. & Abbott, D. Plasmonic refractive index sensor employing niobium nanofilm on photonic crystal fiber. *IEEE Photonics Technol. Lett.* **30**, 315–318 (2018).
186. Lühder, T., Wieduwilt, T., Schneidewind, H. & Schmidt, M. A. Electric current-driven spectral tunability of surface plasmon polaritons in gold coated tapered fibers. *AIP Adv.* **8**, 095113 (2018).
187. Markos, C., Kubat, I. & Bang, O. Hybrid polymer photonic crystal fiber with integrated chalcogenide glass nanofilms. *Sci. Rep.* **4**, 6057 (2014).
188. de Ceglia, D. *et al.* Viscoelastic optical nonlocality of low-loss epsilon-near-zero nanofilms. *Sci. Rep.* **8**, 9335 (2018).
189. Braic, L. *et al.* Titanium oxynitride thin films with tunable double epsilon-near-zero behavior for nanophotonic applications. *ACS Appl. Mater. Interfaces* **9**, 29857–29862 (2017).
190. Korneev, P. Harmonics generation in ultra-thin nanofilms irradiated by intense nonrelativistic laser pulses. *Laser Phys.* **22**, 184–194 (2012).
191. Webb, A. S., Poletti, F., Richardson, D. J. & Sahu, J. K. Suspended-core holey fiber for evanescent-field sensing. *Opt. Eng.* **46**, 010503 (2007).
192. Wieduwilt, T. *et al.* Gold-reinforced silver nanoprisms on optical fiber tapers—a new base for high precision sensing. *APL Photonics* **1**, 066102 (2016).
193. Lühder, T., Wieduwilt, T., Schneidewind, H. & Schmidt, M. A. Electric current-driven spectral tunability of surface plasmon polaritons in gold coated tapered fibers. *AIP Adv.* **8**, 095113 (2018).
194. Prabhakar, A. & Mukherji, S. Microfabricated polymer chip with integrated u-bend waveguides for evanescent field absorption based detection. *Lab Chip* **10**, 748–754 (2010).
195. Chen, C.-H., Tsao, T.-C., Tang, J.-L. & Wu, W.-T. A multi-D-shaped optical fiber for refractive index sensing. *Sensors* **10**, 4794–4804 (2010).
196. Pan, Y. Z. *et al.* Fabrication of a D-shaped fiber by femtosecond laser-induced water breakdown for carbon nanotubes' evanescent field interaction mode-locking of a double-clad fiber laser. *Laser Phys.* **23**, 085110 (2013).
197. Osório, J. H. *et al.* Exposed-core fiber multimode interference sensor. *Results Opt.* **5**, 100125 (2021).
198. Warren-Smith, S. C. *et al.* Exposed-core microstructured optical fibers for real-time fluorescence sensing. *Opt. Express* **17**, 18533–18542 (2009).
199. Li, X., Nguyen, L. V., Zhao, Y., Ebendorff-Heidepriem, H. & Warren-Smith, S. C. High-sensitivity sagnac-interferometer biosensor based on exposed core microstructured optical fiber. *Sens. Actuators, B* **269**, 103–109 (2018).

200. Li, X. *et al.* Simultaneous measurement of temperature and refractive index using an exposed core microstructured optical fiber. *IEEE J. Sel. Top. Quantum Electron.* **26**, 1–7 (2020).
201. Bachhuka, A. *et al.* Surface functionalization of exposed core glass optical fiber for metal ion sensing. *Sensors* **19** (2019).
202. Ding, L. *et al.* Nitric oxide optical fiber sensor based on exposed core fibers and CdTe/CdS quantum dots. *Sens. Actuators, B* **273**, 9–17 (2018).
203. Kostecki, R. *et al.* Novel polymer functionalization method for exposed-core optical fiber. *Opt. Mater. Express* **4**, 1515–1525 (2014).
204. Ngo, G. Q. *et al.* Scalable functionalization of optical fibers using atomically thin semiconductors. *Adv. Mater.* **32**, 2003826 (2020).
205. Apanius, M., Kaul, P. B. & Abramson, A. R. Silicon shadow mask fabrication for patterned metal deposition with microscale dimensions using a novel corner compensation scheme. *Sens. Actuators, A* **140**, 168–175 (2007).
206. Coloma Ribera, R., van de Kruijs, R. W. E., Sturm, J. M., Yakshin, A. E. & Bijkerk, F. Intermixing and thermal oxidation of ZrO_2 thin films grown on a-Si, SiN, and SiO_2 by metallic and oxidic mode magnetron sputtering. *J. Appl. Phys.* **121**, 115303 (2017).
207. Xu, L., Wang, X., Lei, T., Sun, D. & Lin, L. Electrohydrodynamic deposition of polymeric droplets under low-frequency pulsation. *Langmuir* **27**, 6541–6548 (2011).
208. Bornside, D., Macosko, C. & Scriven, L. Modeling of spin coating. *J. Imaging Sci. Technol.* **13**, 122–130 (1987).
209. Pierson, H. O. *Handbook of chamical vapor deposition: principles, technology and applications* (Noyes Publications, New York, U.S.A., 1999), 2 edn.
210. Hiller, D. *et al.* Low temperature silicon dioxide by thermal atomic layer deposition: Investigation of material properties. *J. Appl. Phys.* **107**, 064314 (2010).
211. Ratzsch, S., Kley, E.-B., Tünnermann, A. & Szeghalmi, A. Influence of the oxygen plasma parameters on the atomic layer deposition of titanium dioxide. *Nanotechnol.* **26**, 024003 (2014).
212. Wu, S. J., Houng, B. & Huang, B. Effect of growth and annealing temperatures on crystallization of tantalum pentoxide thin film prepared by RF magnetron sputtering method. *J. Alloys Compd.* **475**, 488 – 493 (2009).
213. Anders, A. Tutorial: Reactive high power impulse magnetron sputtering (R-HiPIMS). *J. Appl. Phys.* **121**, 171101 (2017).
214. Hala, M., Zabeida, O., Klemberg-Sapieha, J. E. & Martinu, L. Dynamics of HiPIMS discharge operated in oxygen. *IEEE Trans. Plasma Sci.* **39**, 2582–2583 (2011).
215. Mao, L., Geng, Y., Cao, Y. & Yan, Y. Uniform high-reflectivity silver film deposited by planar magnetron sputtering. *Vacuum* **185**, 109999 (2021).
216. Pieralisi, F., Hanika, M., Scheer, E. & Bender, M. Split sputter mode: a novel sputtering method for flat-panel display manufacturing. *J. Inf. Disp.* **12**, 89–92 (2011).
217. Fan, Q., Chen, X. & Zhang, Y. Computer simulation of film thickness distribution in symmetrical magnet magnetron sputtering. *Vacuum* **46**, 229 – 232 (1995).
218. Broadway, D. M., Platonov, Y. Y. & Gomez, L. A. Achieving desired thickness gradients on flat and curved substrates. In Hoover, R. B. & II, A. B. C. W. (eds.) *X-Ray Optics, Instruments, and Missions II*, vol. 3766, 262 – 274. International Society for Optics and Photonics (SPIE, 1999).
219. Yu, B. *et al.* Control of lateral thickness gradients of Mo-Si multilayer on curved substrates using genetic algorithm. *Opt. Lett.* **40**, 3958–3961 (2015).
220. Sun, S. *et al.* Mo/Si multilayers sputtered onto inclined substrates: experiments and simulations. *Opt. Express* **28**, 13516–13531 (2020).
221. Tompkins, H. & Irene, E. A. *Handbook of ellipsometry* (William Andrew, Norwich, NY, USA, 2005).

222. Ceresa, E. & Garbassi, F. AES/XPS thickness measurement of the native oxide on single crystal Si wafers. *Mater. Chem. Phys.* **9**, 371–385 (1983).
223. Conforto, E. & Schmid, P. E. Pt–Si reaction through interfacial native silicon oxide layers. *Philos. Mag. A* **81**, 61–82 (2001).
224. Carim, A. H., Dovek, M. M., Quate, C. F., Sinclair, R. & Vorst, C. High-resolution electron microscopy and scanning tunneling microscopy of native oxides on silicon. *Science* **237**, 630–633 (1987).
225. Siefke, T. *et al.* Materials pushing the application limits of wire grid polarizers further into the deep ultraviolet spectral range. *Adv. Opt. Mater.* **4**, 1780–1786 (2016).
226. Bright, T. J. *et al.* Infrared optical properties of amorphous and nanocrystalline Ta_2O_5 thin films. *J. Appl. Phys.* **114**, 083515 (2013).
227. Black, J. A. *et al.* Group-velocity-dispersion engineering of tantala integrated photonics. *Opt. Lett.* **46**, 817–820 (2021).
228. Gao, L., Lemarchand, F. & Lequime, M. Exploitation of multiple incidences spectrometric measurements for thin film reverse engineering. *Opt. Express* **20**, 15734–15751 (2012).
229. Chang, P.-H. & Liu, H.-Y. Structures of tantalum pentoxide thin films formed by reactive sputtering of Ta metal. *Thin Solid Films* **258**, 56 – 63 (1995).
230. Demiryont, H., Sites, J. R. & Geib, K. Effects of oxygen content on the optical properties of tantalum oxide films deposited by ion-beam sputtering. *Appl. Opt.* **24**, 490–495 (1985).
231. Hofsäss, H. & Zhang, K. Surfactant sputtering. *Appl. Phys. A* **92**, 517–524 (2008).
232. Spiller, E. *et al.* High-performance mo-si multilayer coatings for extreme-ultraviolet lithography by ion-beam deposition. *Appl. Opt.* **42**, 4049–4058 (2003).
233. Nawazuddin, M. B. S. *et al.* Lotus-shaped negative curvature hollow core fiber with 10.5 db/km at 1550 nm wavelength. *J. Lightwave Technol.* **36**, 1213–1219 (2018).
234. Ivić, Z., Čevizović, D., Željko Pržulj, Lazarides, N. & Tsironis, G. Dispersive properties of self–induced transparency in two–level media. *Chaos, Solitons Fractals* **143**, 110611 (2021).
235. Chen, J. S. *et al.* Photochemistry in photonic crystal fiber nanoreactors. *Chem. Eur. J.* **16**, 5607–5612 (2010).
236. Uchijima, K., Kita, T. & Yamada, H. Nonlinear optical photonic crystal waveguide with TiO2 material. In Teherani, F. H., Look, D. C. & Rogers, D. J. (eds.) *Oxide-based Materials and Devices IV*, vol. 8626, 247 – 257. International Society for Optics and Photonics (SPIE, 2013).
237. Guan, X., Hu, H., Oxenløwe, L. K. & Frandsen, L. H. Compact titanium dioxide waveguides with high nonlinearity at telecommunication wavelengths. *Opt. Express* **26**, 1055–1063 (2018).
238. Fu, M. *et al.* High-q titanium dioxide micro-ring resonators for integrated nonlinear photonics. *Opt. Express* **28**, 39084–39092 (2020).
239. Hammani, K. *et al.* Octave spanning supercontinuum in titanium dioxide waveguides. *Appl. Sci.* **8** (2018).
240. Christensen, S., S., S. R. D., Bang, O. & Bache, M. Directional supercontinuum generation: the role of the soliton. *J. Opt. Soc. Am. B* **36**, A131–A138 (2019).
241. Parmigiani, F. *et al.* Ultra-flat SPM-broadened spectra in a highly nonlinear fiber using parabolic pulses formed in a fiber bragg grating. *Opt. Express* **14**, 7617–7622 (2006).
242. Wieduwilt, T. *et al.* Gold-reinforced silver nanoprisms on optical fiber tapers—a new base for high precision sensing. *APL Photonics* **1**, 066102 (2016).
243. Tuniz, A., Wieduwilt, T. & Schmidt, M. A. Tuning the effective $\mathcal{PT}$ phase of plasmonic eigenmodes. *Phys. Rev. Lett.* **123**, 213903 (2019).
244. Rong, J., Yang, H. & Xiao, Y. Accurately shaping supercontinuum spectrum via cascaded PCF. *Sensors* **20** (2020).

245. Zhang, H. *et al.* All-fiber high power supercontinuum generation by cascaded photonic crystal fibers ranging from 370 nm to 2400 nm. *IEEE Photonics J.* **12**, 7101608 (2020).
246. Arteaga-Sierra, F. R. *et al.* Multi-peak-spectra generation with cherenkov radiation in a non-uniform single mode fiber. *Opt. Express* **22**, 2451–2458 (2014).
247. Venck, S. *et al.* 2–10 µm mid-infrared fiber-based supercontinuum laser source: Experiment and simulation. *Laser Photonics Rev.* **14**, 2000011 (2020).
248. Lou, J. W. *et al.* Broader and flatter supercontinuum spectra in dispersion-tailored fibers. In *Conference on Optical Fiber Communications*, TuH6 (Optical Society of America, 1997).
249. Hu, H., Li, W. & Dutta, N. K. Dispersion-engineered tapered planar waveguide for coherent supercontinuum generation. *Opt. Commun.* **324**, 252 – 257 (2014).
250. Bi, W. *et al.* Ultraviolet-extended supercontinuum generation in zero-dispersion wavelength decreasing photonic crystal fibers. *IEEE Photonics J.* **12**, 3200608 (2020).
251. Chen, H. H., Chen, Z. L., Zhou, X. F. & Hou, J. Ultraviolet-extended flat supercontinuum generation in cascaded photonic crystal fiber tapers. *Laser Phys. Lett.* **10**, 085401 (2013).
252. Billet, M. *et al.* Emission of multiple dispersive waves from a single raman-shifting soliton in an axially-varying optical fiber. *Opt. Express* **22**, 25673–25678 (2014).
253. Milián, C., Ferrando, A. & Skryabin, D. V. Polychromatic cherenkov radiation and supercontinuum in tapered optical fibers. *J. Opt. Soc. Am. B* **29**, 589–593 (2012).
254. Singh, S. P., Mishra, V. & Varshney, S. K. Mid-IR multipeak and stepwise blueshifted dispersive wave generation in liquid-filled chalcogenide capillary optical fibers. *J. Opt. Soc. Am. B* **33**, D65–D71 (2016).
255. Schmitt, K., Oehse, K., Sulz, G. & Hoffmann, C. Evanescent field sensors based on tantalum pentoxide waveguides – a review. *Sensors* **8**, 711–738 (2008).
256. Lamee, K. F., Carlson, D. R., Newman, Z. L., Yu, S.-P. & Papp, S. B. Nanophotonic tantala waveguides for supercontinuum generation pumped at 1560 nm. *Opt. Lett.* **45**, 4192–4195 (2020).
257. Vukovic, N. & Broderick, N. G. R. Method for improving the spectral flatness of the supercontinuum at 1.55 µm in tapered microstructured optical fibers. *Phys. Rev. A* **82**, 043840 (2010).
258. Van, L. C. *et al.* Supercontinuum generation in photonic crystal fibers infiltrated with nitrobenzene. *Laser Phys.* **30**, 035105 (2020).
259. Humbach, O., Fabian, H., Grzesik, U., Haken, U. & Heitmann, W. Analysis of OH absorption bands in synthetic silica. *J. Non-Cryst. Solids* **203**, 19–26 (1996).
260. Huang, P. L. *et al.* Stable mode-locked fiber laser based on CVD fabricated graphene saturable absorber. *Opt. Express* **20**, 2460–2465 (2012).
261. Elu, U. *et al.* Seven-octave high-brightness and carrier-envelope-phase-stable light source. *Nat. Photonics* **15**, 277–280 (2021).
262. Lefort, C. *et al.* Multicolor multiphoton microscopy based on a nanosecond supercontinuum laser source. *J. Biophotonics* **9**, 709–714 (2016).
263. Hontani, Y., Xia, F. & Xu, C. Multicolor three-photon fluorescence imaging with single-wavelength excitation deep in mouse brain. *Sci. Adv.* **7**, eabf3531 (2021).
264. Gottschall, T. *et al.* Fiber-based light sources for biomedical applications of coherent anti-stokes raman scattering microscopy. *Laser Photonics Rev.* **9**, 435–451 (2015).
265. Li, K.-C., Huang, L. L. H., Liang, J.-H. & Chan, M.-C. Simple approach to three-color two-photon microscopy by a fiber-optic wavelength convertor. *Biomed. Opt. Express* **7**, 4803–4815 (2016).
266. Chemnitz, M. *et al.* Widely tuneable fiber optical parametric amplifier for coherent anti-stokes raman scattering microscopy. *Opt. Express* **20**, 26583–26595 (2012).
267. Velázquez-Ibarra, L., Díez, A., Silvestre, E. & Andrés, M. V. Wideband tuning of four-wave mixing in solid-core liquid-filled photonic crystal fibers. *Opt. Lett.* **41**, 2600–2603 (2016).

268. Dudley, J. M., Genty, G. & Coen, S. Supercontinuum generation in photonic crystal fiber. *Rev. Mod. Phys.* **78**, 1135–1184 (2006).
269. Moya, R., Kondo, T., Norris, A. C. & Schlau-Cohen, G. S. Spectrally-tunable femtosecond single-molecule pump-probe spectroscopy. *Opt. Express* **29**, 28246–28256 (2021).
270. Chirkin, A. S., Volkov, V. V., Laptev, G. D. & Morozov, E. Y. Consecutive three-wave interactions in nonlinear optics of periodically inhomogeneous media. *Quantum Electron.* **30**, 847–858 (2000).
271. Copie, F., Kudlinski, A., Conforti, M., Martinelli, G. & Mussot, A. Modulation instability in amplitude modulated dispersion oscillating fibers. *Opt. Express* **23**, 3869–3875 (2015).
272. Conforti, M., Trillo, S., Kudlinski, A. & Mussot, A. Multiple QPM resonant radiations induced by MI in dispersion oscillating fibers. *IEEE Photonics Technol. Lett.* **28**, 740–743 (2016).
273. Zia, H., Lüpken, N. M., Hellwig, T., Fallnich, C. & Boller, K.-J. Supercontinuum generation in media with sign-alternated dispersion. *Laser Photonics Rev.* **14**, 2000031 (2020).
274. Jankowski, M. *et al.* Ultrabroadband nonlinear optics in nanophotonic periodically poled lithium niobate waveguides. *Optica* **7**, 40–46 (2020).
275. Bilotti, F., Toscano, A. & Vegni, L. Design of spiral and multiple split-ring resonators for the realization of miniaturized metamaterial samples. *IEEE Trans. Antennas Propag.* **55**, 2258–2267 (2007).
276. Rubio-Mercedes, C. E., Lima, I. T., Hernández-Figueroa, H. E. & Rodríguez-Esquerre, V. F. Periodic segmented waveguide analysis by using the 2D finite element method. In *2011 SBMO/IEEE MTT-S International Microwave and Optoelectronics Conference (IMOC 2011)*, 876–880 (2011).
277. Kitamura, R., Pilon, L. & Jonasz, M. Optical constants of silica glass from extreme ultraviolet to far infrared at near room temperature. *Appl. Opt.* **46**, 8118–8133 (2007).
278. Huang, Y., Yang, H., Zhao, S., Mao, Y. & Chen, S. Design of photonic crystal fibers with flat dispersion and three zero dispersion wavelengths for coherent supercontinuum generation in both normal and anomalous regions. *Results Phys.* **23**, 104033 (2021).
279. Langrock, C., Fejer, M. M., Hartl, I. & Fermann, M. E. Generation of octave-spanning spectra inside reverse-proton-exchanged periodically poled lithium niobate waveguides. *Opt. Lett.* **32**, 2478–2480 (2007).
280. Kühlke, D. *Optik Grundlagen und Anwendungen* (Wissenschaftlicher Verlag Harri Deutsch GmbH, Frankfurt a.M., Germany, 2004).
281. Wemple, S. H. Material dispersion in optical fibers. *Appl. Opt.* **18**, 31–35 (1979).

Appendix

2-D ray model with dispersion separation

Two pulses of different central frequencies ω_1 and ω_2 experience a walk-off while passing the same distance g through a medium due to their different group velocities v_g. This leads to a temporal delay of both pulses

$$\Delta T = g\left(\frac{1}{v_g(\omega_2)} - \frac{1}{v_g(\omega_1)}\right), \tag{A.38}$$

which can be expanded in a Taylor series of first order around ω_1.

$$\Delta T \approx g\left[\frac{1}{v_g(\omega_1)} + \frac{\partial}{\partial\omega}\left(\frac{1}{v_g(\omega)}\bigg|_{\omega=\omega_1}\right)(\omega_2-\omega_1) - \frac{1}{v_g(\omega_1)}\right] \tag{A.39}$$

$$= g\ \ \mathrm{GVD}(\omega_1)\,(\omega_2-\omega_1) \tag{A.40}$$

Here, the intrinsic definition of the GVD was utilized: $\mathrm{GVD} = \frac{\partial^2 k}{\partial\omega^2} = \frac{\partial\beta_1}{\partial\omega} = \frac{\partial v_g^{-1}}{\partial\omega}$. Rearranging Eq. (A.40) gives

$$\mathrm{GVD} = \frac{1}{g}\,\frac{\Delta T}{\omega_2-\omega_1} = \frac{1}{d}\,\frac{\partial T}{\partial\omega}. \tag{A.41}$$

The ray model of a two dimensional slab waveguide of height b consists of a totally internal reflecting zig-zag path of light inside the central high index region n_{co} (Fig. A.1). Stable modes of multiple rays at the same angle ϑ can only form when interfering constructively upon one round trip of order m (positive integer) in transverse direction (x), that is, traversing the height twice and including the phase jumps $\alpha(\vartheta)$ at both reflections

$$2k_x b - 2\alpha(\vartheta) = 2\pi\mathrm{m} \tag{A.42}$$

$$2kb\sin\vartheta - 2\alpha(\vartheta) = 2\pi\mathrm{m}. \tag{A.43}$$

With the wave number $k = n_{\mathrm{co}}2\pi/\lambda$ the specific ray angle of mode m is

$$\vartheta = \arcsin\left(\lambda\frac{\mathrm{m}+\alpha(\vartheta)/\pi}{2n_{\mathrm{co}}b}\right), \tag{A.44}$$

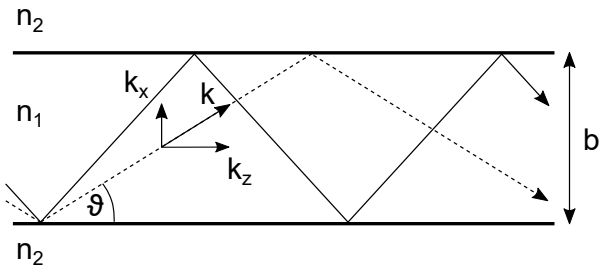

Figure A.1: Ray model in a 2D slab waveguide. The dashed ray at a shallower angle represents the fundamental mode whereas the solid line is a higher-order mode.

with the angle and polarization dependent phase jumps of the total internal reflections [280]

$$\alpha_{\perp}(\vartheta) = 2\arctan\left(\frac{1}{\sin\vartheta}\sqrt{\cos^2\vartheta - \frac{n_{\mathrm{cl}}^2}{n_{\mathrm{co}}^2}}\right) \tag{A.45}$$

$$\alpha_{\parallel}(\vartheta) = 2\arctan\left(\frac{n_{\mathrm{co}}^2}{n_{\mathrm{cl}}^2}\frac{1}{\sin\vartheta}\sqrt{\cos^2\vartheta - \frac{n_{\mathrm{cl}}^2}{n_{\mathrm{co}}^2}}\right). \tag{A.46}$$

Parallel and perpendicular polarization directions are defined with respect to the ray plane, i.e. the paper plane of Fig. A.1. The equation system Eq. (A.44) in combination with Eq. (A.45) or Eq. (A.46) can be solved numerically to retrieve ϑ.

The time T needed to travel the distance d through the waveguide is given by

$$T = \frac{g}{\cos\vartheta}\frac{1}{v_g} = \frac{g}{\cos(\vartheta)\,c}\left(n_{\mathrm{co}} - \lambda\frac{\mathrm{d}n_{\mathrm{co}}}{\mathrm{d}\lambda}\right) \tag{A.47}$$

For the second step, $v_g^{-1} = \beta_1$ and Eq. 2.4 is utilized. Eq. A.47 inserted in Eq. (A.41) leads to

$$\mathrm{GVD} = \frac{1}{g}\frac{\partial T}{\partial\omega} = \frac{1}{g}\frac{\partial\lambda}{\partial\omega}\frac{\partial T}{\partial\lambda} = -\frac{1}{2\pi}\frac{\lambda^2}{c^2}\frac{\partial}{\partial\lambda}\left[\frac{1}{\cos\vartheta}\left(n_{\mathrm{co}} - \lambda\frac{\mathrm{d}n_{\mathrm{co}}}{\mathrm{d}\lambda}\right)\right] \tag{A.48}$$

$$= -\frac{1}{2\pi}\frac{\lambda^2}{c^2}\Bigg[\underbrace{\frac{\partial}{\partial\lambda}\left(\frac{1}{\cos\vartheta}\right)\left(n_{\mathrm{co}} - \lambda\frac{\mathrm{d}n_{\mathrm{co}}}{\mathrm{d}\lambda}\right)}_{\text{waveguide dispersion}} + \underbrace{\frac{1}{\cos\vartheta}\frac{\partial}{\partial\lambda}\left(n_{\mathrm{co}} - \lambda\frac{\mathrm{d}n_{\mathrm{co}}}{\mathrm{d}\lambda}\right)}_{\text{material dispersion}}\Bigg]. \tag{A.49}$$

With the second term of Eq. (A.49) only featuring the second order spectral derivative of the refractive index of the core material $\frac{\partial}{\partial\lambda}\left(n_{\mathrm{co}} - \lambda\frac{\mathrm{d}n_{\mathrm{co}}}{\mathrm{d}\lambda}\right) = -\lambda\frac{d^2 n_{\mathrm{co}}}{d\lambda^2}$, it can be identified as the material dispersion. In contrast to other models, a cosine term of ϑ is still present. For small ray angles, i.e. weakly guiding waveguides, this term is negligible, leading to a convergence towards the conventional formula without the ray angle dependence [93,281]. The first term of the Eq. (A.49) includes the spectral derivative of the ray angle ϑ, clearly being the only waveguide related parameter of the ray trace. Therefore, the first term can be identified as the waveguide dispersion part of the total GVD.

Applying this model to a waveguide consisting of a silica core (dispersion of Ref. 86) with a large width of $b = 8$ µm in air reveals small ray angles for the fundamental modes (Fig. A.2a). The material dispersion is the major contribution to the total dispersion and the polarization as a negligible influence (Fig. A.2b). Reducing the core size to 200 nm increases the ray angle, approaching the critical angle of total internal reflection at about 45°. The increased slope of ϑ raises the contribution of the waveguide dispersion (Fig. A.2c). Furthermore, the convergence to the critical angle causes the waveguide dispersion to bend upwards, ultimately changing its sign. Although it is not enough to cause a second, long-wavelength ZDW for the total dispersion, it shows a clear trend towards it. This model cannot quantitatively explain the dispersion of fibers, yet, it qualitatively exhibits

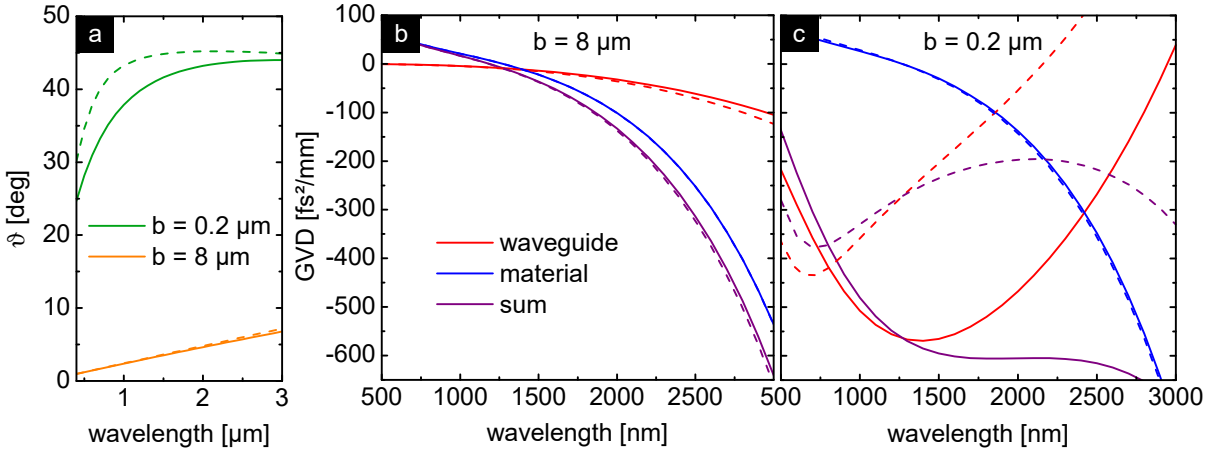

Figure A.2: (a) Angle of the light ray of the waveguide model of Fig. A.1 for two different widths b. Dashed lines correspond to parallel polarization (Eq. A.46) and solid lines to perpendicular polarization (Eq. A.45) with respect to the ray plane. The separation of the GVD into the material and waveguide contribution according to Eq. A.49 for waveguides with a width of 8 µm and 200 nm are shown in (b) and (c), respectively.

a resembling behavior compared to the more accurate dispersion separation approach of Section 2.2.1.

One over-simplification is the lack of the contribution of the cladding material to the material dispersion. Obviously, the evanescent parts of the mode are located within the cladding, which is neglected by the sharp total internal reflection of the ray model. One method to include the influence of the cladding material is to account for the Goos-Hänchen shift as in Ref.[42]. There will be an offset of the rays at the reflection points in z direction and an additional phase shift. Effectively, the waveguide can be treated to have a larger width $b + 2\Delta b$ with the additional enlargement on both sides consisting of cladding material, while neglecting refraction at the interface. This improvement of the model might enhance the results to more accurately reflect the dispersion, but it was not implemented within the scope of this work.

Cross section and end faces of ECFs

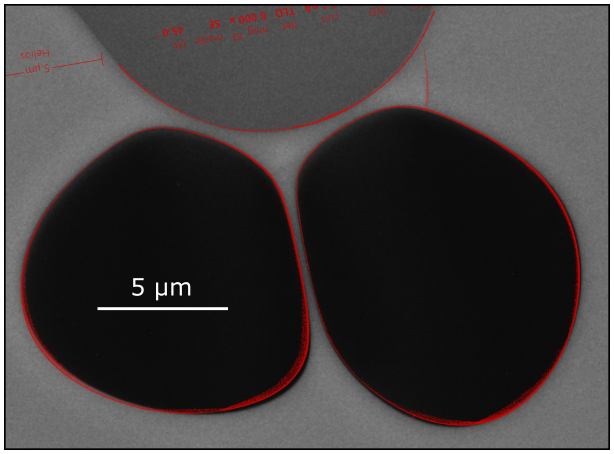

Figure A.3: Comparison of the ECF's cross section (SEM images) at the end of the fiber spool in the beginning (red outline, February 2019) and the end of experiments (July 2021, main picture), separated by less than 10 m.

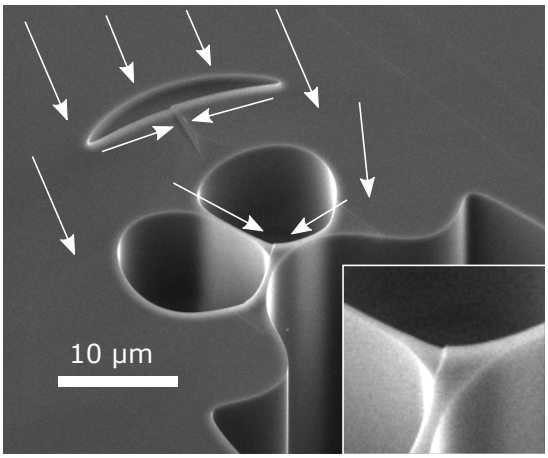

Figure A.4: Angled SEM of the cleaved end face of an ECF. Arrows show the breaking direction, creating conflicts of height and consequential step profiles when facing each other at the opposite side of air holes. The inset shows the magnified core section.

IR losses of silica

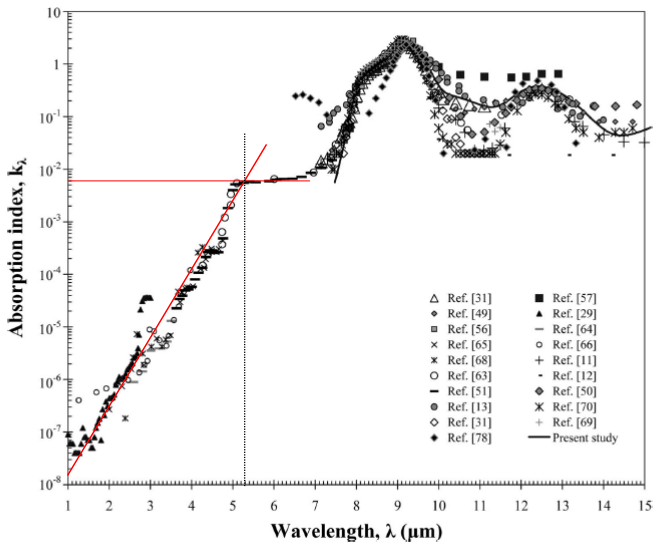

Figure A.5: Imaginary part of the RI of silica collected from various works cited in the original paper by Kitamura et al.[277] Red line: linear approximation of IR losses used in this work, capped at a constant value for $\lambda > 5.3$ µm (valid until $\lambda = 7$ µm). Adapted with permission from Ref. 277 © The Optical Society.

List of publications

Publications directly relevant for this thesis:

Lühder, T.A.K., Schaarschmidt, K., Goerke, S., Schartner, E. P., Ebendorff-Heidepriem, H., Schmidt, M. A. Resonance-induced dispersion tuning for tailoring nonsolitonic radiation via nanofilms in exposed core fibers. *Laser Photonics Rev.* **14**, 1900418 (2020).

Lühder, T.A.K., Schneidewind, H., Schartner, E. P., Ebendorff-Heidepriem, H., Schmidt, M. A. Longitudinally thickness-controlled nano-films on exposed core fibers enabling spectrally flattened supercontinuum generation. *Light Adv. Manuf.* **2**, 21 (2021).

Lühder, T.A.K., Chemnitz, M., Schneidewind, H., Schartner, E. P., Ebendorff-Heidepriem, H., Schmidt, M. A. Tailored multi-color dispersive wave formation in quasi-phase-matched exposed core fibers, *Adv. Sci.* **9**, 2103864 (2022).

Conference contribution:

Lühder, T.A.K., Schneidewind, H., Goerke, S., Schaarschmidt, K., Schartner, E. P., Ebendorff-Heidepriem, H., Schmidt, M. A., Graded nanofilm controlled dispersion and supercontinuum generation in exposed core fibers, *CLEO:QELS*, OSA Technical Digest (Optica Publishing Group), FTh1J.6. (2021)

Publications not featured in this thesis:

Lühder, T.A.K., Wieduwilt, T., Schneidewind, H., and Schmidt, M. A., Electric current-driven spectral tunability of surface plasmon polaritons in gold coated tapered fibers, *AIP Adv.* **8**, 095113 (2018).

Lühder, T.A.K., Plentz, J., Kobelke, J., Wondraczek, K., and Schmidt, M. A., All-fiber integrated in-line semiconductor photoconductor, *J. Lightwave Technol.* **37**, 3244-3251 (2019).

Ngo, G. Q., George, A., Schock, R. T. K., Tuniz, A., Najafidehaghani, E., Gan, Z., Geib, N. C., Bucher, T., Knopf, H., Saravi, S., Neumann, C., **Lühder, T.A.K.**, Schartner, E. P., Warren-Smith, S. C., Ebendorff-Heidepriem, H., Pertsch, T., Schmidt, M. A., Turchanin, A., Eilenberger, F., Scalable functionalization of optical fibers using atomically thin semiconductors. *Adv. Mater.* **32**, 2003826 (2020).

Qi, X.; Schaarschmidt, K.; Li, G.; Junaid, S.; Scheibinger, R.; **Lühder, T.A.K.**; Schmidt, M.A. Understanding nonlinear pulse propagation in liquid strand-based photonic bandgap fibers. *Crystals* **11**, 305 (2021).

Conference contribution:

Lühder, T.A.K., Wieduwilt, T., Schneidewind, H., and Schmidt, M. A., Electrically induced tunability of surface plasmon polaritons in gold coated tapered fibers, *Photonic North*, Montreal, poster-63 (2018)

Acknowledgment

I would like to thank all the colleagues that helped me with scientific discussions, materials and favours during the time of my PhD. This includes all the work that did not make it into this thesis, preventing them from appearing in the declaration of independent work. Barbara Geisenhainer and Claudia Aichele (HF-etching equipment), Jonathan Plentz (AZO+Ag+Al layers, Borofloat samples, masks, electrical sensing setup), Frank Bauer (electronics), Ron Fatobene-Ando (plasmonics discussion), Sven Lindsen (noise canceling), Andrä Gudrun (AZO films), Malte Plidschun (cutting of circuit board), Martin Lorenz (Laserdiode), Clara Stiebing (Raman), Assad Arsad/Martin Leich/Tino Elsmann/Martin Becker (OSA sharing), Alexander Hartung (Comsol discussion, IR objective), Jens Albert (wafer saw), Armin Andrae (water beam cutting), Peter Horbert (3D printer), Tina Eschrich (fiber taper drawing), Mario Ziegler (AlO_x films, cleanroom), Birger Steinbach (Au films), Jan & Andrea Dellith (SEM), Ehud Shchori (acrylate discussion), Andreas Ihring/Wolfgang Morgenroth/Uwe Hübner/Christian Schmidt/Gabriele Schmiedl (film discussion), Annett Gawlik (laser diode test), Dennis Arslan (ENZ material charging simulation), and the members of the IPHT workshop (sample cutting).

I appreciate the helpful review, constructive feedback, and fruitful discussion in our weekly scientific meetings with Ramona, Saher, Kay, Xue, Johannes, Mario, and Torsten. Sharing labs, the working time, and breaks with all members of the hybrid fibers working group of the Leibniz-Institute of Photonic Technology was pleasant. Special thanks goes to our boss Markus Schmidt, enforcing effective and appropriate regulations during the difficult times with corona while keeping the science and the labs running at all times.

I thank all my colleagues for the successful cross-working-group, cross-institutional, and cross-continental collaboration to accomplish impactful scientific advancements and joint papers. This includes Kay Schaarschmidt, Torsten Wieduwilt, Henrik Schneidewind, Xue Qi, and Markus Schmidt (hybrid fibers), Sebastian Goerke (competence center for micro- and nanotechnologies, IPHT), Jonathan Plentz (functional interfaces, IPHT), Jens Kobelke and Katrin Wondraczek (competence center for specialty optical fibers, IPHT), Quyet Ngo (IAP, Jena), Reinhard Geiss (Lichtwerkstatt Jena), Mario Chemnitz (INRS, Canada), Erik Schartner and Heike Ebendorff-Heidepriem (University of Adelaide, Australia).

I acknowledge funding from the german research foundation through the projects SCHM2655/9-1, SCHM2655/11-1, SCHM2655/12-1, and SCHM2655/3-2.

Finally, I would like to thank the international research training group (GRK 2101), the graduate academy of the FSU, the OSA student chapter, and the PhD council of the IPHT for their countless social events, workshops, and summer schools.

Ehrenwörtliche Erklärung

Ich erkläre hiermit ehrenwörtlich, dass ich die vorliegende Arbeit selbständig, ohne unzulässige Hilfe Dritter und ohne Benutzung anderer als der angegebenen Hilfsmittel und Literatur angefertigt habe. Die aus anderen Quellen direkt oder indirekt übernommenen Daten und Konzepte sind unter Angabe der Quelle gekennzeichnet.

Bei der Auswahl und Auswertung folgenden Materials haben mir die nachstehend aufgeführten Personen in der jeweils beschriebenen Weise unentgeltlich geholfen:
1. Ta_2O_5 Beschichtung und Messung für Figs. 4.4 und 4.8: Henrik Schneidewind
2. TiO_2 Beschichtung: Sebastian Goerke
3. SEM Bild Aufnahme: Jan und Andrea Dellith
4. ECF Herstellung: Erik Schartner und Heike Ebendorff-Heidepriem
5. Einführung in nichtlineare Propagationssimulation und speziell Simulationen in Figs. 5.7a+b and 5.9: Kay Schaarschmidt
6. Modell nach Okamoto in Kapitel 3.1 und Berechnungen für Figs. 3.1 und 3.2: Markus Schmidt
7. Einführung ins Laserschneiden an der Lichtwerkstatt Jena: Reinhard Geiss

Weitere Personen waren an der inhaltlich-materiellen Erstellung der vorliegenden Arbeit nicht beteiligt. Insbesondere habe ich hierfür nicht die entgeltliche Hilfe von Vermittlungs- bzw. Beratungsdiensten (Promotionsberater oder andere Personen) in Anspruch genommen. Niemand hat von mir unmittelbar oder mittelbar geldwerte Leistungen für Arbeiten erhalten, die im Zusammenhang mit dem Inhalt der vorgelegten Dissertation stehen.

Die Arbeit wurde bisher weder im In- noch im Ausland in gleicher oder ähnlicher Form einer anderen Prüfungsbehörde vorgelegt.

Die geltende Promotionsordnung der Physikalisch-Astronomischen Fakultät ist mir bekannt.

Ich versichere ehrenwörtlich, dass ich nach bestem Wissen die reine Wahrheit gesagt und nichts verschwiegen habe.

Ort, Datum Unterschrift d. Verfassers